MASSIVE OUTFLOWS ASSOCIATED WITH ATLASGAL CLUMPS

A. Y. Yang[1,2,3], M. A. Thompson[3], J. S. Urquhart[4], W. W. Tian[1,2],

Draft version December 13, 2017

ABSTRACT

We have undertaken the largest survey for outflows within the Galactic Plane using simultaneously observed ^{13}CO and C^{18}O data. 325 out of a total of 919 ATLASGAL clumps have data suitable to identify outflows, and 225 (69 ± 3%) of them show high velocity outflows. The clumps with detected outflows show significantly higher clump masses (M_{clump}), bolometric luminosities (L_{bol}), luminosity-to-mass ratios (L_{bol}/M_{clump}) and peak H_2 column densities (N_{H_2}) compared to those without outflows. Outflow activity has been detected within the youngest quiescent clump (i.e., 70μm weak) in this sample and we find that the outflow detection rate increases with M_{clump}, L_{bol}, L_{bol}/M_{clump} and N_{H_2}, approaching 90% in some cases (UC Hii regions = 93 ± 3%; masers = 86 ± 4%; HC Hii regions = 100%). This high detection rate suggests that outflows are ubiquitous phenomena of massive star formation. The mean outflow mass entrainment rate implies a mean accretion rate of $\sim 10^{-4}\,M_\odot\,yr^{-1}$, in full agreement with the accretion rate predicted by theoretical models of massive star formation. Outflow properties are tightly correlated with M_{clump}, L_{bol} and L_{bol}/M_{clump}, and show the strongest relation with the bolometric clump luminosity. This suggests that outflows might be driven by the most massive and luminous source within the clump. The correlations are similar for both low-mass and high-mass outflows over 7 orders of magnitude, indicating that they may share a similar outflow mechanism. Outflow energy is comparable to the turbulent energy within the clump, however, we find no evidence that outflows increase the level of clump turbulence as the clumps evolve. This implies that the origin of turbulence within clumps is fixed before the onset of star formation.

Subject headings: stars: formation–stars: massive–stars: early-type–ISM: jets and outflows–ISM: molecules–submillimetre: ISM

1. INTRODUCTION

Star formation is an intrinsically complex process involving the collapse and accretion of matter onto protostellar objects, but also the loss of mass from the star-forming system in the form of bipolar outflows (Lada 1985). Outflows from newly formed stars inject momentum and energy into the surrounding molecular cloud at distances ranging from a few AU to up to tens of parsecs away from the star (Arce et al. 2007). Molecular outflows are thus one of the earliest observable signatures of both low- and high-mass star formation (Shepherd & Churchwell 1996a; Kurtz et al. 2000; Molinari et al. 2002; Beuther et al. 2002; Wu et al. 2004). The first detection of outflows was in 1976 (Zuckerman et al. 1976; Kwan & Scoville 1976). Since then, carbon monoxide (CO) emission lines from single-dish and interferometer observations have been widely used to identify outflows (e.g., Arce et al. 2007; de Villiers et al. 2014; Maud et al. 2015). Outflows can be identified as CO lines showing high-velocity wings, with two spatially separated lobes, respectively blue and red velocity shifted (Snell et al. 1980).

Molecular outflows are thus a useful tool to improve our understanding of the underlying formation process of stars of all masses (Arce et al. 2007), in particular for high-mass stars ($> 8\,M_\odot$). For low-mass stars, bipolar outflows driven by accretion disks are basic building blocks of the formation process verified in theoretical models (Shu et al. 1987) and in observations (e.g., Bontemps et al. 1996; Bachiller 1996; Richer et al. 2000; Arce et al. 2007; Hatchell et al. 2007). However, the formation process of massive stars is still very much under debate (Tan et al. 2014) with two major competing models: (i) core accretion via disk (Yorke & Sonnhalter 2002; McKee & Tan 2003) and (ii) competitive accretion (Bonnell et al. 2001). The former can be subdivided into two main categories: (a) increased spherical accretion rates via turbulent cores to overcome the radiation pressure (McKee & Tan 2003) or (b) accretion via a disk that allows beaming of photons to escape along the polar axis (the so-called flashlight effect) to alleviate the limit of radiation (Yorke & Sonnhalter 2002). The easiest way to discriminate the two models of "accretion via a disk" and "competitive accretion" might be the detection of the accretion disk around massive protostars, however, these can be difficult to detect as the accretion disk is small, short-lived, and easily confused with the circumstellar envelope (Kim & Kurtz 2006). If massive stars do form via an accretion disk, as low-mass stars do, they should generate massive and powerful outflows similar to those seen towards low mass stars (Zhang et al. 2001; de Villiers et al. 2014). Thus, observing outflows toward massive young stellar objects (YSOs) can be directly used to help shed light on the debate (Kim & Kurtz 2006). While detailed high angular resolution interferometry is ultimately required to study outflows at sufficient resolution to distinguish between theoretical models, large outflow surveys using heterodyne focal plane arrays (e.g., de Villiers et al. 2014) provide statistically significant samples and are useful finder charts for later interferometric studies.

Outflow feedback can also improve our understanding the origin of turbulence in clouds, but it remains a challenge to quantify the cumulative impact of the outflow-driven turbulence on molecular clouds (Frank et al. 2014). Observations and simulation have both suggested that outflow-driven turbulence can and cannot have a significant effect on natal core (e.g., Arce et al. 2010; Mottram & Brunt 2012; Cunningham et al. 2009; Krumholz et al. 2012). Some simulation results

[1] Key Laboratory of Optical Astronomy, National Astronomical Observatories, Chinese Academy of Sciences, Beijing 100012, China; ayyang@bao.ac.cn

[2] University of Chinese Academy of Science, 19A Yuquan Road, Beijing 100049, China

[3] Centre for Astrophysics Research, School of Physics Astronomy & Mathematics, University of Hertfordshire, College Lane, Hatfield, AL10 9AB, UK; m.a.thompson@herts.ac.uk

[4] Centre for Astrophysics and Planetary Science, University of Kent, Canterbury, CT2 7NH, UK

indicated that outflow feedback has a smaller impact on high-mass star forming regions (e.g., Krumholz et al. 2012), but others have suggested that outflows can act to maintain the turbulence in a cloud (e.g., Cunningham et al. 2009). There exists evidence that outflows have enough power to drive turbulence in the local environment (Arce et al. 2010; Mottram & Brunt 2012), but not contribute significantly to the turbulence of the clouds (Arce et al. 2010; Plunkett et al. 2015; Maud et al. 2015). Frank et al. (2014) have reviewed that impact driven by outflows on length-scales of disks, envelopes, and clouds. A statistical sample of outflow-harboring cores at different evolutionary stages is needed to understand the effect of outflows on their parent clumps (Arce et al. 2007).

Outflow activities have been detected at different evolutionary stages of young stellar objects (YSO): low-mass YSO from Class 0 (e.g., Bontemps et al. 1996; Bally 2016) to FU Orionis (e.g., Evans et al. 1994; Königl et al. 2011) and high-mass YSO from pre-ultracompact HII regions (e.g., Kim & Kurtz 2006; de Villiers et al. 2014) to ultracompact (UC) HII regions (e.g., Qin et al. 2008; Maud et al. 2015). With four evolutionary phases of low-mass YSO from Class 0 to III (Lada & Wilking 1984; Andre et al. 1993), the most powerful CO outflows are detected around the youngest (Class 0) objects (Bachiller & Gomez-Gonzalez 1992), and the outflow energy was found to decrease with YSO evolutionary stages (Bontemps et al. 1996; Curtis et al. 2010b; Bally 2016). According to an early evolutionary sequences of massive star formation: from hot cores to hypercompact regions (HC HII) and UC HII regions (e.g., Churchwell 2002; Zinnecker & Yorke 2007), outflows are thought to be developed from the "hot core" phase (Kurtz et al. 2000), just before the UC HII phase (Shepherd & Churchwell 1996a; Wu et al. 1999; Zhang et al. 2001; Beuther et al. 2002; Molinari et al. 2002). These early phases of massive star formation are frequently associated with water and methanol masers (e.g., Caswell 2013; Urquhart et al. 2011, 2015), which supports a close association between these masers and outflows activity (e.g., Codella et al. 2004; de Villiers et al. 2014). Referring to our sample, König et al. (2017) and Urquhart et al. (2018) identified an early evolutionary sequence for massive star formation clumps based on their infrared to radio spectral energy distribution (SED), including the youngest quiescent phase (i.e., a starless or pre-stellar phase with weak 70μm emission), protostellar (i.e., clumps with mid-infrared 24μm weak but far-infrared bright), YSO-forming clumps (YSO clump; i.e., mid-infrared 24μm bright clumps), and massive star formation clumps (MSF clumps; i.e., mid-infrared 24μm bright clumps with a massive star formation tracer). The earliest quiescent stage has been found to be associated with molecular outflows (Traficante et al. 2017). Discussing the outflow properties of a large sample of clumps at different evolutionary stages allows us to study outflow activity as a function of MYSO evolutionary state.

Bipolar outflows have been extensively studied in low-mass (e.g., Bontemps et al. 1996; Bachiller 1996; Hatchell et al. 2007; Bjerkeli et al. 2013) and high-mass sources (e.g., Zhang et al. 2005; Beuther et al. 2002; de Villiers et al. 2014; Maud et al. 2015). The typical values of outflow mass (M_{out}), outflow entrainment rates ($\dot{M}_{out}$), momentum rates (F_{out}), mechanical luminosity (L_{out}), dynamic timescale (t_d), and average outflow sizes (ℓ_{out}) for low- and high-mass objects are summarized in Table 1. Outflows from massive protostars with typical values (e.g., Richer et al. 2000; Zhang et al. 2005; Kim & Kurtz 2006; Beuther et al. 2002; Wu et al. 2004; Arce et al. 2007; de Villiers et al. 2014, 2015; Maud et al. 2015) are approximately more than two order of magnitude greater than typical outflows from low-mass YSOs (e.g., Bontemps et al. 1996; Arce et al. 2007; Wu et al. 2004), with similar dynamic timescale. The similar correlations between outflow properties and clump mass, bolometric luminosity over several orders of magnitude suggest that a common driving mechanism may be responsible for all masses and luminosities (Bontemps et al. 1996; Zhang et al. 2005; Beuther et al. 2002; Wu et al. 2004; López-Sepulcre et al. 2009; de Villiers et al. 2014).

TABLE 1
Typical values for low-mass and high-mass outflows

Parameters	low-mass outflows [1]	High-mass outflows [2]
M_{out}	$0.1 \sim 1\,M_\odot$	$10 \sim 10^3\,M_\odot$
$\dot{M}_{out}$	$10^{-7} \sim 10^{-6}\,M_\odot/yr$	$10^{-5} \sim 10^{-3}\,M_\odot/yr$
F_{out}	$10^{-6} \sim 10^{-5}\,M_\odot\,km/s/yr$	$10^{-4} \sim 10^{-2}\,M_\odot\,km/s/yr$
L_{out}	$0.1 \sim 1\,L_\odot$	$0.1 \sim 100\,L_\odot$
ℓ_{out}	$0.1 \sim 1\,pc$	$0.5 \sim 2.5\,pc$
t_d	$(0.1 \sim 10) \times 10^5$ yr	$(0.1 \sim 10) \times 10^5$ yr

Reference: 1, e.g., Bontemps et al. (1996); Arce et al. (2007); Wu et al. (2004); Hatchell et al. (2007). 2, e.g., Richer et al. (2000); Zhang et al. (2005); Kim & Kurtz (2006); Beuther et al. (2002); Wu et al. (2004); Arce et al. (2007); de Villiers et al. (2014, 2015); Maud et al. (2015).

High-velocity outflow structures are common in both low mass and high-mass YSOs. The occurrence frequency of molecular outflows in low-mass YSOs ranges between 70% and 90% (Bontemps et al. 1996; Bjerkeli et al. 2013). For massive protostars, Zhang et al. (2001, 2005) detected high-velocity gas in 57% of 69 luminous IRAS sources, and Codella et al. (2004) show a similar detection rate of 50% (39/80) for masers. Higher detection rates of 70% ∼ 90% are found in massive star formation regions (e.g., Shepherd & Churchwell 1996b; Beuther et al. 2002; Kim & Kurtz 2006; Maud et al. 2015). Recently studies show detection rates of 100% for 11 very luminous YSOs (López-Sepulcre et al. 2009) and 44 methanol masers (de Villiers et al. 2014). This suggests that outflows are ubiquitous phenomena of high-mass and low-mass star formation. However, all of these studies have focused on selected samples and therefore these high detection rates may not be representative of the general population of embedded massive protostellar sources.

The physical parameters of the outflows and their relations have also been investigated for massive protostars (Cabrit & Bertout 1992; Shepherd & Churchwell 1996b; Beuther et al. 2002; Wu et al. 2004; de Villiers et al. 2014). These studies have proposed a view that massive protostars can drive powerful outflows, and further suggested that outflows can provide a link between low- and high-mass star formation scenarios. However, these correlations between outflow parameters are obtained from targeted observations for small samples of luminous or maser sources, or massive star-forming regions (MSF) (López-Sepulcre et al. 2009; Beuther et al. 2002; Kim & Kurtz 2006). Wu et al. (2004) undertook statistical analysis toward a large sample of 139 high-mass objects with outflows detection based on compilation of data from literatures. However, Cabrit & Bertout (1990) proposed that the estimation of outflow parameters could vary over 2 to 3 orders of magnitude depending on procedures used. Recently, van der Marel et al. (2013) proposed a scatter by up to a factor of 5 for the outflow force of low-luminosity embedded sources from different studies. Analyzing compiled data from the literatures would thus have a large dispersion due to the differing procedures used by various authors. Therefore, a self-consistent statistical analysis toward a large homogeneous sample of molecular outflows is needed to further understand outflow characteristics.

In this paper, we undertake the largest and most unbiased survey of outflows yet carried out by combining the ATLASGAL and CHIMPS surveys. Our search covers all 919 ATLASGAL clumps in the CHIMPS survey region, i.e. approximately 18 square degrees and comprising 325 clumps with known distances and suitable CHIMPS data. We estimate the physical properties of outflows toward a large sample of massive clumps and discuss the correlations between these parameters, which are crucial in revealing the intrinsic properties and driving mechanism of outflows. Our study benefits from a homogenous and self-consistent analysis which acts to minimise systematic errors and allows us to investigate the relationship between outflows and their associated clumps in a much more unbiased manner than previous studies. This paper is organized as follows: Section 2 describes the ATLASGAL and CHIMPS surveys, and displays the sample selection process. Data analysis of the CO spectra, outflow detection and mapping are described in Section 3. In Section 4, we examine the detection statistics of the detected outflows and calculate their physical properties. Differences between clumps that are associated and not associated with outflows are discussed in Section 5 along with the physical properties of the clumps and their correlation with turbulence and outflows evolution of the clumps. We give a summary and our conclusions in Section 6.

2. THE SURVEYS AND OUR SAMPLE OF CLUMPS

2.1. *CHIMPS*

CHIMPS, the ^{13}CO/C^{18}O ($J = 3 \rightarrow 2$) Heterodyne Inner Milky Way Plane Survey, covers a region of $28^\circ \lesssim \ell \lesssim 46^\circ$ and $|b| \leq 0\overset{\circ}{.}5$ in the inner Galactic Plane (Rigby et al. 2016), has been carried out using James Clerk Maxwell Telescope (JCMT). The observations have an angular resolution of 15″ and velocity resolution of 0.5 km s^{-1} , with a median rms of ~ 0.6 K per channel. This sensitivity corresponds to column densities of $N_{\mathrm{H_2}} \sim 3 \times 10^{20}$ cm^{-2} and $N_{\mathrm{H_2}} \sim 4 \times 10^{21}$ cm^{-2} for ^{13}CO and C^{18}O, respectively. The critical density of ^{13}CO and C^{18}O is $\gtrsim 10^4$ cm^{-3} at temperatures of ≤ 20 K, and so CHIMPS is a good tracer the higher density gas associated with star formation. The ^{13}CO data from CHIMPS[5] can also be a useful tool to trace high velocity structures because it is less contaminated by other high velocity motions within star-forming complexes and is less affected by emission from diffuse clouds along the line of sight. The simultaneously observed C^{18}O is optically thin compared to ^{13}CO in the same clump, thus its peak emission is most likely to associate with the most dense center of the star-forming clump and can therefore be a good tracer of emission emanating from the dense core at the center of the clump. The CHIMPS data may therefore serve as an excellent resource for detecting molecular outflows toward clumps with massive star-formation.

2.2. *ATLASGAL*

ATLASGAL, The APEX Telescope Large Area Survey of the Galaxy, is an unbiased 870 μm submillimeter (submm) survey that covers the inner Galactic plane ($|\ell| \leq 60$ with $|b| \leq 1.5^\circ$). ATLASGAL has a resolution of 19″ and a typical noise level of 50 to 70 mJy beam^{-1} (Schuller et al. 2009). This submm survey provides the largest, unbiased database of dense clumps that can be used as a starting point for detailed studies of large numbers of massive pre- and proto-stellar clumps in the Galactic Plane. A comprehensive database of ~ 10163 massive star forming clumps has been compiled (ATLASGAL compact source catalogue (CSC); Contreras et al. 2013; Urquhart et al. 2014a) that allows us to undertake a blind search for CO outflow activity toward star-forming clumps. Furthermore, the physical properties (e.g., distance, clumps mass, column density, bolometric luminosity) of these massive star forming clumps have been measured by Urquhart et al. (2018), which allows us to conduct statistical analysis of correlations between outflow parameters and clump properties for a large and representative sample of massive star-forming clumps.

2.3. *The clump sample*

The complete region covered by the two surveys is the sky region of CHIMPS spanning $28^\circ \lesssim \ell \lesssim 46^\circ$ and $|b| \leq 0\overset{\circ}{.}5$. There are 919 ATLASGAL clumps in this region (Contreras et al. 2013; Urquhart et al. 2014a). We extract the ^{13}CO and C^{18}O spectra toward all 919 clumps using data from CHIMPS[5]. Our outflow search method requires detections in both ^{13}CO and C^{18}O, and we found a final sample of 325 clumps that fulfilled this criterion. The physical properties of 10 clumps are given in Table 2, with total 325 clumps at Appendix Table 8.

In order to show that this sample of clumps is representative of the whole, we plot their physical properties in Figure 1. The plotted quantities are the peak H$_2$ column density ($\mathrm{N_{H_2}}$) against respectively clump mass ($\mathrm{M_{clump}}$), bolometric luminosity ($\mathrm{L_{bol}}$) and luminosity-to-mass ratio ($\mathrm{L_{bol}/M_{clump}}$). These physical properties were measured by Urquhart et al. (2018). The average values of 325 clumps of $\log(\mathrm{N_{H_2}/cm^2}) = 22.45 \pm 0.36$ with a spread of 21.76 to 23.92, $\log(\mathrm{M_{clump}/M_\odot}) = 2.93 \pm 0.64$ with a spread of -0.30 to 5.04, $\log(\mathrm{L_{bol}/L_\odot}) = 3.8 \pm 1.0$ with a spread of 1.64 to 6.21, and $\log[\mathrm{L_{bol}/M_{clump}(L_\odot/M_\odot)}] = 0.89 \pm 0.62$ with a spread of -1.0 to 2.65.

Comparing the means of the two samples we find that the average values of $\mathrm{M_{clump}}$, $\mathrm{L_{bol}}$, $\mathrm{L_{bol}/M_{clump}}$ and $\mathrm{N_{H_2}}$ for the 325 clumps detected in ^{13}CO and C^{18}O are moderately larger than those of all 919 clumps (see Table 6). Kolmogorov−Smirnov (K-S) tests for these two samples suggest that they are from different parent distributions for peak column density (statistic = 0.13, and p-value $\ll 0.001$), bolometric luminosity (statistic = 0.29, p-value $\ll 0.001$), as well as luminosity-to-mass ratio (statistic = 0.33, p-value $\ll 0.001$). Distributions of clump mass of the two samples show a much smaller difference and only an 11% probability that the two are drawn from the same distribution, i.e. we cannot exclude the null hypothesis with significance.

Thus, the sample of clumps that forms the basis for our outflow search (i.e. detected in ^{13}CO and C^{18}O) have moderately higher $\mathrm{N_{H_2}}$, $\mathrm{L_{bol}}$, $\mathrm{L_{bol}/M_{clump}}$, but with similar $\mathrm{M_{clump}}$ compared to the total sample, which suggest that the selected clumps are associated with more evolved protostars (Urquhart et al. 2018). Inspecting Figure 1 shows that our outflow search sample of clumps covers almost the full observed range of properties in the parent sample as our sample has comparable minimum and maximum value of physical parameters with the parent sample (see Table 2). We are thus relatively confident that the inferences we draw are valid across the full

[5]http://dx.doi.org/10.11570/16.0001

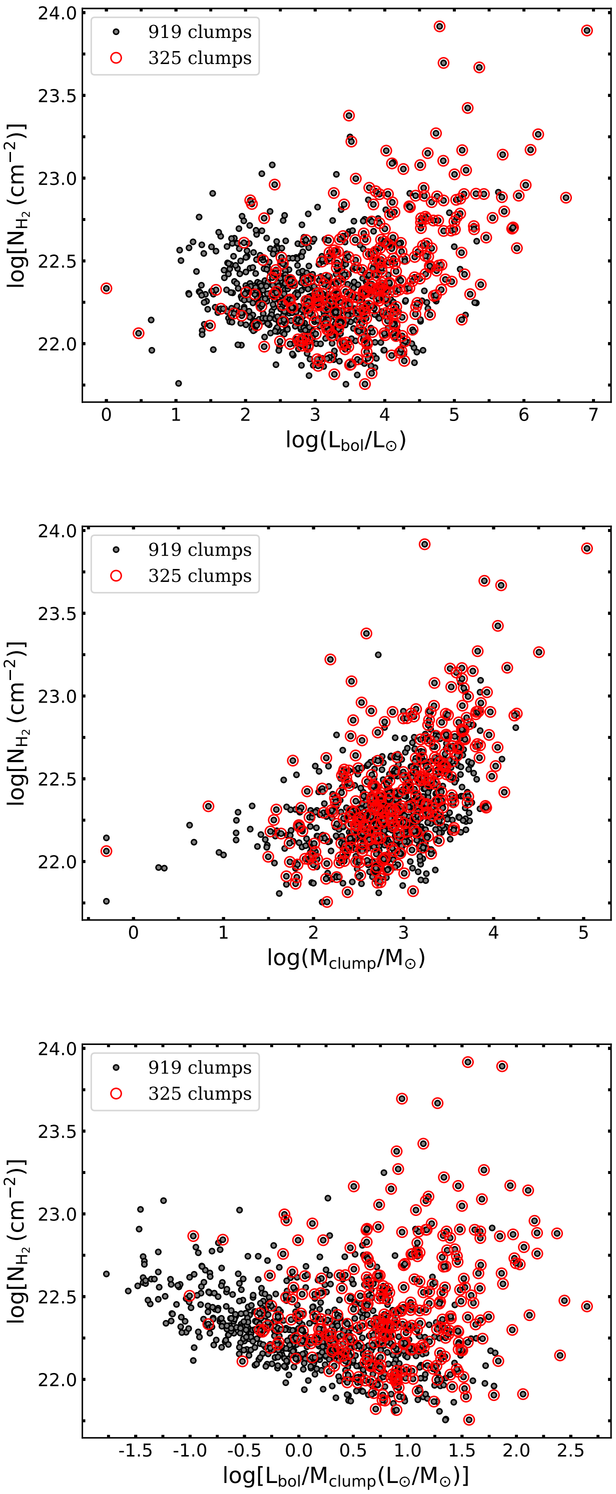

FIG. 1.— Distributions of N_{H_2}, L_{bol}, M_{clump}, and L_{bol}/M_{clump} in logarithmic scale for the selected 325 ATLASGAL clumps compared to the total 919 clumps. The range of physical parameters of the selected 325 clumps are well covered compared to the whole 919 clumps.

sample of clumps.

3. DATA ANALYSIS

TABLE 2

Clump properties of all 325 ATLASGAL clumps to search for outflows: clumps Galactic name and coordinates, integrated flux density at 870μm (F_{int}), heliocentric distance (Dist.), peak H_2 column density (N_{H_2}), bolometric luminosity (L_{bol}), clump mass (M_{clump}). These value are from Urquhart et al. (2018). Only a small part of the whole table is presented here, with full version at Appendix Table 8.

ATLASGAL CSC Gname	ℓ (°)	b (°)	F_{int} (Jy)	Dist. (kpc)	logN_{H_2} (cm^{-2})	logL_{bol} ($L_\odot$)	logM_{clump} ($M_\odot$)
G027.784+00.057	27.784	0.057	9.11	5.9	22.578	3.9	3.2
G027.796−00.277	27.796	−0.277	4.48	2.9	22.36	3.1	2.2
G027.883+00.204	27.883	0.204	9.16	8.3	22.19	3.3	3.6
G027.903−00.012	27.903	−0.012	8.36	6.1	22.437	4.2	3.1
G027.919−00.031	27.919	−0.031	2.11	3.0	21.866	3.0	1.8
G027.923+00.196	27.923	0.196	7.02	8.3	22.125	3.4	3.4
G027.936+00.206	27.936	0.206	7.48	2.7	22.416	3.4	2.3
G027.978+00.077	27.978	0.077	9.49	4.5	22.381	4.2	2.8
G028.013+00.342	28.013	0.342	1.76	8.3	21.872	3.5	2.7
G028.033−00.064	28.033	−0.064	1.98	6.1	22.133	3.0	2.6

3.1. ^{13}*CO spectrum extraction and outflow wing identification*

There are several studies that have identified high velocity outflows in ^{12}CO toward massive star forming regions (Shepherd & Churchwell 1996b; Beuther et al. 2002; Wu et al. 2004; Zhang et al. 2005). ^{13}CO has also been shown as a useful tool to detect molecular outflows because it can trace high velocity gas in crowed high-mass star forming regions where ^{12}CO can be seriously affected by confusion (Codella et al. 2004; Arce et al. 2010). The simultaneous observation of C^{18}O emission which is more optically thin and can be a good tracer of the dense cores of targets (Codella et al. 2004; de Villiers et al. 2014). In this work, we extract ^{13}CO and C^{18}O spectra from CHIMPS data cubes of an area of clump size at peak emission of each ATLASGAL clump to identify outflow activity.

The detailed strategy of identifying high-velocity outflow wings used in this study is essentially the same as that described by de Villiers et al. (2014), which has been developed from the work of van der Walt et al. (2007) and Codella et al. (2004). Here, we give a brief description of the method employed to identify outflow wings but for more details please see de Villiers et al. (2014).

We illustrate the basic steps in the procedure in Figure 2. Starting from the observed spectra of ^{13}CO (grey solid line) and C^{18}O (grey dashed line) obtained at the peak position of the ATLASGAL clump, the basic procedures to identify outflow wings are: [a] scaling the C^{18}O lines to the peak temperature of ^{13}CO, shown by the in red dash-dotted line; [b] fitting a Gaussian to the scaled the C^{18}O spectra, shown as blue dotted line; [c] obtaining ^{13}CO residuals spectra (in black solid line), by subtracting the scaled Gaussian fit C^{18}O (red dash-dotted line) from the ^{13}CO (grey solid line); [d] identify the blue and red line wings (red cross symbols) where the ^{13}CO residual is larger than 3σ, where σ is noise level of the emission-free spectrum. The line wings are defined by the velocity where the ^{13}CO profile is broader than the scaled Gaussian C^{18}O profile (core-only emission). In order to avoid subtracting any emission from high velocity structures that may be included in the scaled C^{18}O profile, a Gaussian was fitted to the scaled C^{18}O, by gradually removing points from the outer high velocity edges until the C^{18}O spectra could be fitted, as suggested by van der Walt et al. (2007) and de Villiers et al. (2014). Following the above procedures, blue wings ($6.8 - 11.8\,\mathrm{km\,s^{-1}}$) and red wings ($16.3 - 21.8\,\mathrm{km\,s^{-1}}$)

TABLE 3
^{13}CO outflow calculations of all blue and red wings for 225 ATLASGAL clumps: observed peak ^{13}CO and C^{18}O velocities, the antenna temperatures are corrected for main-beam efficiency (0.72), the velocity range $\Delta V_{b/r}$ for blue and red wings of ^{13}CO spectra, the maximum projected velocity for blue and red shifted $V_{max_{b/r}}$ relative to the peak C^{18}O velocity. Only a small part of the table is presented here, with full version at Appendix Table 9.

ATLASGAL CSC Gname	^{13}CO v_p (km s^{-1})	^{13}CO T_{mb} (K)	C^{18}O v_p (km s^{-1})	C^{18}O T_{mb} (K)	ΔV_b (km s^{-1})	ΔV_r (km s^{-1})	V_{max_b} (km s^{-1})	V_{max_r} (km s^{-1})
G027.784+00.057	101.2	5.9	100.8	1.8	[96.3,100.8]	[103.8,104.8]	4.5	4.0
G027.903−00.012	97.9	6.3	97.5	4.9	[95.3,96.8]	[98.8,100.3]	2.2	2.8
G027.919−00.031	47.6	6.1	47.7	3.7	[46.3,46.8]	[48.3,49.8]	1.4	2.1
G027.936+00.206	42.3	6.2	42.0	2.3	[37.3,40.3]	[43.8,46.8]	4.7	4.8
G027.978+00.077	74.7	4.2	75.3	2.9	[71.8,73.3]	[76.8,79.3]	3.5	4.0
G028.148−00.004	98.6	4.0	98.5	3.1	[96.3,97.8]	[99.8,100.8]	2.2	2.3
G028.151+00.171	89.7	4.8	89.6	2.1	[86.8,88.8]	[90.8,92.3]	2.8	2.7
G028.199−00.049	96.3	6.8	95.6	3.6	[89.3,95.8]	[98.3,107.3]	6.3	11.7
G028.231+00.041	107.0	3.3	107.0	1.2	[104.8,105.8]	[107.3,110.3]	2.2	3.3
G028.234+00.062	107.1	4.9	107.0	1.8	[104.8,105.8]	[107.8,108.8]	2.2	1.8

for the emission spectra of the ATLASGAL clump were determined via custom-written scripts using Astropy, a Python package for Astronomy (Astropy Collaboration et al. 2013), (see Figure 2(a) for an example toward the ATLASGAL clump G032.797+00.191).

For those ^{13}CO profiles showing clear evidence of self-absorption (e.g. G028.199−00.049 as shown in Figure 2(b)), the method was adjusted as follows. First, a Gaussian fit to the shoulders of its ^{13}CO profile (grey dash-dotted line in Figure 2(b)), and the fitted Gaussian peak is used as the true peak temperature of the ^{13}CO. This gives an indication of the expected peak to the scaled C^{18}O profile. Then following the procedures a, b, c, and d, blue wings ($89.3 - 95.8$ km s^{-1}) and red wings ($98.3 - 107.3$ km s^{-1}) are thus determined for these clumps. For more details please see Figure 2 and Figure 3 in de Villiers et al. (2014).

This method of searching for outflows is affected by uncertainties due to confusion (the observed sources lie along the Galactic plane where most of the molecular material resides), spectral noise (in the case of weak sources) and outflow geometry (which determines the width of the wings in the profile) (Codella et al. 2004). A consequence of these limitations is that we might miss some outflows, but given the homogeneity of the present sample and the large number of the observed objects, these results should be representative of the general population and therefore provide an accurate picture of the commonality of outflows and their properties.

In total, we find that 225 out of 325 clumps are associated with high velocity structures based on the method outlined above. The source velocities and blue- and red-shifted velocity ranges are given in Table 3 for a small portion of the outflows identified, with the total 225 outflows listed in Appendix Table 9. 10 of 225 sources show single red/blue high velocity wings and the remaining 215 show both blue and red wings.

Next, we created ^{13}CO integrated intensity images of each wing, integrated over the velocity ranges determined in the previous step. This is so that we can spatially separate the wing emission into distinct red and blue outflow lobes, and subsequently calculate the physical properties of the outflows using the methods presented in Section 4.2. We show two examples in Figure 3 where solid blue and dotted red contours representing blue and red outflow lobes are overlaid onto the ^{13}CO integrated intensity image (in grey scale), and the 870 μm emission from ATLASGAL shown as white contours. The ATLASGAL emission is optically thin and traces the bulk of the dense gas, revealing the column density distribution and the clump centroid.

As some massive clumps are located in clusters, their outflow properties may have been contaminated by similar high velocity component from different clumps (Shepherd & Churchwell 1996a), and their red and/or blue outflow lobes possibly mixed with other high velocity components from nearby source in the field of view. We thus exclude 48 clumps where it is difficult to identify their red and blue lobe area as the contours of outflow lobes are mixed with a complex environment. In addition, 12 sources show blue and red wings but their integrated emission is too weak to show two outflow lobes on their ^{13}CO integrated images. In summary, we have obtained outflow maps in 155 of our 215 sources, which display well-defined blue and red lobes. Excluding two sources without distances (Urquhart et al. 2018), we are left with a final sample of 153 massive clumps with mapped outflows suitable for further analysis. Outflow wings spectra of 225 clumps and ^{13}CO integrated images of 155 clumps are shown online as supporting information.

4. RESULTS

Here we present the results of our outflow search and determine the physical properties of the identified outflow sample.

4.1. *Detection Statistics of Outflows*

Among the 325 clumps in our outflow search sample, 225 of them were found to show high velocity line wings, resulting in a detection rate of $69 \pm 3\%$ for the whole sample. Within the 225 sources that show high velocity line wings, 10 clumps have a single blue/red wing and the remaining 215 have both blue and red wings. The monopolar features of the 10 clumps might be affected by uncertainties due to confusion, spectral noise, and outflow geometry (Codella et al. 2004). The detection frequency of bipolar outflows is subsequently reduced to $\sim 66 \pm 3\%$.

This detection rate is comparable to Maud et al. (2015) (66%) and Zhang et al. (2001, 2005) (57%), which may be due to the similarity of the evolutionary stages of our sample with Maud et al. (2015), i.e., compact Hɪɪ regions or MYSOs, and in luminosity with Zhang et al. (2001, 2005), i.e., $10^2 L_\odot \sim 10^5 L_\odot$. This detection rate is slightly larger than Codella et al. (2004) (39%∼50%) partly because they include a number of sources at later stage of ultra-compact (UC) Hɪɪ regions when outflows tend to disappear (Codella et al. 2004). Our detection rate is slightly smaller than some previous results (e.g., Shepherd & Churchwell 1996b; Beuther et al. 2002; López-Sepulcre et al. 2009; de Villiers et al. 2014), likely due

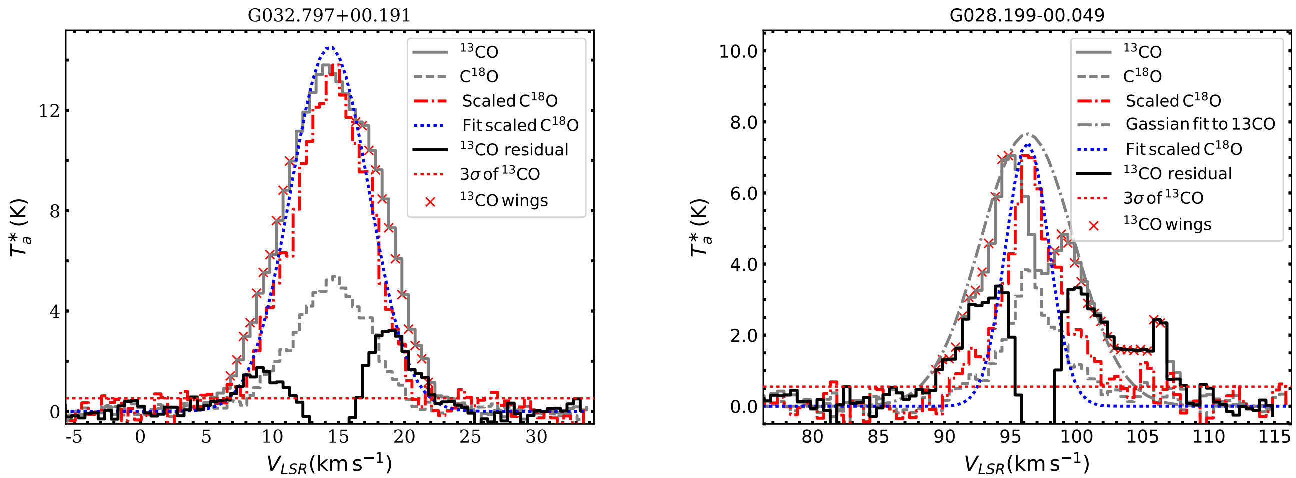

FIG. 2.— Left panel(a): an example of outflow wing selection by using spectra of the ^{13}CO (grey solid line) and C^{18}O (grey dashed line) for the ATLASGAL clump G032.797+00.191. Blue wings and red wings identification process: [a] scaling the C^{18}O spectrum to ^{13}CO peak, shown by red dash-dotted line; [b], fitting a Gaussian to the scaled C^{18}O, shown as blue dotted line; [c], obtaining ^{13}CO residuals spectra in black solid line, by subtracting the Gaussian fit to scaled C^{18}O (red dash-dotted) from ^{13}CO (grey solid line); [d], Blue wings (6.8 – 11.8 km s^{-1}) and red wings (16.3 – 21.8 km s^{-1}), shown as red cross symbols, can be determined from where the^{13}CO residuals are larger than the 3σ line. σ is noise level of the emission-free spectrum. Right panel(b): an example of outflow wings selection toward ATLASGAL clump G028.199−00.049 that ^{13}CO profile shows clear evidence of self-absorption. First, a Gaussian fit to the shoulders of ^{13}CO spectra, in grey dash-dotted line, and the fitted Gaussian is used as true peak temperature of the ^{13}CO. This indicates the expected actual peak for the scaled C^{18}O spectra. Then following the above procedures a b c, and d, blue wings (89.3 – 95.8 km s^{-1}) and red wings (98.3 – 107.3 km s^{-1}) are thus determined for G028.199−00.049. More details please see Figure 2 and Figure 3 in de Villiers et al. (2014).

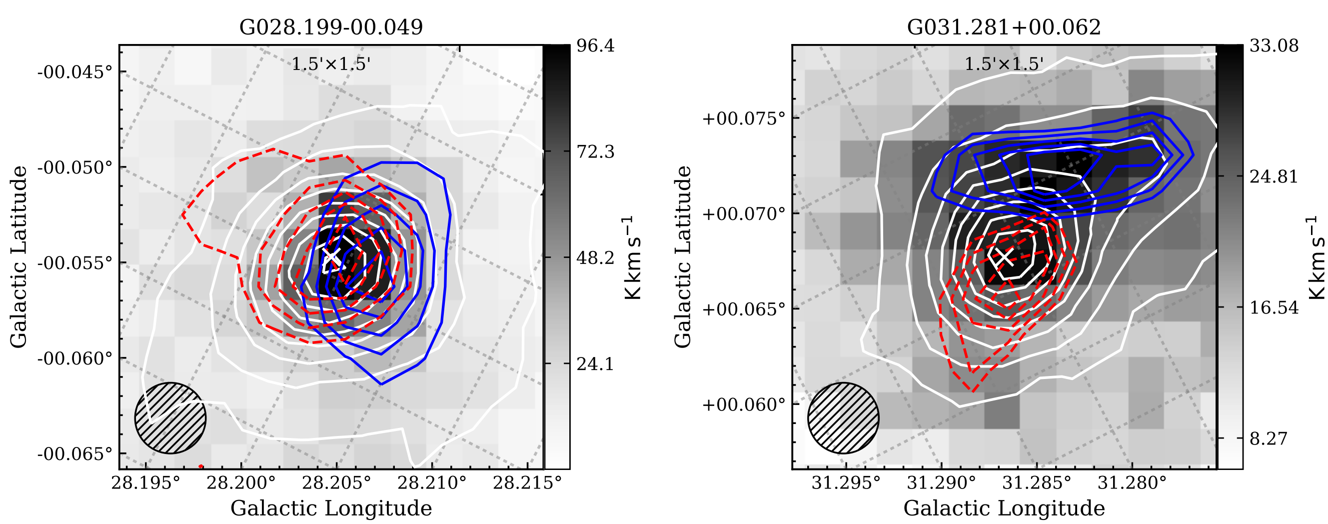

FIG. 3.— Examples of the outflow mapping: the intensity integrated image (1.5′ × 1.5′) of the blue and red wings centered on the symbol of white cross at the ATLASGAL clump G028.199−00.049 (left-hand panel) and G031.281+00.062 (right-hand panel). Grey scale images shows ^{13}CO integrated emission, with blue wings (blue solid line) and red wings (red dashed lines). These wings emission are integrated with velocity ranges of 101.2 – 104.2 km s^{-1} (blue wings), 111.2 – 112.7 km s^{-1} (red wings) for G031.281+00.062 and 89.3 – 95.8 km s^{-1} (blue wings), 98.3 – 107.3 km s^{-1} (red wings) for G028.199−00.049, respectively. Red and blue contours have been divided by 5/6 levels with starting value 3σ or 30% of maximum intensity, and ending value 95% of maximum intensity with unit of K km s^{-1}. White contours show emission from 870μm ATLASGAL with levels determined by a dynamic range power-law fitting scheme (Thompson et al. 2006). The beam of CHIMPS (15″) is shown by the hatched black circle presented in the lower left of each image.

TABLE 4
[13]CO outflow properties of all blue and red lobes for 153 ATLASGAL clumps : blue/red lobe length $l_{b/r}$ [pc], masses M_b(blue), M_r(red), M_{out}(M_{out} = M_b + M_r)[$M_\odot$], momentum p[10 $M_\odot$ km s^{-1}], energy E[10^{39} J], dynamic time t_d[10^4 yr], mass entrainment rates $\dot{M}_{out}$[10^{-4} $M_\odot$/yr], mechanical force F_{CO}[10^{-3} $M_\odot$ km s^{-1}/yr], and mechanical luminosity L_{CO}[$L_\odot$]. Only a small part of the whole table is presented here, with full version at Appendix Table 10.

ATLASGAL CSC Gname	l_b (pc)	l_r (pc)	M_b ($M_\odot$)	M_r ($M_\odot$)	M_{out} ($M_\odot$)	p (10 $M_\odot$ km s^{-1})	E (10^{39} J)	t_d (10^4 yr)	$\dot{M}_{out}$ ($10^{-4}M_\odot$/yr)	F_{CO} ($10^{-3}M_\odot$ km s^{-1}/yr)	L_{CO} ($L_\odot$)
G027.784+00.057	1.1	0.6	39.4	5.4	44.8	20.8	2.4	14.8	2.9	1.2	1.2
G027.903−00.012	0.8	1.0	18.8	18.8	37.6	14	0.8	24.5	1.5	0.6	0.28
G027.919−00.031	0.5	0.5	3.0	9.5	12.4	4.6	0.16	16.0	0.7	0.2	0.08
G027.936+00.206	0.2	0.2	1.9	3.2	5.1	3.8	0.4	3.1	1.6	1.2	0.8
G027.978+00.077	0.5	1.0	7.4	13.3	20.7	12.6	1.2	16.1	1.2	0.8	0.4
G028.148−00.004	0.5	0.6	5.4	8.5	13.9	5.0	0.32	14.6	0.9	0.4	0.16
G028.151+00.171	0.6	1.2	6.0	2.7	8.7	4.0	0.28	25.5	0.3	0.14	0.08
G028.199−00.049	0.8	1.5	83.5	86.0	169.5	176.0	38.8	9.7	16.8	16.6	30.8

TABLE 5
Detection rate versus bins range of $M_{clump}(M_\odot)$, $L_{bol}(L_\odot)$, $L_{bol}/M_{clump}(L_\odot/M_\odot)$, $N_{H_2}(cm^2)$

$\log M_{clump}$	$\log L_{bol}$	$\log[L_{bol}/M_{clump}]$	$\log N_{H_2}$
[-0.30,2.31]61 ± 7%	[0.0,2.89] 52 ± 8%	[-1.00,0.20]52 ± 8%	[21.76,22.06]61 ± 7%
[2.31,2.60] 69 ± 7%	[2.89,3.30]53 ± 7%	[0.20,0.62] 49 ± 7%	[22.06,22.22]49 ± 7%
[2.60,2.78] 56 ± 7%	[3.30,3.70]62 ± 7%	[0.62,0.78] 71 ± 7%	[22.22,22.32]56 ± 7%
[2.78,3.05] 57 ± 7%	[3.70,3.96]70 ± 7%	[0.78,0.98] 69 ± 7%	[22.32,22.42]55 ± 8%
[3.05,3.30] 76 ± 6%	[3.96,4.25]73 ± 7%	[0.98,1.26] 82 ± 6%	[22.42,22.58]76 ± 6%
[3.30,3.59] 69 ± 7%	[4.25,4.77]80 ± 6%	[1.26,1.51] 78 ± 6%	[22.58,22.84]89 ± 5%
[3.59,5.04] 96 ± 3%	[4.77,6.91]91 ± 4%	[1.51,2.65] 82 ± 6%	[22.84,23.92]96 ± 3%

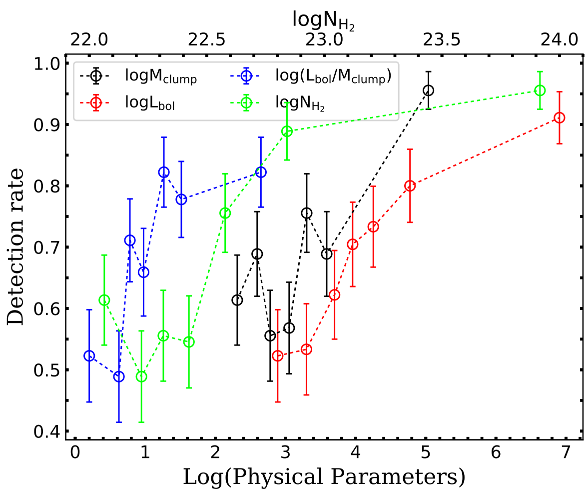

FIG. 4.— Detection rate as a function of clump mass $M_{clump}(M_\odot)$, bolometric luminosity of central objects $L_{bol}(L_\odot)$, luminosity-to-mass ratio $L_{bol}/M_{clump}(L_\odot/M_\odot)$, and the peak H_2 column density of clumps $N_{H_2}(cm^{-2})$ in logarithmic scales. The values on x-axis for these parameters correspond to the bins value from the second to the end value, while $\log N_{H_2}$ show bins values on the top x-axis from the second to end. The bins value and detection rate are presented in Table 5

to the fact that they are targeted observations toward markers of massive star formation.

ATLASGAL clumps were classified into an evolutionary sequence based on their infrared to radio SED into four types by König et al. (2017) and Urquhart et al. (2018), including the youngest quiescent phase (i.e., a starless or pre-stellar phase with 70μm weak), protostellar (i.e., clumps with mid-infrared 24μm weak but far-infrared bright), YSO-forming clumps (YSO clumps; i.e., mid-infrared 24μm bright clumps), and massive star formation clumps (MSF clumps; i.e., mid-infrared 24μm bright clumps with a massive star formation tracer). Among our outflow search sample of 325 clumps, with the exception of 6 clumps that have not yet been classified, there are 125 MSF, 171 YSO, 19 protostellar, and 4 quiescent clumps. We detect outflow line wings towards 102 (102/125; 82 ± 3%) MSF clumps, 105 (105/171; 61 ± 4%) YSO clumps, 10 protostellar clumps (10/19; 53 ± 11%), and 2 quiescent clumps (2/4; 50 ± 25%) respectively.

Looking at the MSF subsample in more detail, there are 56 clumps associated with ultra-compact (UC) H II regions from Urquhart et al. (2013), 52 of which are found to have high velocity line wings (93 ± 3%). 4 clumps are associated with 4 hypercompact (HC) H II regions (Sewilo et al. 2004; Zhang et al. 2014; Keto et al. 2008; Sewiło et al. 2011) of which 100% show high velocity line wings. 70 clumps are associated with maser (water or methanol) emissions (Codella et al. 2004; Urquhart et al. 2014b; de Villiers et al. 2014; Urquhart et al. 2018) and 60 of the 70 maser associated clumps (86 ± 4%) are associated with high velocity line wings, which is consistent with the detection rate for maser associated sources in Codella et al. (2004) and de Villiers et al. (2014). These high detection rates confirm that outflows are a common feature in the early stages of massive star formation, as suggested in many previous studies (Shepherd & Churchwell 1996a; Kurtz et al. 2000; Beuther et al. 2002; Molinari et al. 2002; Wu et al. 2004).

Among the 325 total clumps and 225 outflow-associated clumps, 314 and 216 respectively have measured distances and hence physical parameters from Urquhart et al. (2018). We are therefore able to examine the detection rate as a function of clump mass (M_{clump}), bolometric luminosity of central objects (L_{bol}), luminosity-to-mass ratio (L_{bol}/M_{clump}), and the peak H_2 column density of clumps (N_{H_2}); these are shown in Figure 4. For each parameter, we divide the clumps into 7 bins covering the minimum to maximum values in Table 6 and then determine the detection fraction for each bin (see Table 5). The results are plotted in Figure 4 showing the detection rate increases from ~ 50% to ~ 90% as clump evolves, which reveals an obvious trend in that more massive, luminous, dense, and evolved sources show a much higher outflow detection fraction.

Our overall detection rate of 69 ± 3% for the whole sample is probably a lower limit due to the sensitivity of CHIMPS and the inclusion of less massive clumps that may not be capable of forming massive stars (e.g., roughly 8% clumps in this sample have masses $M_{clump} < 100\,M_\odot$ with the fraction of low-mass clumps higher than in other studies (e.g., Beuther et al. 2002; de Villiers et al. 2014)). This explains why the overall detection rate determined in this work is lower than previously reported in the literature (Shepherd & Churchwell 1996b; Beuther et al. 2002; Kim & Kurtz 2006; López-Sepulcre et al. 2009; de Villiers et al. 2014) as the previous literature samples were very specifically targeted towards markers of massive star formation, and outflows are said to be ubiquitous properties of massive star formation. Our unbiased survey reveals strong selection functions in the outflow detection fraction in luminosity, clump mass, column density and luminosity-to-mass ratio. At later evolutionary stages of the central objects in the clumps, the detection rates of outflows in our sample can be as high as 90% when $L_{bol}/M_{clump} > 10\,(L_\odot/M_\odot)$, $L_{bol} > 2.7\times10^4\,L_\odot$, $M_{clump} > 3.9\times10^3\,M_\odot$, and $N_{H_2} > 3.8\times10^{22}\,cm^{-2}$. In particular, the rise in the fraction of detected outflows with peak H_2 column density at $\log N_{H_2} > 22.2\,cm^{-2}$ (or $\sim 250\,M_\odot\,pc^{-2}$), is larger than the concept of a surface density threshold for efficient star formation of $\sim 120\,M_\odot\,pc^{-2}$ as found by Lada et al. (2010) and Heiderman et al. (2010).

4.2. *Determination of outflow parameters*

The physical properties of outflows provide useful information on the energy and mass exchange process, and have been derived by many previous works (e.g. de Villiers et al. 2014; Beuther et al. 2002; Cabrit & Bertout 1990). Following the strategy outlined by de Villiers et al. (2014), we make the following assumptions: (1), the J = 3 − 2 transition temperature of ^{13}CO $T_{trans} = 31.8$ K (Minchin et al. 1993) and excitation temperature $T_{ex} = 35$ K (e.g. Shepherd & Churchwell 1996a; Henning et al. 2000; Beuther et al. 2002). (2), the ^{13}CO line wings are optically thin. The column density of ^{13}CO may thus be written as (Curtis et al. 2010a):

$$N\left(^{13}\mathrm{CO}\right) = 5\times10^{12} T_{ex} \exp\left(\frac{T_{trans}}{T_{ex}}\right) \int T_{mb} dv\ (\mathrm{cm}^{-2}), \quad (1)$$

where $\int T_{mb} dv$ is calculated from the mean temperature of ^{13}CO within the outflow lobe area defined by the lowest contours, dividing it by the main beam correction factor of 0.72 from CHIMPS (Rigby et al. 2016). The abundance ratios of $[CO]/[H_2] = 10^{-4}$ (Frerking et al. 1982) and $[^{12}CO]/[^{13}CO] = 7.5D_{gal} + 7.6$, where D_{gal} is Galactocentric distance in kiloparsec (Wilson & Rood 1994), are used to convert to the H_2 column density. The column density $N(H_2)$ is, therefore, given by:

$$N(H_2) = (7.5D_{gal} + 7.6) \times 10^4 N(^{13}CO). \qquad (2)$$

The $N(H_2)$ column densities of the blue and red lobes ($N_{b/r}$) are then used to calculate the mass of each lobe ($M_{b/r}$), and then obtain the total outflow mass M_{out},

$$M_{out} = M_r + M_b = (N_b \times A_b + N_r \times A_r)\, m_{H_2}, \qquad (3)$$

where $A_{b/r}$ is the surface area of each lobe and m_{H_2} is the mass of a hydrogen molecule. The surface area of each lobe is calculated using the same threshold used to calculate T_{mb}, defined by the lowest contours.

For each pixel in the defined outflow lobe area, we calculate the outflow momentum and energy per velocity channel (Δv), by using the channel velocity relative to the systemic velocity (v_i) and gas mass (M_i) corresponding to the emission in that channel. The outflow momentum and energy can thus be obtained by summing their corresponding value over all velocity channels,

$$p = \sum_{A_b}\left[\sum_{i=v_b} M_{b_i} v_i\right]\Delta v + \sum_{A_r}\left[\sum_{i=v_r} M_{r_i} v_i\right]\Delta v \qquad (4)$$

$$E = \frac{1}{2}\sum_{A_b}\left[\sum_{i=v_b} M_{b_i} v_i^2\right]\Delta v + \frac{1}{2}\sum_{A_r}\left[\sum_{i=v_r} M_{r_i} v_i^2\right]\Delta v. \qquad (5)$$

The maximum characteristic length l_{max} refers to the maximum length of each outflow lobe $l_{b/r}$ that is measured from the clump centroid to each extreme of each lobe. Therefore, we can estimate the dynamic time scale t_d, the mass rate of the molecular outflow $\dot{M}_{out}$, the mechanical force F_{CO} and the mechanical luminosity L_{CO} using the following equations:

$$t_d = \frac{l_{max}}{(V_{maxb} + V_{maxr})/2}. \qquad (6)$$

$$\dot{M}_{out} = \frac{M_{out}}{t} \qquad (7)$$

$$F_{CO} = \frac{p}{t} \qquad (8)$$

$$L_{CO} = \frac{E}{t}, \qquad (9)$$

where V_{maxb} and V_{maxr} is the maximum blue and red velocities relative to the peak $C^{18}O$ velocity (see Table 3). Please see de Villiers et al. (2014) for further details. We adopt an average inclination angle of $\theta = 57.3°$ to correct the results for the unknown angle between the flow axis and the line of sight (Beuther et al. 2002; Zhang et al. 2005). The inclination-corrected physical properties of outflows with mapped blue and red lobes are listed in Table 4 for a small portion, and the properties of total 153 outflows are shown in Appendix Table 10.

TABLE 6
Summary of physical parameters of clumps and outflows. In Columns (2-5) we give the minimum, maximum, mean ± standard deviation, and median values of these parameters for each subsample. The physical parameters of clump are measured by Urquhart et al. (2018)

Parameter	x_{min}	x_{max}	$x_{mean} \pm x_{std}$	x_{med}
919 ATLASGAL clumps in CHIMPS				
$\log(M_{clump}/M_\odot)$	-0.30	5.04	2.84 ± 0.62	2.88
$\log(L_{bol}/L_{bol})$	0.00	6.91	3.19 ± 0.99	3.15
$\log[L_{bol}/M_{clump}(L_\odot/M_\odot)]$	-1.77	2.65	0.35 ± 0.79	0.39
$\log(N_{H_2}/cm^2)$	21.76	23.92	22.35 ± 0.29	22.30
325 clumps with good data				
$\log(M_{clump}/M_\odot)$	-0.30	5.04	2.93 ± 0.64	2.93
$\log(L_{bol}/L_{bol})$	0.00	6.91	3.82 ± 0.96	3.82
$\log[L_{bol}/M_{clump}(L_\odot/M_\odot)]$	-1.00	2.65	0.89 ± 0.62	0.90
$\log(N_{H_2}/cm^2)$	21.76	23.92	22.45 ± 0.36	22.36
225 clumps with outflows				
$\log(M_{clump}/M_\odot)$	1.50	4.5	3.00 ± 0.61	3.05
$\log(L_{bol}/L_{bol})$	1.64	6.21	3.99 ± 0.90	3.96
$\log[L_{bol}/M_{clump}(L_\odot/M_\odot)]$	-0.97	2.65	0.99 ± 0.61	0.99
$\log(N_{H_2}/cm^2)$	21.82	23.92	22.51 ± 0.37	22.47
100 clumps without outflows				
$\log(M_{clump}/M_\odot)$	-0.30	5.04	2.77 ± 0.66	2.77
$\log(L_{bol}/L_{bol})$	0.00	6.91	3.44 ± 0.98	3.42
$\log[L_{bol}/M_{clump}(L_\odot/M_\odot)]$	-1.00	2.37	0.67 ± 0.61	0.74
$\log(N_{H_2}/cm^2)$	21.76	23.89	22.28 ± 0.27	22.25
Outflow properties for 153 clumps with further analysis				
$M_{out}/M_\odot$	1.36	2065.26	121.16 ± 250.82	45.89
ℓ_{max}/pc	0.20	3.02	1.10 ± 0.57	0.99
t_d (10^5 yr)	0.25	8.90	1.78 ± 1.30	1.51
$\dot{M}_{out}$ ($10^{-4} M_\odot$/yr)	0.08	172.34	9.26 ± 21.11	2.72
p ($10\,M_\odot$ km s^{-1})	0.54	2964.65	124.76 ± 359.60	23.39
E (10^{39} J)	0.02	786.51	20.45 ± 79.91	2.00
L_{CO} ($L_\odot$)	0.01	502.88	14.71 ± 53.28	0.89
F_{CO} ($10^{-3}\,M_\odot$ km s^{-1} yr^{-1})	0.03	225.26	9.98 ± 28.65	1.32

In Table 6 we give a summary of the maximum, minimum, median and standard deviation of the distribution of the clump properties with and without outflows and also the outflow properties of the 153 clumps with mapped outflow lobes. The outflows from our survey have a similar range of physical properties to previously studied massive outflows (e.g., Zhang et al. 2005; Beuther et al. 2002; Wu et al. 2004; de Villiers et al. 2014), and are more than 2 orders of magnitude more massive and more energetic than low-mass outflows (e.g., Bontemps et al. 1996; Wu et al. 2004; Arce et al. 2007; Bjerkeli et al. 2013). The mean outflow mass-loss rates imply a mean accretion rate of $\sim 10^{-4}\,M_\odot\,yr^{-1}$ (Beuther et al. 2002; de Villiers et al. 2014), which agrees with the accretion rates predicted by theoretical models of massive star formation (e.g., Bonnell et al. 2001; Krumholz et al. 2007).

Typically, the uncertainties on derived outflow physical properties are a factor ~ 3 on outflow mass M_{out}, a factor of ~ 10 on mechanical force F_{CO}, and a factor of ~ 30 on mechanical luminosity L_{CO}, in previous studies (e.g., Cabrit & Bertout 1990; Shepherd & Churchwell 1996a; Beuther et al. 2002; Wu et al. 2004; de Villiers et al. 2014). These are mainly due to uncertainties in distance, $^{12}CO/H_2$, T_{ex}, and inclination angles (Cabrit & Bertout 1990). The uncertainty in kinematic distance described by Urquhart et al. (2018) could also have a large influence on these parameters. However, many of these uncertainties are systematic and so are unlikely to have a significant affect on the overall distribution and correlations between individual quantities. Therefore, the homogeneity of our sample and the large number of the observed objects should ensure any results drawn from our statistical analysis are robust.

5. DISCUSSION

5.1. *Outflow activity as a function of MYSO evolutionary state*

The outflow properties presented in Section 4.1 allow us to investigate at which stage outflows "switch on" and how outflow properties change with respect to different evolutionary phases. Interestingly, 2 clumps in the youngest quiescent stage, i.e., 70μm weak (Urquhart et al. 2018), show outflow wings, which suggests some clumps that are in a quiescent stage are associated with outflow activity and therefore may be in a very early protostellar stage. This is supported by Feng et al. (2016) and Tan et al. (2016), who have reported bipolar outflow toward a high-mass protostar associated with a 70μm dark source. This makes these two 70μm weak clumps interesting candidates to investigate outflow activity in the earliest stages of a protostars evolution in more detail.

There is a clear trend for increasing detection frequency of outflows along the four evolutionary sequences, i.e., from the youngest quiescent (50 ± 25%) to protostellar (53 ± 11%), to YSO (61 ± 4%), and then to MSF clump (82 ± 3%). This suggests that outflow activity becomes much more common as clumps evolve. A detailed study of the subgroup MSF clump (i.e., mid-infrared 24μm bright clump associated with a massive star formation tracer), higher detection rates occurred for subclass of hypercompact Hii regions associated clumps (100%), ultracompact Hii regions associated clumps (93 ± 3%), and masers associated clumps (86 ± 4%). For masers associated clumps, the detection rate is 100% (i.e., 11/11) for water-maser-associated clumps and 86 ± 3% (i.e., 53/63) for methanol-maser-associated clumps, and 100% (i.e., 4/4) for water-methanol-maser-associated clumps. For maser-associated UC Hii regions, the detection rate is 100% (i.e., 27/27) and reduces to 86 ± 4% (i.e., 25/29) for non-maser-associated UC Hii regions. Therefore, in the MSF clump group, the detection rate can be very high ∼ 90% up to 100% for pre-UC Hii (e.g., HC Hii regions (Kurtz 2005), water and/or methanol masers (Codella et al. 2004; König et al. 2017)), and early UC Hii region phase (e.g., maser associated UC Hii regions(Codella et al. 2004)). Then, outflow detection frequency is likely to decrease as the UC Hii region evolves, which is also supported by the decreasing outflow activity at the end of the UC Hii region stage reported by Codella et al. (2004).

In summary, the outflow detection rate is increasing as the clumps evolve in this young sample (see Figure 4), and appears to peak (100%) at the pre-UC Hii region or early UC Hii region stage. However, there are a few clumps at a later stage of evolution, with large values of L/M and which are associated with complex star formation region in the Galactic plane (e.g., G043.166+00.01 in W49A), that show no evidence for outflow wings. The non-detection of outflows towards these sources may be due to the complexity of the CO emission (e.g., Zhang et al. 2001), interactions of the sources within the clumps below our resolution (e.g., Codella et al. 2004), or external winds/shocks (e.g., Maud et al. 2015). However, these non-outflow sources with high L/M show extended emission or be part of extended emission at 1.4 GHz MAGPIS survey (Helfand et al. 2006). The high L/M may also indicate that the Hii region has started to disrupt their environment and that the central YSOs are no longer accreting.

5.2. *Comparison between clumps with and without outflows*

Our search for high velocity line wings in the outflow search sample allows us to divide clumps into two subsamples, those that are associated with outflows and those that are not. In Fig. 5 we present histograms that compare the distribution of the physical properties of the clumps associated with outflows (red) and unassociated clumps (blue). The average properties for the two samples are summarised in Table 6. It is clear from these Figure 5 that the clumps associated with outflows are significantly more massive, have higher column densities and host more luminous and evolved objects. K-S tests confirm these two samples are significantly different from each other (p-values $\ll 0.001$). This implies that clumps with more luminous central sources are much more likely to be associated with outflows than those clumps hosting lower luminosity central sources. This is consistent with the study by Urquhart et al. (2014b) who found that the more massive and dense clumps are more likely to be associated with MYSOs and H ii regions and therefore more likely to be associated with outflows.

5.3. *Comparison of outflow parameters to properties of their corresponding clumps*

Our large homogenous and uniformly selected sample allow us to examine the correlation between the physical properties of the outflows and the properties of their corresponding clumps properties. As most of the derived physical properties depend on the distance to the clump we use a nonparametric measure of the statistical dependence to measure their correlation and allow for the effects of distance being a common variable between parameters. We use Spearman's rank correlation coefficient (ρ) to control the effect of distance-dependent parameters (Kim & Yi 2006). The results of these correlations are listed in Table 7. The relations between outflow properties and their natal clump mass, bolometric luminosity, luminosity-to-mass ratio are shown in Figure 6 to Figure 9.

5.3.1. M_{out} *versus* M_{clump}, L_{bol}, *and* L_{bol}/M_{clump}

The mass of the outflow is a fundamental parameter, and we plot the relation between outflow mass M_{out} and clump properties M_{clump}, L_{bol}, and L_{bol}/M_{clump} in the upper, middle and lower panels of Figure 6. The correlation coefficients and results of linear fits to the data are presented in Table 7. A similar relation ($M_{out} \propto M_{clump}^{0.8}$) has been reported by de Villiers et al. (2014) for 44 methanol maser associated objects using the same method as this work. Beuther et al. (2002) reported a correlation of $M_{out} \sim 0.1 M_{clump}^{0.8}$ for 21 high-mass star-forming regions. López-Sepulcre et al. (2009) gave a correlation of $M_{out} = 0.3 M_{clump}^{0.8}$ for 11 very luminous objects, with their clump masses derived from $C^{18}O$ and millimetre-wave dust emission. Sánchez-Monge et al. (2013) found a similar relation as López-Sepulcre et al. (2009) for 14 high-mass star-forming regions, with outflow masses derived from SiO and clump masses from infrared SED fits. The correlation derived from our sample of 153 massive clumps ($M_{out} \propto M_{clump}^{0.6\pm0.06}$) is similar to these previous results, while the marginally shallower index most likely results from a larger range of clump masses and wider spread of evolutionary stages in this work. The ratio of M_{out}/M_{clump} has a median value of 0.05 for the sample, and 92% of the sample have the ratio in 0.005 ∼ 0.32. Thus, approximately 5% of the core gas is entrained in the molecular outflow, which is similar to the mean entrainment ratio of 4% in Beuther et al. (2002).

The correlation between M_{out} and L_{bol} (ρ = 0.66) suggests

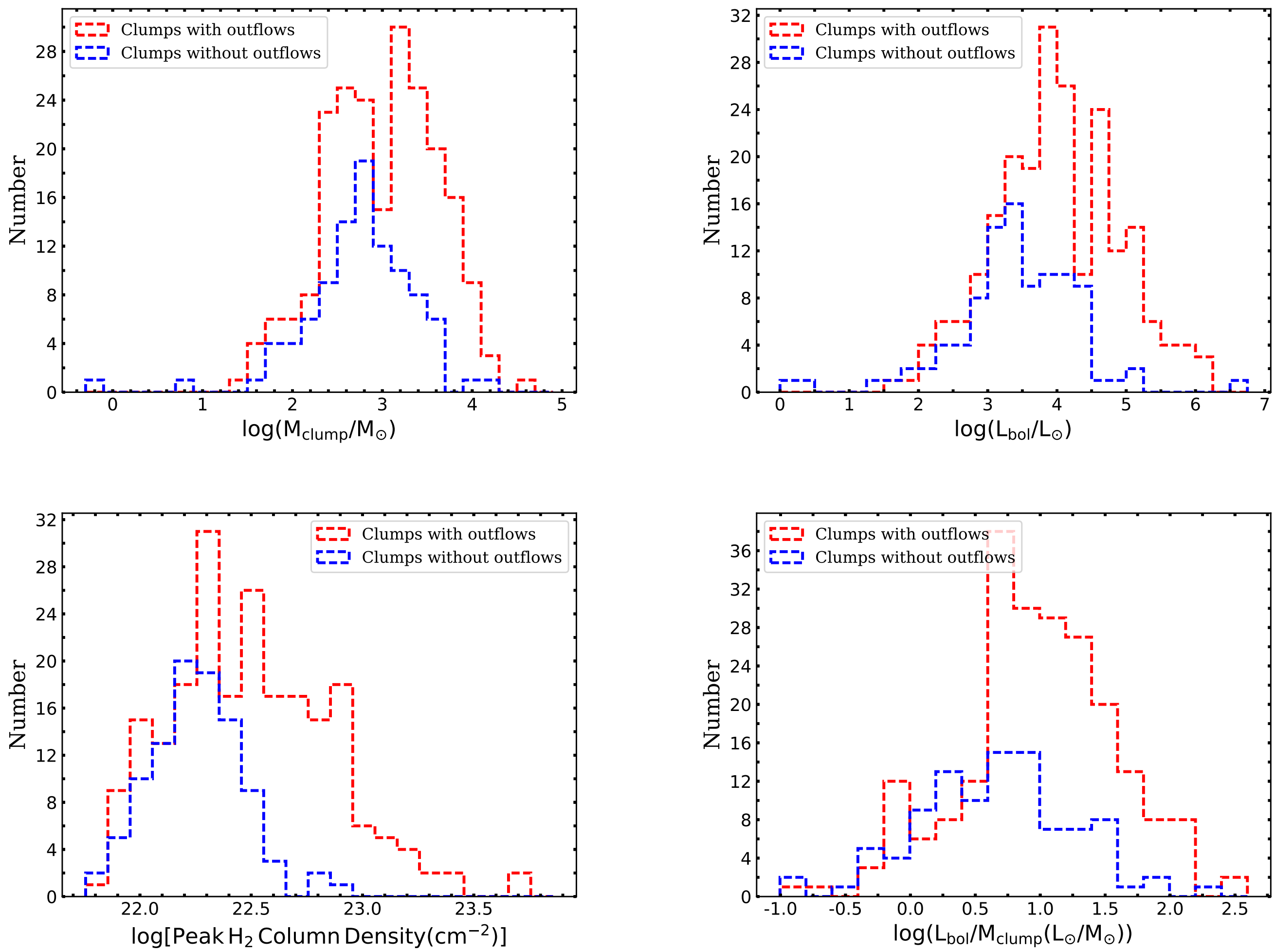

FIG. 5.— Top-left to Bottom-right: logarithmic distributions of the clump mass ($M_{clump}/M_{\odot}$), bolometric luminosity ($L_{bol}/L_{\odot}$), the peak H_2 column density (N_{H_2}/cm^2), and luminosity-to-mass ratio ($L_{bol}/M_{clump}(L_{\odot}/M_{\odot})$), for the 225 outflows clumps (red dashed line) compared to the 100 clumps without outflows (blue dashed line). The bin size is 0.2 dex, 0.25 dex, 0.1 dex, and 0.2 dex from top-left to bottom-right. The L/M ratio is a well-identified indicator of clumps evolution with larger value for more evolved clump, and the peak H_2 column density show a very strong positive correlation with the fraction of clumps associated with massive star formation (Urquhart et al. 2018).

TABLE 7
Outflow Parameters versus Clump Properties.
We use non-parametric Spearman's rank correlation test to determine the level of correlation between these distance-dependent parameters when take distance as the control variable. The p-value gives the significance of all correlations and is lower than 0.0013 for a significant correlation. If a significant correlation is found, we fit the data in log-log space using a linear least-squares fit method.

Relations	Spearman's Rank Correlation			Linear least-square fits
	ρ	p-value	control variable	log-log space
M_{out} vs M_{clump}	0.35	$\ll 0.001$	Dist.	$\log(M_{out}/M_{\odot}) = (0.6 \pm 0.06)\log(M_{clump}/M_{\odot}) - (0.2 \pm 0.20)$
M_{out} vs L_{bol}	0.66	$\ll 0.001$	Dist.	$\log(M_{out}/M_{\odot}) = (0.5 \pm 0.03)\log(L_{bol}/L_{\odot}) - (0.3 \pm 0.13)$
M_{out} vs L_{bol}/M_{clump}	0.59	$\ll 0.001$	Dist.	$\log(M_{out}/M_{\odot}) = (0.6 \pm 0.07)\log(L_{bol}/M_{clump}(L_{\odot}/M_{\odot})) + (1.1 \pm 0.08)$
$\dot{M}_{out}$ vs M_{clump}	0.47	$\ll 0.001$	Dist.	$\log(\dot{M}_{out}/M_{\odot}yr^{-1}) = (0.6 \pm 0.07)\log(M_{clump}/M_{\odot}) - (5.3 \pm 0.20)$
$\dot{M}_{out}$ vs L_{bol}	0.80	$\ll 0.001$	Dist.	$\log(\dot{M}_{out}/M_{\odot}yr^{-1}) = (0.6 \pm 0.03)\log(L_{bol}/L_{\odot}) - (5.7 \pm 0.13)$
$\dot{M}_{out}$ vs L_{bol}/M_{clump}	0.68	$\ll 0.001$	Dist.	$\log(\dot{M}_{out}/M_{\odot}yr^{-1}) = (0.7 \pm 0.06)\log(L_{bol}/M_{clump}(L_{\odot}/M_{\odot})) - (4.2 \pm 0.07)$
F_{CO} vs M_{clump}	0.51	$\ll 0.001$	Dist.	$\log(F_{CO}/M_{\odot}\,km\,s^{-1}yr^{-1}) = (0.8 \pm 0.09)\log(M_{clump}/M_{\odot}) - (5.1 \pm 0.30)$
F_{CO} vs L_{bol}	0.79	$\ll 0.001$	Dist.	$\log(F_{CO}/M_{\odot}\,km\,s^{-1}yr^{-1}) = (0.7 \pm 0.04)\log(L_{bol}/L_{\odot}) - (5.5 \pm 0.17)$
F_{CO} vs L_{bol}/M_{clump}	0.65	$\ll 0.001$	Dist.	$\log(F_{CO}/M_{\odot}\,km\,s^{-1}yr^{-1}) = (0.9 \pm 0.08)\log(L_{bol}/M_{clump}(L_{\odot}/M_{\odot})) - (3.6 \pm 0.10)$
L_{CO} vs M_{clump}	0.54	$\ll 0.001$	Dist.	$\log(L_{CO}/L_{\odot}) = (1.0 \pm 0.10)\log(M_{clump}/M_{\odot}) - (2.8 \pm 0.3)$
L_{CO} vs L_{bol}	0.79	$\ll 0.001$	Dist.	$\log(L_{CO}/L_{\odot}) = (0.8 \pm 0.05)\log(L_{bol}/L_{\odot}) - (3.2 \pm 0.2)$
L_{CO} vs L_{bol}/M_{clump}	0.62	$\ll 0.001$	Dist.	$\log(L_{CO}/L_{\odot}) = (1.1 \pm 0.1)\log(L_{bol}/M_{clump}(L_{\odot}/M_{\odot})) - (1.0 \pm 0.1)$

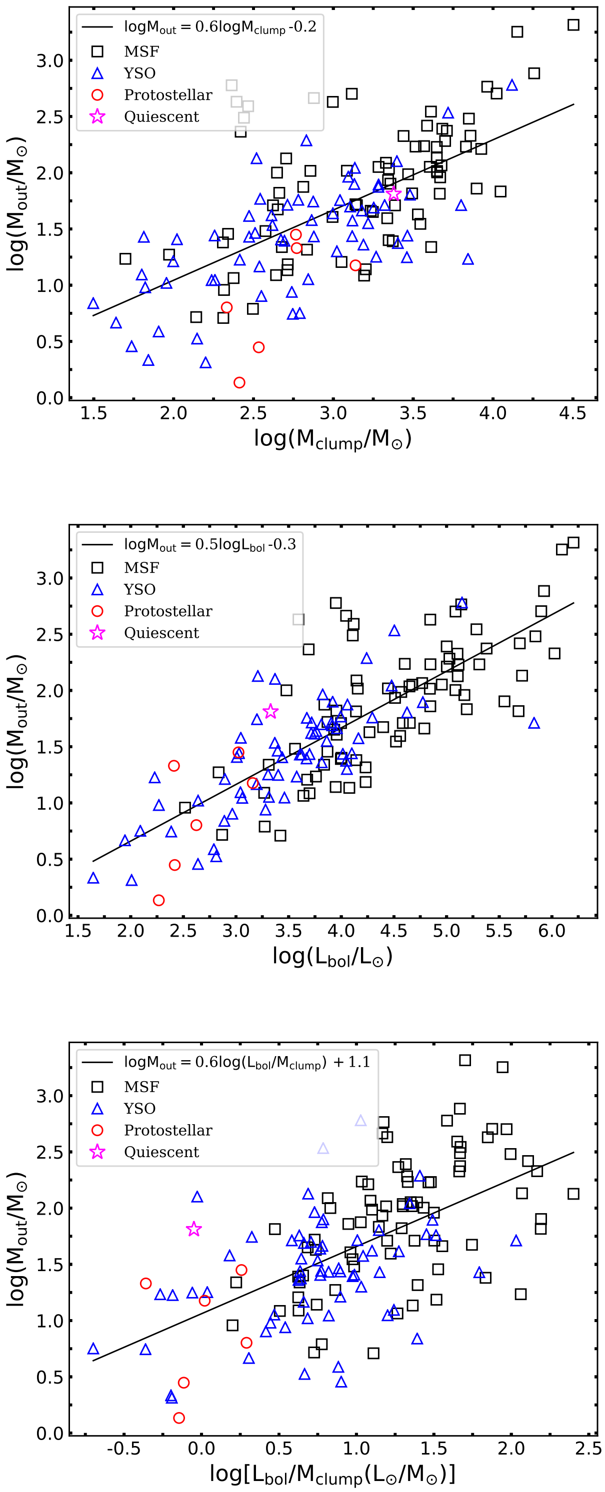

FIG. 6.— Top-panel: (a) outflow mass versus clump masses. Middle-panel: (b) outflow mass versus bolometric luminosity. Bottom-panel: (c) outflow mass versus luminosity-to-mass ratio. The black squares, blue triangles, red circles, and magenta stars refer to MSF, YSO, protostellar, and quiescent clumps. The solid line in each plot is the least square linear fit line in logarithmic scale.

that the two parameters are physically related. The fit to the logs of these parameters give a slope of 0.5 ± 0.03, which is similar to the slope reported by Wu et al. (2004) for a sample of high-mass and low-mass sources (0.56±0.02) spanning a wide range for L_{bol} between $10^{-1}\,L_\odot$ and $10^6\,L_\odot$. López-Sepulcre et al. (2009) also find a similar relation toward a sample of O-type young stellar objects. The agreement between all of these studies suggests that the correlation is applicable over a broad range of luminosities (i.e., $10^{-1}\,L_\odot \sim 10^{6.5}\,L_\odot$) from low-mass objects to massive objects, and that the outflow driving mechanism is likely to be similar for all luminosities.

In addition, the relation between M_{out} and L_{bol}/M_{clump} indicates that the outflow mass increases as the embedded protostar in the clump evolves. In Figure 6, the largest amount of entrainment mass comes from the most evolved MSF clumps. While there is no clear evolutionary trend of outflow mass for the four stages this is probably because the properties of the four proposed evolutionary stages are likely to overlap with each other (see König et al. (2017) and Urquhart et al. (2018)). The partial correlation coefficient, $\rho = 0.59$, is larger than found for the M_{out} and M_{clump} ($\rho = 0.35$), but smaller than found for M_{out} and L_{bol} ($\rho = 0.66$).

5.3.2. $\dot{M}_{out}$ *versus* M_{clump}, L_{bol} *and* L_{bol}/M_{clump}

We present the relationships that $\dot{M}_{out}$ as a function of M_{clump}, L_{bol}, and L_{bol}/M_{clump} in the upper, middle and lower panels of Figure 7 and present the correlation coefficients and results of linear fits to the data in Table 7. The tight correlation between outflow mass-loss rate and clump mass suggests that higher mass clumps host protostellar objects that have higher outflow activity, which agrees with previous results (de Villiers et al. 2014) within the uncertainties. Furthermore, it is possible to give a rough estimation for the average accretion rate ($\dot{M}_{accr}$) from the mean outflow mass-loss rate as $\dot{M}_{accr} \sim \dot{M}_{out}/6$, by following the same strategy as in Beuther et al. (2002) and de Villiers et al. (2014), which are based on star formation models (e.g., Shu et al. 1999; Tomisaka 1998). The mean outflow mass-loss rate is $\dot{M}_{out} = 9.2 \times 10^{-4}\,M_\odot\,yr^{-1}$ in our sample, the approximate mean accretion rate is $\dot{M}_{accr} \sim \dot{M}_{out}/6 \sim 1.5 \times 10^{-4}\,\mathrm{M_\odot\,yr^{-1}}$, which is the same order of magnitude as the $\sim 10^{-4}\,\mathrm{M_\odot\,yr^{-1}}$ found by previous studies of luminous YSOs and H II regions (e.g., Beuther et al. 2002; Zhang et al. 2005; Kim & Kurtz 2006; López-Sepulcre et al. 2009; de Villiers et al. 2014).

The correlation of mass entrainment rate ($\dot{M}_{out}$) and bolometric luminosity ($L_\odot$) has been discussed in a number of previous studies (Cabrit & Bertout 1992; Shepherd & Churchwell 1996a; Henning et al. 2000; Beuther et al. 2002; López-Sepulcre et al. 2009), all of which have reported a similar relation that higher luminosity objects are associated with higher outflow mass entrainment rates. From this relation, Shepherd & Churchwell (1996a) suggested that massive stars are responsible for the observed outflow power. Beuther et al. (2002) proposed that the mass entrainment rate does not depend strongly on the luminosity for sources $L_{bol} > 10^3\,L_\odot$. However, Henning et al. (2000) suggested that a correlation between the mass entrainment rate and luminosity for low-, intermediate- and high-luminosity objects. Our study confirms that a tight positive correlation exists between outflow mass-loss rates and luminosity for objects of all luminosities.

Furthermore, the entrainment rates ($\dot{M}_{out}$) are also related to the luminosity-to-mass ratio (L_{bol}/M_{clump}) of the clump,

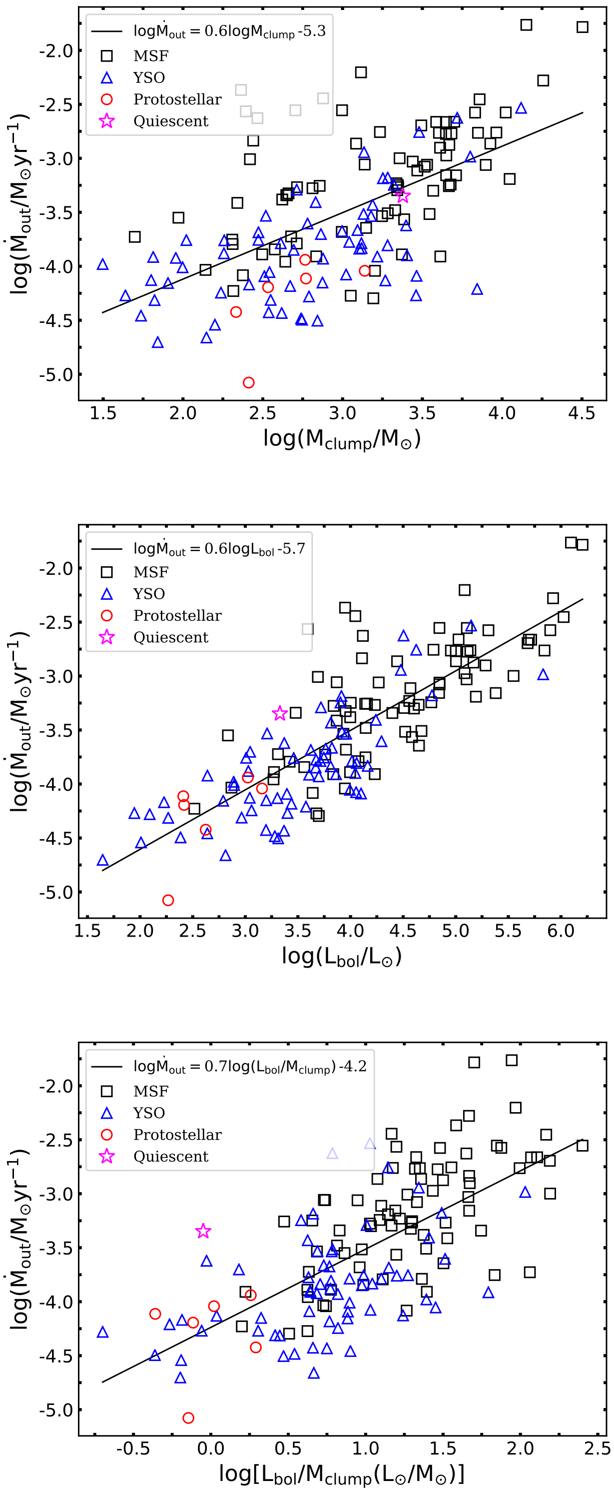

FIG. 7.— Top-panel: (a) outflow mass-loss rate versus clump masses. Middle-panel: (b) outflow mass-loss rate versus bolometric luminosity. Bottom-panel: (c) outflow mass-loss rate versus luminosity-to-mass ratio. The markers represent the same source type with Figure 6. The solid line in each plot is the least square linear fit line in logarithmic scale.

which suggests a higher entrainment rate is associated with more evolved protostars with larger values of L_{bol}/M_{clump}. This indicates that accretion rate increases with the evolution of star formation in the clump, providing strong support for theoretical models that predict accretion rates increase as a function of time (e.g., Bernasconi & Maeder 1996; Norberg & Maeder 2000; Behrend & Maeder 2001; Haemmerlé et al. 2013). The partial correlation coefficient $\rho = 0.68$ is larger than $\rho = 0.47$ for $\dot{M}_{out}$ and M_{clump}, but smaller than $\rho = 0.80$ for $\dot{M}_{out}$ and L_{bol}.

5.3.3. F_{CO} *versus* M_{clump}, L_{bol} *and* L_{bol}/M_{clump}

We present outflow mechanism force F_{CO} as a function of clump properties of M_{clump}, L_{bol}, and L_{bol}/M_{clump} in the upper, middle and lower panels of Figure 8 and the correlation coefficients and results of linear fits to the data in Table 7.

The mechanical force of an outflow (F_{CO}, also known as the outflow momentum flux) is the ratio of the momentum to the dynamical age of the outflow and can be used as a measure of the outflow strength and the rate at which momentum is injected into the clump by the outflow (Bachiller & Tafalla 1999; Downes & Cabrit 2007). Many central studies have reported that outflow force is positively correlated with clump (or core) mass and luminosity (e.g. Cabrit & Bertout 1992; Bontemps et al. 1996; Shepherd & Churchwell 1996a; Wu et al. 2004; Zhang et al. 2005). We find similar positive correlations in our sample in Figure 8.

Interestingly, we also find a positive correlation between the outflow force and the luminosity-to-mass ratio of the clump (see Figure 10 and 8), which suggests that as the star formation evolves within the clump the outflow force increases. In our sample (see figure 8), the most powerful outflows originate within the most evolved MSF clumps, whereas the first three evolutionary stages (e.g., quiescent, protostellar and YSO) are associated with less powerful outflows. This is in contradiction to studies of low mass star formation which show a decrease in the outflow force between Class 0 and I stages (Bontemps et al. 1996; Curtis et al. 2010c). We investigate this point in more detail in Section 5.3.5. The partial correlation coefficient $\rho = 0.65$ is larger than $\rho = 0.51$ for F_{CO} versus M_{clump}, but smaller than $\rho = 0.79$ for F_{CO} versus L_{bol}.

5.3.4. L_{CO} *versus* M_{clump}, L_{bol} *and* L_{bol}/M_{clump}

We present the relations between outflow mechanism luminosity L_{CO} and outflow properties of M_{clump}, L_{bol}, and L_{bol}/M_{clump} in the upper, middle and lower panels of Figure 9 and the correlation coefficients and results of linear fits to the data in Table 7. Tight relations exist between outflow mechanical luminosity L_{CO} and clump mass, bolometric luminosity L_{bol}, as well as luminosity-to-mass ratio L_{bol}/M_{clump}. The relation between L_{CO} and L_{bol} ($L_{CO} \propto L_{bol}^{0.8}$) is similar to the reported correlations of $L_{CO} \propto L_{bol}^{0.8}$ for embedded YSOs in Cabrit & Bertout (1992), and slightly larger than $L_{CO} \propto L_{bol}^{0.6}$ for both low-mass and high-mass groups in Wu et al. (2004). The average of value L_{CO}/L_{bol} is $\sim 3 \times 10^{-4}$.

Similarly to outflow force, the mechanical luminosity is also related to the luminosity-to-mass ratio of the clump, suggesting that clumps with more evolved star formation are associated with more powerful outflows. In Figure 9, the most luminous outflow comes from the most evolved MSF clumps, and the first three evolutionary stages (e.g., quiescent, protostellar and YSO) are associated with less luminous outflows. The partial

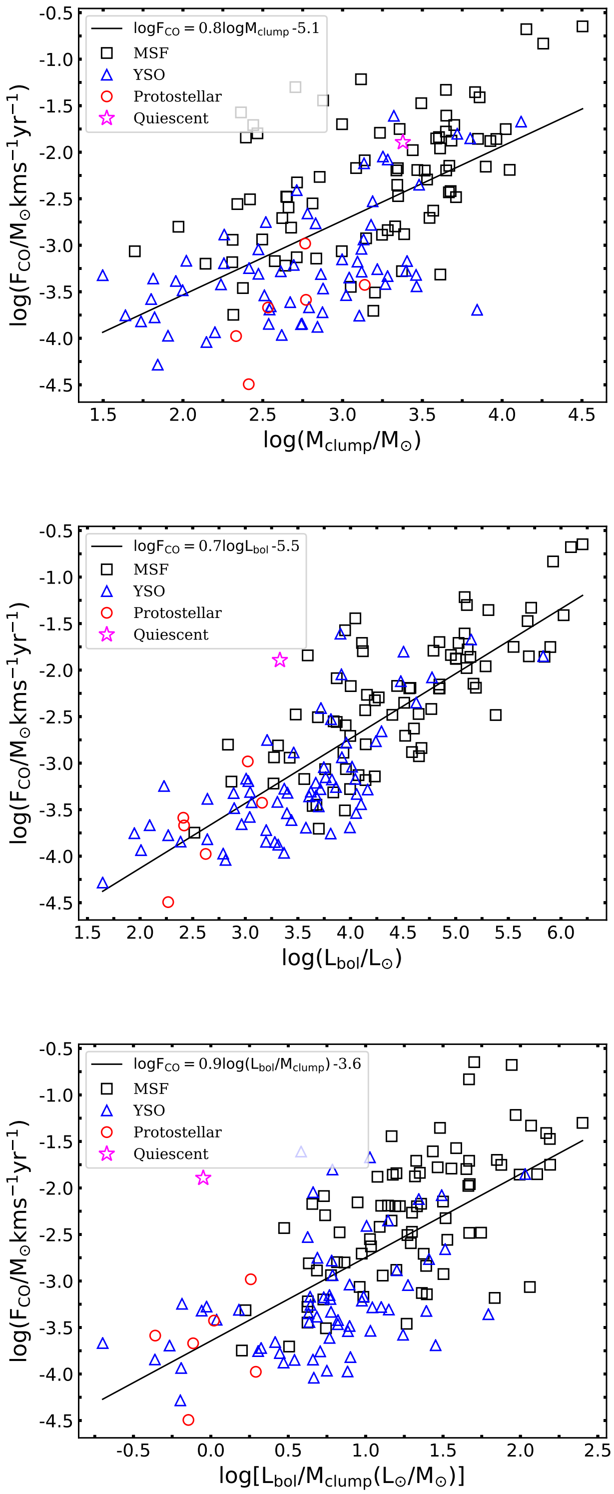

FIG. 8.— Top-panel: (a) outflow mechanical force versus clump masses. Middle-panel: (b) outflow mechanical force versus bolometric luminosity. Bottom-panel: (c) outflow mechanical force versus luminosity-to-mass ratio. The markers represent the same source types with Figure 6. The solid line in each plot is the least square linear fit line in logarithmic scale.

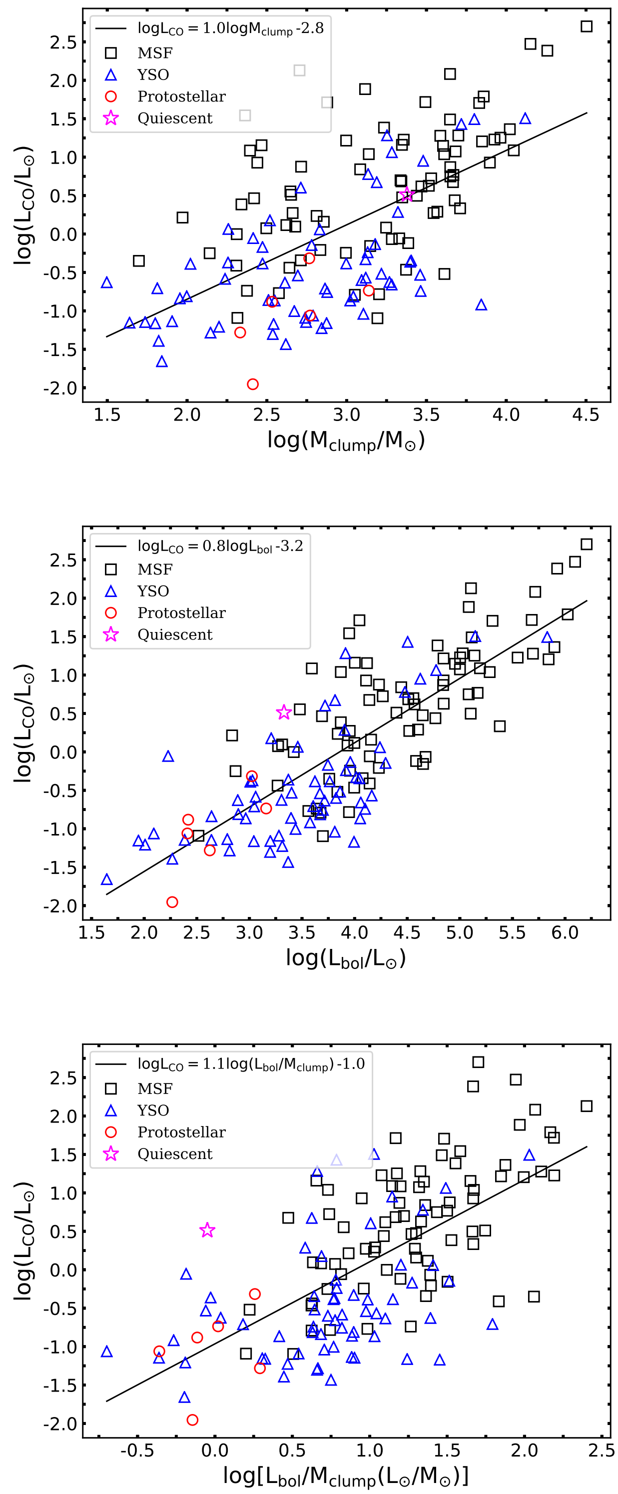

FIG. 9.— Top-panel: (a) outflow mechanical luminosity versus clump masses. Middle-panel: (b) outflow mechanical luminosity versus bolometric luminosity. Bottom-panel: (c) outflow mechanical luminosity versus luminosity-to-mass ratio. The markers represent the same source types as Figure 6. The solid line in each plot is the least square linear fit line in logarithmic scale.

correlation coefficient $\rho = 0.62$ is larger than $\rho = 0.54$ for L_{CO} and M_{clump}, but smaller than $\rho = 0.79$ for L_{CO} and L_{bol}. There is a close correlation between the clump luminosity and the mechanical luminosity.

5.3.5. *Implications of the clump-outflow correlations*

As suggested by McKee & Tan (2003), the accretion rate during star-formation is proportional to the surface density of the clumps $\Sigma^{0.75}$. This indicates that the most massive and dense clumps harbor stars with higher accretion rate than those forming in lower-mass clumps. Urquhart et al. (2013) found the bolometric luminosities of a sample of massive star forming clumps were tightly correlated with the Lyman continuum flux emitted from their embedded HII regions and therefore demonstrated that the vast majority of the observed luminosity could be directly attributed to the most massive stars in the clumps. Furthermore, Urquhart et al. (2013) also found a tight correlation between the clump mass and the mass of the most massive stars that showed that the most massive stars are preferentially found toward the centre of the most massive clumps in the highest column density regions. The correlations between outflow and clump properties in the above section suggest that higher clump masses, more luminous and evolved central sources are associated with much more powerful outflows, together with higher entrainment masses, larger entrainment mass rates, stronger outflow force, and higher outflow mechanical luminosity. Furthermore, the luminosity of the clumps shows the strongest relation with outflow properties as its correlation coefficient is the highest. This provides support that the outflow may be dominated by the most luminous and massive source within clumps, as the luminosity of the clump is in turn largely provided by that of the most massive protostar or YSO within the clump (Urquhart et al. 2013, 2014b). It is difficult to resolve the contributions from a single massive protostar or YSO in clumps (Urquhart et al. 2013), however, the tight relation between the most massive and luminous clumps associated with most powerful outflows from our investigation is statistically reliable.

The mean accretion rates $\sim 10^{-4}\,M_{\odot}\,yr^{-1}$ estimated by our sample are large enough to overcome the strong radiation from massive protostars, which supports the expected accretion rates in theoretical models of massive star formation (e.g., Bonnell et al. 2001; Krumholz et al. 2007).

We saw a positive correlation between outflow force and mechanical luminosity with clump luminosity and luminosity-to-mass ratio, which at first sight indicates that the outflows increase in force and luminosity as the star formation evolves. However, the slopes between outflow properties and clumps parameters are rather shallow (< 1) in log-log space (see Table 7), which suggests that the outflow properties evolve more slowly than do L_{bol}, M_{clump} and L_{bol}/M_{clump}. This may indicate a decrease in the mass accretion rate (and resulting mass outflow rate) whilst the luminosity of the central YSOs continues to increase. Alternatively this may be caused by a decrease in the amount of entrained material as the outflow cavities become more developed. Another possibility is that while larger clumps are associated with more massive and luminous sources and these drive more powerful outflows perhaps less of the total luminosity is emanating from the star driving the outflow. Finally, almost all of our outflow sample are comprised of mid-infrared bright clumps with $L_{bol}/M_{clump} \sim 10\,(L_{\odot}/M_{\odot})$, which indicates that they are all likely to be at a similar evolutionary stage close to the end of the main accretion phase (see Figure 24 in Urquhart et al. 2018) and which may explain the tight correlations between parameters.

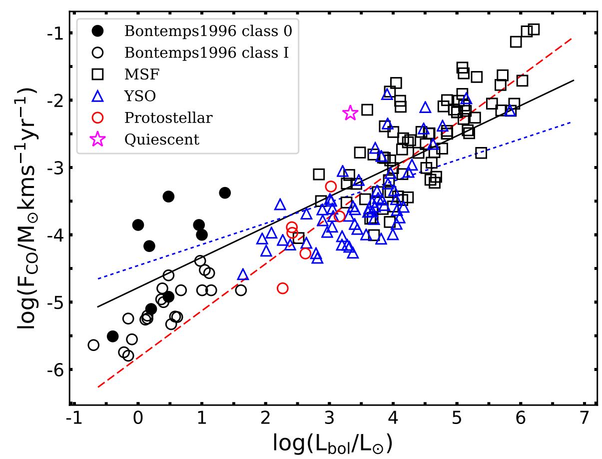

FIG. 10.— Outflow force $F_{CO} = \dot{P}$ versus the bolometric luminosity L_{bol} of central sources. The markers represent the same source types as Figure 6. To compare with low-mass outflow force, the filled and open circles respectively indicate the Class 0 and Class I from Bontemps et al. (1996). The black solid line ($\log F_{CO} = 0.5\log L_{bol} - 4.7$) represents the best fit in log-log space between F_{CO} and L_{bol} for both low- and high-mass outflows. The red dashed line ($\log F_{CO} = 0.7\log L_{bol} - 5.5$) is the best fit for all massive outflows in this study, and extrapolated to lower luminosities. The blue dotted line ($\log F_{CO} = 0.3\log L_{bol} - 4.5$) indicates the best fit for low-mass outflows from Bontemps et al. (1996), extended to higher luminosities.

5.4. *Comparison with Low-mass outflows*

The results of our least-squares fitting between outflow parameters and clump properties in this work are consistent with the relations seen in low-mass outflows (Cabrit & Bertout 1992; Wu et al. 2004). Here we present a comparison between the outflow force for low luminosities and high luminosities to illustrate their connection.

Figure 10 plots the outflow force F_{CO} against luminosity for Massive Star-Forming (MSF), YSOs, protostellar, and quiescent clumps in the sample of 153 mapped outflows, together with outflows associated with Class 0 and Class I protostars/YSOs from Bontemps et al. (1996). The outflow mechanical force values have been inclination-corrected using an average angle of 57°.3 for this work and this has also been applied to the results of Bontemps et al. (1996). In Figure 10 we see a continuous relationship between outflow force and luminosity that holds over 7 orders of magnitude. This supports the hypothesis that a similar outflow mechanism may operate for both low-mass and high-mass star formation. However when low luminosity and high luminosity sources are fitted separately we find a slight difference between low and high luminosity samples, which implies that the existence of a common outflow mechanism is not as clear cut as Figure 10 suggests. This small difference has been also found by Maud et al. (2015). Nevertheless we (and Maud et al. 2015) cannot exclude the possibility of systematic error between the outflow force of low luminosity and high luminosity samples given that they lie at very different distances and were observed using different techniques. The main cause of the different slope in the outflow force-luminosity relation are the Class 0 sources observed by Bontemps et al. (1996). A larger and more consistently analysed sample of low luminosity sources, perhaps from the JCMT Gould Belt survey (Ward-Thompson

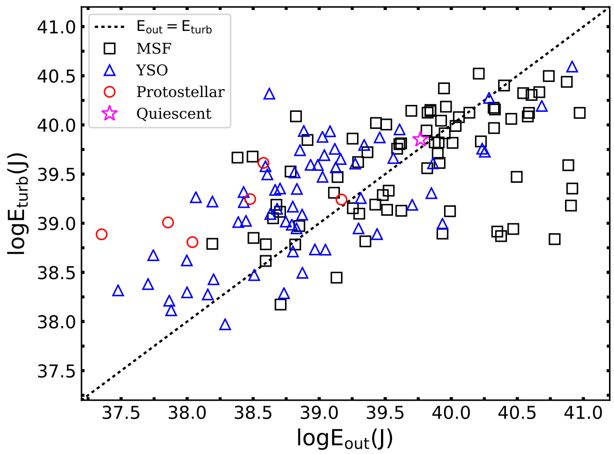

FIG. 11.— Outflow energy of the 153 outflow clumps against turbulence energy. The markers represent the same source types as Figure 6 and the dotted line show $E_{out} = E_{turb}$. This may indicates that outflow energy is comparable to turbulence energy for the majority clump.

et al. 2007), is required to investigate any potential systematic bias. However, this work lies beyond the scope of our study.

In conclusion, we find that outflows are ubiquitous phenomena for both high-mass and low-mass groups with a potentially similar driving mechanism.

5.5. *The evolution of the outflows and clump turbulence*

Outflow feedback can help address two main questions: (a) do outflows inject enough momentum to maintain turbulence; (b) can outflows propriety couple to clump gas to drive turbulent motions (Frank et al. 2014). It remains a challenge to quantify the cumulative impact of the outflow-driven turbulence on molecular clouds. One method to measure the effect that outflows have on their parent clumps is to compare the total outflow energy and the turbulent kinematic energy. The turbulent kinematic energy can be estimated by $E_{turb} = (3/16\ln 2)M_{core} \times FWHM^2$ (Arce & Goodman 2001), if the thermal motions are a negligible contribution to the full width half maximum (FWHM) of $C^{18}O$ J = 3 − 2 (Arce & Goodman 2001; Maud et al. 2015). Our large sample of clumps and outflows with well determined physical properties allows us to statistically investigate the correlation between outflow energy and turbulence energy at different evolutionary stages of central sources, and examine the impact that outflows have on their natal clumps.

In Figure 11, we see that the outflow energy (E_{out}) appears to be comparable to the turbulent energy (E_{turb}) for the 153 clumps with mapped outflows in our sample. The mean value of $E_{out}/E_{turb} \sim 3.3$, with a spread of 0.02 ∼ 88. This suggests that the outflows associated with most clumps have enough energy to maintain turbulence. Cunningham et al. (2009) proposed that jet-driven outflows can provide an efficient form of dynamical feedback and act to maintain turbulence in the molecular cloud. However, some authors suggested that outflows have enough power to drive turbulence in the local environment (e.g., Arce et al. 2010; Mottram & Brunt 2012; Maud et al. 2015), but do not contribute significantly to the turbulence of the clouds (e.g., Arce et al. 2010; Maud et al. 2015; Plunkett et al. 2015).

Looking at each subgroup in more details in Figure 11, we can see that all clumps in the first two evolutionary stages (i.e., quiescent, protostellar) lie above the line of equality of E_{turb} and E_{out} (i.e., $E_{turb} > E_{out}$). This is consistent with Graves et al. (2010), who found the total outflow energy to be smaller than the turbulent kinetic energy of the cloud. For the three more evolved stages, the mean turbulence kinematic energy is consistent with each other within the uncertainties, i.e., protostellar clumps ($E_{turb} \sim 1.4 \times 10^{39}$ J), YSO clumps ($E_{turb} \sim 3.9 \times 10^{39}$ J), MSF clumps ($E_{turb} \sim 9.8 \times 10^{39}$ J). While the mean outflow energy increase as the clump evolves, i.e., protostellar clumps ($E_{out} \sim 3.9 \times 10^{38}$ J), YSO clumps ($E_{out} \sim 4.0 \times 10^{39}$ J), MSF clumps ($E_{out} \sim 3.5 \times 10^{40}$ J). Thus, the mean ratio of E_{out}/E_{turb} increase from ∼ 0.3 to ∼ 1 and then to ∼ 3.6 as the clump evolves from the protostellar to MSF stage. This may imply that no matter whether the outflows have not (e.g., protostellar stage) or have (e.g., YSO or MSF phase) enough energy to fully drive the turbulence, outflow energy does not significantly contribute to the turbulence energy of the parent clump as the protostar evolves. This is consistent with simulation preformed by Krumholz et al. (2012) that showed that outflow-driven feedback has a smaller impact on massive star formation regions.

In the left panel of Figure 12 we show the turbulent energy (E_{turb}) versus the luminosity-to-mass ratio of the clump (L_{bol}/M_{clump}) for the 314 clumps in our sample with measured clump properties and $C^{18}O$ detections. The average value of E_{turb} is $\sim 7.0 \times 10^{39}$ J for clumps that show outflows, which is consistent to the value of $\sim 6.8 \times 10^{39}$ J for clumps that do not contain outflows, within uncertainties. In addition, there is no difference for the range of turbulent energy values between clumps with outflows and clumps without outflows, which implies star-forming clumps have a similar level of turbulence as quiescent clumps. This is consistent with studies mentioned in Hennebelle & Falgarone (2012) for clouds with and without star-forming activity, showing similar velocity dispersion (Kawamura et al. 2009) and presenting comparable levels of turbulence (Williams et al. 1994). Furthermore, it is clear that there is no obvious correlation between the E_{turb} and L_{bol}/M_{clump}, with Spearman rank coefficient $\rho = 0.08$ and p-value=0.33, which suggests that the level of turbulence in the clump is not significantly affected by the evolution of the central object. This is consistent with the analysis of NH_3 line-widths of ∼ 8000 dense clumps as a function of evolution of embedded protostars (L_{bol}/M_{clump}) in Urquhart et al. (2018). In addition, the right panel of Figure 12 shows that the outflow energy is strongly correlated with the evolution of central objects, with Spearman rank coefficient $\rho = 0.6$ and p-value$\ll 0.001$, indicating higher outflow energies are associated with more evolved objects (i.e., larger value of L_{bol}/M_{clump}).

All these findings imply that the outflow energy from embedded protostars should increase as they evolve, in addition, this outflow energy is large enough to maintain the turbulence in the clump (see Figure 11). However, outflow energy does not significantly contribute to the energy of the turbulence in the clump as the protostar evolves (see left panel of Figure 12). The level of turbulence is similar for clumps associated with outflows and not associated with outflows at four evolutionary stages, which suggests that the origin of the turbulence occurs before the star formation begins. This is consistent with several other studies (e.g., Ossenkopf & Mac Low 2002; Brunt et al. 2009; Padoan et al. 2009), who suggest turbulence is mostly driven by large-scale mechanisms that originate outside the

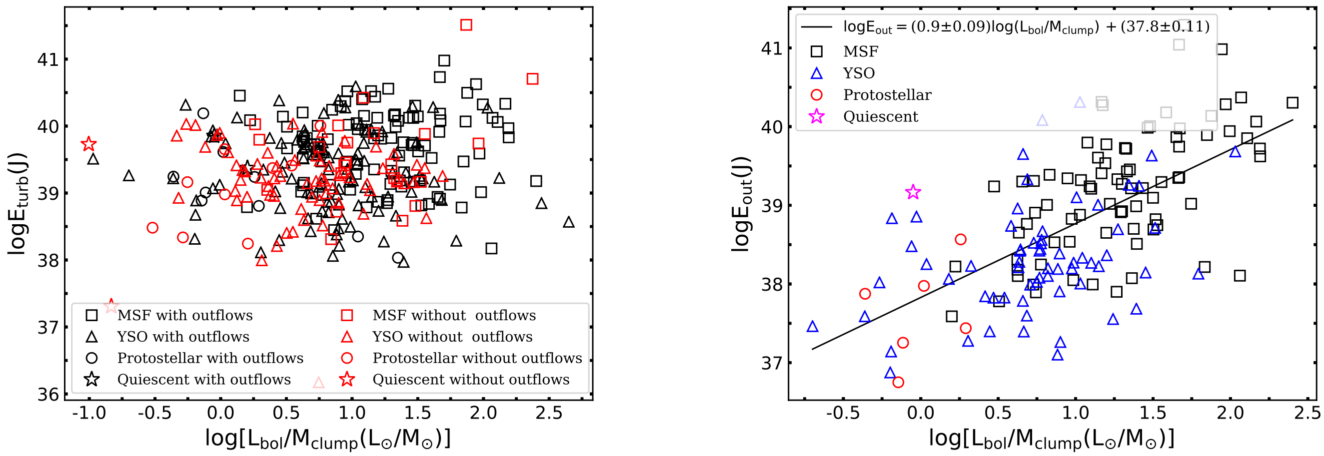

FIG. 12.— Left-panel: outflow energy of the 314 clumps against the luminosity-to-mass ratio of central objects. These markers refer to the same source type with Figure 6, with all black markers representing clumps with detected outflows and all red markers indicating clumps with no outflows. It is shown that clumps without outflows appear to have the range of turbulence energy similar to the clumps with no outflows. More interestingly, the level of turbulence is not significantly affected by the evolution of central sources in the clumps. Right panel: the plot of outflow energy (E_{out}) versus the luminosity-to-mass ratio of central source for the 153 clumps with mapped outflows,. This suggests that higher outflow energies are associated with more evolved objects (i.e., larger value of L_{bol}/M_{clump}).

cloud (e.g. supernovae).

6. SUMMARY AND CONCLUSIONS

We have carried out a unbiased outflow survey toward 919 ATLASGAL clumps located in the CHIMPS survey, 325 of which have ^{13}CO and C^{18}O data that are suitable for outflow identification. The physical properties of the 325 clumps are shown in Table 2. We detect high velocity outflow wings towards 225 clumps by inspecting the line wings in the one dimensional ^{13}CO spectra extracted at the centroid of each clump (see Table 3 for details). We investigate these wings further by mapping the ^{13}CO integrated intensity corresponding to each wing. We are able to estimate the outflow properties for 153 clumps that are found to have well-defined bipolar outflows and reliable distances. These properties are given in Table 4. The overall physical properties of the clumps are summarized in Table 6. We show that the outflows discovered here are more than 2 orders of magnitude more massive and energetic than outflows associated with low-mass objects. We compare outflow properties with clump characteristics, discuss how the properties of this large homogenous sample change as a function of evolution and examine their impact on the turbulence of their natal clumps.

The main results are summarized as follows:

1. 225 of the 325 massive clumps show high velocity line wings indicative of outflows, implying a $69 \pm 3\%$ detection frequency of CO outflows. Among the 225 sources, 10 clumps have single blue/red wing and the rest 215 show both blue and red wings. The detection frequency bipolar outflows is $66 \pm 3\%$, while we find significantly higher outflow detection rates in UC H II regions (52/56, $93 \pm 3\%$), maser associated sources (60/70, $86 \pm 4\%$), and HC H II regions (4/4, 100%) in our sample.

2. The 225 clumps with detected outflows have significantly higher M_{clump}, L_{bol}, L_{bol}/M_{clump} and higher N_{H_2} compared to 100 clumps with no outflows. K-S tests for these parameters suggest that the two samples are from different populations.

3. The detection rate of outflows increase with increasing of M_{clump}, L_{bol}, L_{bol}/M_{clump} and N_{H_2}, which can be as high as 90% when $M_{clump} > 3.9 \times 10^3$ M$_\odot$, $L_{bol} > 2.7 \times 10^4$ L$_\odot$, $L_{bol}/M_{clump} > 10$ (L$_\odot$/M$_\odot$), $N_{H_2} > 3.8 \times 10^{22}$ cm^{-2}. The detection rates as a function of N_{H_2}, are entirely consistent with the gas surface threshold density for efficient star formation suggested by Lada et al. (2010) and Heiderman et al. (2010).

4. Outflow activity begins to switch on at the youngest quiescent stage (i.e., 70μm weak) in this young sample. The detection frequency of outflow is increasing as the clumps evolve from quiescent ($50 \pm 25\%$), to protostellar ($53 \pm 11\%$), to YSO ($61 \pm 4\%$), and then to MSF clump ($82 \pm 2\%$). The detection of outflow activity appears to peak (i.e., 100%) at pre-UC HII (e.g., HC HII regions, water and/or methanol masers) or early UC HII region phase (e.g., maser associated UC HII regions).

5. Outflow properties (M_{out}, $\dot{M}_{out}$, F_{CO} and L_{CO}) are tightly correlated with M_{clump}, L_{bol} and L_{bol}/M_{clump} of the clump when the effect of distance is controlled. The strongest relation between the outflow parameters and the clump luminosity may indicate that outflows are dominated by the energy of most luminous source in the clump. These correlations are consistent with studies of both low-mass and high-mass samples which leads us to conclude that they share a similar mechanism for outflows, although there exists the potential for systematic bias between low and high mass samples.

6. The mean outflow mass entrainment rate is 9.2×10^{-4} M$_\odot$ yr^{-1}, suggesting a mean accretion rate of $\sim 10^{-4}$ M$_\odot$ yr^{-1}. This is the same order found in high-mass star formation regions (e.g., Beuther et al. 2002; Kim & Kurtz 2006; de Villiers et al. 2014), and is in agreement with the accretion rates predicted theoretical models of massive star formation (e.g., Bonnell et al. 2001; Krumholz et al. 2007). Moreover, our results

are also consistent with an increasing accretion rate as a function of time, which is an expected consequence of number of theoretical models (e.g., Bernasconi & Maeder 1996; Norberg & Maeder 2000; Behrend & Maeder 2001; Haemmerlé et al. 2013).

7. The outflow energy is comparable to the turbulent energy of the cloud with mean $E_{out}/E_{turb} \sim 3.3$. While the outflow energy increases with increasing of L_{bol}/M_{clump}, i.e., with the evolution of the central protostar, the turbulent energy does not. We find no obvious correlation between E_{turb} and L_{bol}/M_{clump}. Thus the outflow does not contribute significantly to clump turbulence as the clump evolves. This suggests that core turbulence might exist before star formation begin, which is consistent with that turbulence is mostly driven by large-scale mechanisms (e.g., Ossenkopf & Mac Low 2002; Brunt et al. 2009; Padoan et al. 2009).

These results may suggest that outflow energies are dominated by the most massive and luminous protostars in the clumps. However, it is a challenge to resolve the contributions from single massive protostar in clumps. High angular resolution observations are needed to resolve individual outflows within the clumps. The large and homogeneously selected sample that we present here should form the basis for subsequent interferometric observations with ALMA and NOEMA.

In addition, we have demonstrated the potential of wide-field Galactic Plane surveys to discover a relatively unbiased selection of outflows. We look forward to the expansion of our study using the forthcoming CHIMPS2 survey which will expand the area covered by CHIMPS to the remaining section of the first Galactic quadrant and potentially double the number of outflows discovered here.

ACKNOWLEDGEMENTS

We would like to thank the anonymous referee for the helpful comments. We acknowledge support from the NSFC (11603039, 11473038) from China's Ministry of Science and Technology. M. A. T. acknowledges support from the UK Science & Technology Facilities Council via grant ST/M001008/1. A. Y. Y. would like to thank the Science and UK Technology Facilities Council and the China Scholarship Council for grant funding through the China-UK SKA joint PhD programme.

This document was produced using the Overleaf web application, which can be found at www.overleaf.com.

REFERENCES

Andre, P., Ward-Thompson, D., & Barsony, M. 1993, ApJ, 406, 122
Arce, H. G., Borkin, M. A., Goodman, A. A., Pineda, J. E., & Halle, M. W. 2010, ApJ, 715, 1170
Arce, H. G., & Goodman, A. A. 2001, ApJ, 554, 132
Arce, H. G., Shepherd, D., Gueth, F., et al. 2007, Protostars and Planets V, 245
Astropy Collaboration, Robitaille, T. P., Tollerud, E. J., et al. 2013, A&A, 558, A33
Bachiller, R. 1996, ARA&A, 34, 111
Bachiller, R., & Gomez-Gonzalez, J. 1992, A&A Rev., 3, 257
Bachiller, R., & Tafalla, M. 1999, in NATO Advanced Science Institutes (ASI) Series C, Vol. 540, NATO Advanced Science Institutes (ASI) Series C, ed. C. J. Lada & N. D. Kylafis, 227
Bally, J. 2016, ARA&A, 54, 491
Behrend, R., & Maeder, A. 2001, A&A, 373, 190
Bernasconi, P. A., & Maeder, A. 1996, A&A, 307, 829
Beuther, H., Schilke, P., Sridharan, T. K., et al. 2002, A&A, 383, 892
Bjerkeli, P., Liseau, R., Nisini, B., et al. 2013, A&A, 552, L8
Bonnell, I. A., Bate, M. R., Clarke, C. J., & Pringle, J. E. 2001, MNRAS, 323, 785
Bontemps, S., Andre, P., Terebey, S., & Cabrit, S. 1996, A&A, 311, 858
Brunt, C. M., Heyer, M. H., & Mac Low, M.-M. 2009, A&A, 504, 883
Cabrit, S., & Bertout, C. 1990, ApJ, 348, 530
—. 1992, A&A, 261, 274
Caswell, J. L. 2013, in IAU Symposium, Vol. 292, Molecular Gas, Dust, and Star Formation in Galaxies, ed. T. Wong & J. Ott, 79–82
Churchwell, E. 2002, ARA&A, 40, 27
Codella, C., Lorenzani, A., Gallego, A. T., Cesaroni, R., & Moscadelli, L. 2004, A&A, 417, 615
Contreras, Y., Schuller, F., Urquhart, J. S., et al. 2013, A&A, 549, A45
Cunningham, A. J., Frank, A., Carroll, J., Blackman, E. G., & Quillen, A. C. 2009, ApJ, 692, 816
Curtis, E. I., Richer, J. S., & Buckle, J. V. 2010a, MNRAS, 401, 455
Curtis, E. I., Richer, J. S., Swift, J. J., & Williams, J. P. 2010b, MNRAS, 408, 1516
—. 2010c, MNRAS, 408, 1516
de Villiers, H. M., Chrysostomou, A., Thompson, M. A., et al. 2014, MNRAS, 444, 566
—. 2015, MNRAS, 449, 119
Downes, T. P., & Cabrit, S. 2007, A&A, 471, 873
Evans, II, N. J., Balkum, S., Levreault, R. M., Hartmann, L., & Kenyon, S. 1994, ApJ, 424, 793
Feng, S., Beuther, H., Zhang, Q., et al. 2016, ApJ, 828, 100
Frank, A., Ray, T. P., Cabrit, S., et al. 2014, Protostars and Planets VI, 451
Frerking, M. A., Langer, W. D., & Wilson, R. W. 1982, ApJ, 262, 590
Graves, S. F., Richer, J. S., Buckle, J. V., et al. 2010, MNRAS, 409, 1412
Haemmerlé, L., Eggenberger, P., Meynet, G., Maeder, A., & Charbonnel, C. 2013, A&A, 557, A112
Hatchell, J., Fuller, G. A., & Richer, J. S. 2007, A&A, 472, 187
Heiderman, A., Evans, II, N. J., Allen, L. E., Huard, T., & Heyer, M. 2010, ApJ, 723, 1019
Helfand, D. J., Becker, R. H., White, R. L., Fallon, A., & Tuttle, S. 2006, AJ, 131, 2525
Hennebelle, P., & Falgarone, E. 2012, A&A Rev., 20, 55
Henning, T., Schreyer, K., Launhardt, R., & Burkert, A. 2000, A&A, 353, 211
Kawamura, A., Mizuno, Y., Minamidani, T., et al. 2009, ApJS, 184, 1
Keto, E., Zhang, Q., & Kurtz, S. 2008, ApJ, 672, 423
Kim, K.-T., & Kurtz, S. E. 2006, ApJ, 643, 978
Kim, S.-H., & Yi, S. V. 2006, Molecular Biology and Evolution, 23, 1068
König, C., Urquhart, J. S., Csengeri, T., et al. 2017, A&A, 599, A139
Königl, A., Romanova, M. M., & Lovelace, R. V. E. 2011, MNRAS, 416, 757
Krumholz, M. R., Klein, R. I., & McKee, C. F. 2007, ApJ, 656, 959
—. 2012, ApJ, 754, 71
Kurtz, S. 2005, in IAU Symposium, Vol. 227, Massive Star Birth: A Crossroads of Astrophysics, ed. R. Cesaroni, M. Felli, E. Churchwell, & M. Walmsley, 111–119
Kurtz, S., Cesaroni, R., Churchwell, E., Hofner, P., & Walmsley, C. M. 2000, Protostars and Planets IV, 299
Kwan, J., & Scoville, N. 1976, ApJ, 210, L39
Lada, C. J. 1985, ARA&A, 23, 267
Lada, C. J., Lombardi, M., & Alves, J. F. 2010, ApJ, 724, 687
Lada, C. J., & Wilking, B. A. 1984, ApJ, 287, 610
López-Sepulcre, A., Codella, C., Cesaroni, R., Marcelino, N., & Walmsley, C. M. 2009, A&A, 499, 811
Maud, L. T., Moore, T. J. T., Lumsden, S. L., et al. 2015, MNRAS, 453, 645
McKee, C. F., & Tan, J. C. 2003, ApJ, 585, 850
Minchin, N. R., White, G. J., & Padman, R. 1993, A&A, 277, 595
Molinari, S., Testi, L., Rodríguez, L. F., & Zhang, Q. 2002, ApJ, 570, 758
Mottram, J. C., & Brunt, C. M. 2012, MNRAS, 420, 10
Norberg, P., & Maeder, A. 2000, A&A, 359, 1025
Ossenkopf, V., & Mac Low, M.-M. 2002, A&A, 390, 307
Padoan, P., Juvela, M., Kritsuk, A., & Norman, M. L. 2009, ApJ, 707, L153
Plunkett, A. L., Arce, H. G., Corder, S. A., et al. 2015, ApJ, 803, 22
Qin, S.-L., Wang, J.-J., Zhao, G., Miller, M., & Zhao, J.-H. 2008, A&A, 484, 361
Richer, J. S., Shepherd, D. S., Cabrit, S., Bachiller, R., & Churchwell, E. 2000, Protostars and Planets IV, 867
Rigby, A. J., Moore, T. J. T., Plume, R., et al. 2016, MNRAS, 456, 2885
Sánchez-Monge, Á., López-Sepulcre, A., Cesaroni, R., et al. 2013, A&A, 557, A94
Schuller, F., Menten, K. M., Contreras, Y., et al. 2009, A&A, 504, 415
Sewilo, M., Churchwell, E., Kurtz, S., Goss, W. M., & Hofner, P. 2004, ApJ, 605, 285
Sewiło, M., Churchwell, E., Kurtz, S., Goss, W. M., & Hofner, P. 2011, ApJS, 194, 44
Shepherd, D. S., & Churchwell, E. 1996a, ApJ, 472, 225
—. 1996b, ApJ, 457, 267
Shu, F. H., Adams, F. C., & Lizano, S. 1987, ARA&A, 25, 23
Shu, F. H., Allen, A., Shang, H., Ostriker, E. C., & Li, Z.-Y. 1999, in NATO Advanced Science Institutes (ASI) Series C, Vol. 540, NATO Advanced Science Institutes (ASI) Series C, ed. C. J. Lada & N. D. Kylafis, 193
Snell, R. L., Loren, R. B., & Plambeck, R. L. 1980, ApJ, 239, L17

Tan, J. C., Beltrán, M. T., Caselli, P., et al. 2014, Protostars and Planets VI, 149
Tan, J. C., Kong, S., Zhang, Y., et al. 2016, ApJ, 821, L3
Thompson, M. A., Hatchell, J., Walsh, A. J., MacDonald, G. H., & Millar, T. J. 2006, A&A, 453, 1003
Tomisaka, K. 1998, ApJ, 502, L163
Traficante, A., Fuller, G. A., Billot, N., et al. 2017, MNRAS, 470, 3882
Urquhart, J. S., Morgan, L. K., Figura, C. C., et al. 2011, MNRAS, 418, 1689
Urquhart, J. S., Thompson, M. A., Moore, T. J. T., et al. 2013, MNRAS, 435, 400
Urquhart, J. S., Csengeri, T., Wyrowski, F., et al. 2014a, A&A, 568, A41
Urquhart, J. S., Moore, T. J. T., Csengeri, T., et al. 2014b, MNRAS, 443, 1555
Urquhart, J. S., Moore, T. J. T., Menten, K. M., et al. 2015, MNRAS, 446, 3461
Urquhart, J. S., König, C., Giannetti, A., et al. 2018, MNRAS, 473, 1059
van der Marel, N., Kristensen, L. E., Visser, R., et al. 2013, A&A, 556, A76
van der Walt, D. J., Sobolev, A. M., & Butner, H. 2007, A&A, 464, 1015
Ward-Thompson, D., Di Francesco, J., Hatchell, J., et al. 2007, PASP, 119, 855
Williams, J. P., de Geus, E. J., & Blitz, L. 1994, ApJ, 428, 693
Wilson, T. L., & Rood, R. 1994, ARA&A, 32, 191
Wu, Y., Wei, Y., Zhao, M., et al. 2004, A&A, 426, 503
Wu, Y., Yang, C., Li, Y., et al. 1999, Science in China A: Mathematics, 42, 732
Yorke, H. W., & Sonnhalter, C. 2002, ApJ, 569, 846
Zhang, C.-P., Wang, J.-J., Xu, J.-L., Wyrowski, F., & Menten, K. M. 2014, ApJ, 784, 107
Zhang, Q., Hunter, T. R., Brand, J., et al. 2005, ApJ, 625, 864
—. 2001, ApJ, 552, L167
Zinnecker, H., & Yorke, H. W. 2007, ARA&A, 45, 481
Zuckerman, B., Kuiper, T. B. H., & Rodriguez Kuiper, E. N. 1976, ApJ, 209, L137

APPENDIX

TABLES

TABLE 8
Clump properties of all 325 ATLASGAL clumps to search for outflows: clumps Galactic name and coordinates, integrated flux density at 870μm (F_{int}), heliocentric distance (Dist.), peak H_2 column density (N_{H_2}), bolometric luminosity (L_{bol}), and clump mass (M_{clump}). These physical values are from (Urquhart et al. 2018).

ATLASGAL CSC Gname	ℓ (°)	b (°)	F_{int} (Jy)	Dist. (kpc)	N_{H_2} (cm^{-2})	$logL_{bol}$ ($logL_\odot$)	$logM_{clump}$ ($logM_\odot$)	ATLASGAL CSC Gname	ℓ (°)	b (°)	F_{int} (Jy)	Dist. (kpc)	$logN_{H_2}$ (cm^{-2})	$logL_{bol}$ ($L_\odot$)	$logM_{clump}$ ($M_\odot$)
G027.784+00.057	27.784	0.057	9.11	5.9	22.578	3.9	3.2	G031.281+00.062	31.281	0.062	40.97	5.2	23.105	4.8	3.6
G027.796−00.277	27.796	−0.277	4.48	2.9	22.36	3.1	2.2	G031.386−00.269	31.386	−0.269	5.57	5.2	22.046	4.2	2.7
G027.883+00.204	27.883	0.204	9.16	8.3	22.19	3.3	3.6	G031.394+00.306	31.394	0.306	25.56	5.2	22.512	4.3	3.5
G027.903−00.012	27.903	−0.012	8.36	6.1	22.437	4.2	3.1	G031.396−00.257	31.396	−0.257	12.95	5.2	22.865	4.8	3.0
G027.919−00.031	27.919	−0.031	2.11	3.0	21.866	3.0	1.8	G031.412+00.307	31.412	0.307	61.68	5.2	23.696	4.8	3.9
G027.923+00.196	27.923	0.196	7.02	8.3	22.125	3.4	3.4	G031.498+00.177	31.498	0.177	1.89	5.2	22.259	2.9	2.5
G027.936+00.206	27.936	0.206	7.48	2.7	22.416	3.4	2.3	G031.542−00.039	31.542	−0.039	2.03	2.1	22.211	1.6	1.8
G027.978+00.077	27.978	0.077	9.49	4.5	22.381	4.2	2.8	G031.568+00.092	31.568	0.092	2.88	5.2	22.299	2.4	2.8
G028.013+00.342	28.013	0.342	1.76	8.3	21.872	3.5	2.7	G031.581+00.077	31.581	0.077	12.6	5.2	22.894	4.4	3.1
G028.033−00.064	28.033	−0.064	1.98	6.1	22.133	3.0	2.6	G031.594−00.192	31.594	−0.192	3.46	2.1	22.22	2.7	1.8
G028.144+00.321	28.144	0.321	5.76	–	22.276	–	–	G031.596−00.336	31.596	−0.336	1.38	5.2	22.026	2.8	2.3
G028.148−00.004	28.148	−0.004	9.19	6.1	22.628	3.9	3.2	G031.644−00.266	31.644	−0.266	1.66	2.1	22.169	1.9	1.6
G028.151+00.171	28.151	0.171	4.56	4.8	22.313	3.3	2.7	G031.668+00.241	31.668	0.241	2.33	5.2	22.267	3.3	2.5
G028.199−00.049	28.199	−0.049	35.49	6.1	23.169	5.1	3.6	G031.676+00.244	31.676	0.244	2.02	5.2	22.222	3.2	2.5
G028.231+00.041	28.231	0.041	19.78	6.1	–	–	–	G031.734−00.182	31.734	−0.182	1.54	5.2	21.993	2.9	2.3
G028.233+00.002	28.233	0.002	3.07	6.1	22.143	3.2	2.7	G032.019+00.064	32.019	0.064	19.64	5.2	22.942	3.8	3.7
G028.234+00.062	28.234	0.062	5.33	6.1	22.398	3.2	3.1	G032.044+00.059	32.044	0.059	41.74	5.2	23.151	4.6	3.8
G028.244+00.012	28.244	0.012	12.11	6.1	22.175	4.7	3.1	G032.051−00.089	32.051	−0.089	1.64	9.9	21.95	3.7	2.8
G028.288−00.362	28.288	−0.362	25.73	11.6	22.577	5.9	4.0	G032.117+00.091	32.117	0.091	14.15	5.2	22.556	4.5	3.1
G028.291+00.007	28.291	0.007	4.4	3.0	22.3	3.3	2.2	G032.149+00.134	32.149	0.134	25.01	5.2	22.893	4.6	3.5
G028.294−00.192	28.294	−0.192	1.37	10.4	21.981	3.5	2.9	G032.424+00.081	32.424	0.081	6.27	11.2	22.203	4.1	3.6
G028.301−00.382	28.301	−0.382	17.05	9.7	22.357	5.4	3.7	G032.456+00.387	32.456	0.387	1.99	3.0	22.267	2.6	2.0
G028.316−00.032	28.316	−0.032	10.62	6.1	22.288	3.0	3.4	G032.471+00.204	32.471	0.204	9.87	3.0	22.524	3.5	2.6
G028.321−00.009	28.321	−0.009	12.7	6.1	22.617	4.0	3.4	G032.604−00.256	32.604	−0.256	3.14	5.2	21.995	3.4	2.5
G028.388+00.451	28.388	0.451	1.52	4.6	21.896	3.1	2.1	G032.706−00.061	32.706	−0.061	4.28	6.5	22.505	3.6	3.0
G028.398+00.081	28.398	0.081	26.07	4.5	23.166	4.0	3.5	G032.739+00.192	32.739	0.192	8.28	13.0	22.515	4.1	4.0
G028.438+00.036	28.438	0.036	1.05	4.5	21.905	3.6	1.8	G032.744−00.076	32.744	−0.076	14.26	11.7	23.023	5.0	3.9
G028.469−00.282	28.469	−0.282	1.73	11.6	22.07	3.8	3.1	G032.797+00.191	32.797	0.191	31.65	13.0	23.171	6.1	4.2
G028.579−00.341	28.579	−0.341	7.37	4.7	22.313	3.8	2.9	G032.821−00.331	32.821	−0.331	5.79	5.1	22.609	4.2	2.7
G028.596−00.361	28.596	−0.361	12.48	4.7	22.179	4.4	2.9	G032.990+00.034	32.99	0.034	10.18	9.2	22.681	4.8	3.5
G028.601−00.377	28.601	−0.377	9.73	4.7	22.064	4.1	2.9	G033.133−00.092	33.133	−0.092	15.27	9.4	22.869	5.0	3.7
G028.608+00.019	28.608	0.019	20.21	7.4	22.683	5.0	3.6	G033.134−00.021	33.134	−0.021	2.22	6.5	22.231	3.1	2.8
G028.608−00.027	28.608	−0.027	2.48	2.8	22.017	2.8	1.9	G033.203+00.019	33.203	0.019	9.75	6.5	22.153	3.7	3.3
G028.649+00.027	28.649	0.027	13.53	7.4	22.758	4.5	3.5	G033.206−00.009	33.206	−0.009	11.79	6.5	22.289	4.7	3.2
G028.681+00.032	28.681	0.032	5.34	7.4	22.186	3.5	3.1	G033.264+00.067	33.264	0.067	7.45	6.5	22.507	3.9	3.2
G028.701+00.404	28.701	0.404	2.73	4.7	22.39	2.9	2.6	G033.288−00.019	33.288	−0.019	2.75	6.5	22.22	3.7	2.7
G028.707−00.294	28.707	−0.294	14.36	4.7	22.629	3.7	3.3	G033.338+00.164	33.338	0.164	4.11	5.2	22.26	3.0	2.9
G028.787+00.237	28.787	0.237	6.02	7.4	22.524	4.4	3.1	G033.388+00.199	33.388	0.199	2.62	5.2	22.282	3.6	2.6
G028.802−00.022	28.802	−0.022	6.37	7.4	22.65	3.4	3.5	G033.389+00.167	33.389	0.167	2.14	13.1	22.491	4.1	3.3
G028.812+00.169	28.812	0.169	12.91	7.4	22.576	4.7	3.4	G033.393+00.011	33.393	0.011	19.02	6.5	22.795	4.1	3.7
G028.831−00.252	28.831	−0.252	23.85	4.7	22.941	4.6	3.3	G033.416−00.002	33.416	−0.002	15.89	5.4	22.484	4.1	3.3
G028.861+00.066	28.861	0.066	23.13	7.4	22.786	5.1	3.7	G033.418+00.032	33.418	0.032	2.52	6.5	22.187	3.7	2.6
G028.881−00.021	28.881	−0.021	3.5	7.4	22.541	3.8	3.0	G033.494−00.014	33.494	−0.014	2.59	6.5	22.339	3.8	2.7
G028.974+00.081	28.974	0.081	3.3	10.4	21.821	3.8	3.1	G033.643−00.227	33.643	−0.227	3.78	6.5	22.362	4.1	2.7
G029.002+00.067	29.002	0.067	1.92	10.4	21.955	4.2	2.8	G033.651−00.026	33.651	−0.026	11.84	6.5	22.574	4.1	3.5
G029.016−00.177	29.016	−0.177	3.11	5.8	22.244	3.2	2.8	G033.656−00.019	33.656	−0.019	3.1	6.5	22.368	4.1	2.7
G029.119+00.087	29.119	0.087	4.54	5.6	22.023	3.7	2.8	G033.739−00.021	33.739	−0.021	12.56	6.5	22.997	3.6	3.7
G029.126−00.146	29.126	−0.146	3.74	–	21.87	–	–	G033.809−00.159	33.809	−0.159	2.49	3.2	21.981	2.9	2.0
G029.241+00.251	29.241	0.251	3.95	4.0	22.086	3.2	2.4	G033.811−00.187	33.811	−0.187	6.46	10.8	22.299	5.2	3.3
G029.276−00.129	29.276	−0.129	3.57	4.1	22.216	2.9	2.5	G033.914+00.109	33.914	0.109	31.26	6.5	23.048	5.2	3.7
G029.362−00.316	29.362	−0.316	1.44	5.6	21.756	3.7	2.2	G034.096+00.017	34.096	0.017	10.46	1.6	22.626	2.9	2.1
G029.396−00.094	29.396	−0.094	5.47	7.7	22.841	3.4	3.4	G034.133+00.471	34.133	0.471	5.61	11.6	22.375	5.0	3.4
G029.464+00.009	29.464	0.009	1.44	8.7	21.966	3.4	2.7	G034.169+00.089	34.169	0.089	2.09	1.6	22.182	1.8	1.5
G029.476−00.179	29.476	−0.179	5.35	7.7	22.368	4.0	3.2	G034.221+00.164	34.221	0.164	7.39	1.6	22.184	2.9	1.9
G029.779−00.261	29.779	−0.261	2.36	5.2	22.445	2.4	2.7	G034.229+00.134	34.229	0.134	60.99	1.6	–	–	–
G029.841−00.034	29.841	−0.034	2.72	5.2	22.381	2.9	2.7	G034.241+00.107	34.241	0.107	3.73	1.6	22.314	2.4	1.6
G029.852−00.059	29.852	−0.059	5.89	5.2	22.332	4.3	2.7	G034.243+00.132	34.243	0.132	51.86	1.6	22.732	4.5	2.5
G029.862−00.044	29.862	−0.044	13.1	5.2	22.462	4.7	3.0	G034.244+00.159	34.244	0.159	33.7	1.6	23.089	4.1	2.4
G029.887+00.004	29.887	0.004	9.49	5.2	22.224	4.5	2.9	G034.258+00.109	34.258	0.109	4.58	1.6	22.251	2.9	1.6
G029.889−00.009	29.889	−0.009	8.05	5.2	22.122	4.1	2.8	G034.258+00.154	34.258	0.154	217.0	1.6	23.917	4.8	3.2
G029.899−00.062	29.899	−0.062	7.21	5.2	22.213	3.9	2.9	G034.258+00.166	34.258	0.166	16.59	1.6	23.221	3.5	2.2
G029.911−00.042	29.911	−0.042	52.84	5.2	22.89	4.8	3.8	G034.261+00.176	34.261	0.176	30.85	1.6	–	–	–
G029.921−00.014	29.921	−0.014	6.38	5.2	22.415	3.8	2.8	G034.273+00.141	34.273	0.141	15.79	1.6	22.441	4.7	2.1
G029.931−00.064	29.931	−0.064	27.14	5.2	22.767	4.6	3.5	G034.284+00.184	34.284	0.184	3.77	1.6	22.61	2.0	1.8
G029.937−00.052	29.937	−0.052	23.85	5.2	22.472	4.8	3.3	G034.391+00.214	34.391	0.214	19.02	1.6	–	–	–
G029.941−00.012	29.941	−0.012	10.23	5.2	22.336	3.8	3.1	G034.411+00.234	34.411	0.234	34.74	1.6	23.378	3.5	2.6
G029.952+00.151	29.952	0.151	1.72	5.2	22.234	2.5	2.5	G034.454+00.006	34.454	0.006	4.78	5.3	22.63	3.4	2.9
G029.954−00.016	29.954	−0.016	57.01	5.2	23.142	5.7	3.6	G034.459+00.247	34.459	0.247	15.28	1.6	22.961	2.4	2.5
G029.959−00.067	29.959	−0.067	3.4	5.2	22.194	3.6	2.5	G035.026+00.349	35.026	0.349	17.42	2.3	22.854	4.1	2.4
G029.964−00.012	29.964	−0.012	3.31	5.2	22.476	4.8	2.4	G035.051+00.332	35.051	0.332	6.6	3.1	22.218	2.7	2.6
G029.964−00.414	29.964	−0.414	3.07	4.3	21.815	3.3	2.4	G035.344+00.347	35.344	0.347	1.77	5.9	22.082	3.6	2.4
G029.976−00.047	29.976	−0.047	41.23	5.2	22.83	4.4	3.7	G035.452−00.296	35.452	−0.296	1.94	10.3	22.334	3.9	3.0
G030.010+00.034	30.01	0.034	1.13	5.2	22.226	2.2	2.4	G035.457−00.179	35.457	−0.179	2.19	4.1	22.383	3.1	2.2
G030.013−00.031	30.013	−0.031	9.25	5.2	22.23	3.8	3.0	G035.466+00.141	35.466	0.141	23.2	4.7	22.855	4.7	3.3
G030.019−00.047	30.019	−0.047	27.56	5.2	22.526	4.6	3.5	G035.497−00.021	35.497	−0.021	13.45	10.4	22.336	4.4	3.9
G030.023+00.106	30.023	0.106	10.39	5.2	22.185	4.0	3.1	G035.517−00.034	35.517	−0.034	5.09	10.4	22.047	4.3	3.3
G030.029+00.117	30.029	0.117	9.4	5.2	22.179	4.1	3.0	G035.522−00.274	35.522	−0.274	8.35	2.7	22.866	2.1	3.0
G030.031+00.106	30.031	0.106	7.43	5.2	22.008	3.7	2.8	G035.577+00.047	35.577	0.047	10.09	10.4	22.393	4.5	3.7
G030.094+00.047	30.094	0.047	1.53	5.2	21.906	3.0	2.3	G035.577+00.067	35.577	0.067	22.04	10.4	22.69	5.0	4.0
G030.138−00.071	30.138	−0.071	4.98	5.2	22.505	2.3	3.3	G035.579−00.031	35.579	−0.031	18.05	10.4	22.906	5.3	3.8

TABLE 8
–continuum Clump properties of all 325 ATLASGAL clumps to search for outflows

ATLASGAL CSC Gname	ℓ (°)	b (°)	F_{int} (Jy)	Dist. (kpc)	$logN_{H_2}$ (cm^{-2})	$logL_{bol}$ ($logL_\odot$)	$logM_{clump}$ ($logM_\odot$)
G030.198−00.169	30.198	−0.169	5.56	5.2	22.223	4.2	2.7
G030.201−00.157	30.201	−0.157	6.61	5.2	21.896	4.3	2.7
G030.213−00.187	30.213	−0.187	23.18	5.2	22.592	4.5	3.4
G030.224−00.179	30.224	−0.179	7.89	5.2	22.315	4.2	2.9
G030.251+00.054	30.251	0.054	7.66	5.2	22.325	4.0	2.9
G030.294+00.056	30.294	0.056	8.08	5.2	22.413	3.9	2.9
G030.299−00.202	30.299	−0.202	16.06	5.2	22.325	3.9	3.3
G030.341−00.116	30.341	−0.116	9.45	5.2	22.496	3.1	3.2
G030.348+00.097	30.348	0.097	4.16	5.2	22.007	3.4	2.6
G030.348+00.392	30.348	0.392	4.9	5.0	22.488	3.3	2.8
G030.351+00.086	30.351	0.086	2.08	5.2	22.003	3.4	2.3
G030.386−00.104	30.386	−0.104	25.2	5.2	22.53	4.6	3.4
G030.399−00.102	30.399	−0.102	8.94	5.2	22.051	4.0	3.0
G030.399−00.296	30.399	−0.296	3.6	5.2	22.457	3.3	2.7
G030.419−00.231	30.419	−0.231	23.55	5.2	23.055	4.3	3.5
G030.424−00.214	30.424	−0.214	7.53	5.2	22.624	3.2	3.1
G030.426−00.267	30.426	−0.267	11.63	5.2	21.929	4.1	3.0
G030.488−00.301	30.488	−0.301	6.05	5.2	21.875	3.5	2.7
G030.493−00.391	30.493	−0.391	5.44	0.4	22.334	–	0.8
G030.513+00.031	30.513	0.031	2.29	2.7	22.014	2.5	1.9
G030.534+00.021	30.534	0.021	9.78	2.7	22.508	3.9	2.4
G030.588−00.042	30.588	−0.042	25.61	2.7	22.904	4.0	2.9
G030.623−00.111	30.623	−0.111	4.37	5.2	22.303	3.1	2.9
G030.624+00.169	30.624	0.169	13.83	5.2	22.294	3.3	3.3
G030.641−00.117	30.641	−0.117	1.94	5.2	22.052	3.3	2.4
G030.648−00.119	30.648	−0.119	2.64	5.2	22.08	3.2	2.5
G030.651−00.204	30.651	−0.204	10.43	5.2	22.738	3.8	3.2
G030.659+00.229	30.659	0.229	3.41	5.2	22.315	3.4	2.7
G030.663−00.144	30.663	−0.144	5.71	5.2	22.317	3.7	2.9
G030.683−00.074	30.683	−0.074	17.24	5.2	22.744	4.7	3.2
G030.684−00.261	30.684	−0.261	5.48	5.2	22.378	4.4	2.7
G030.693−00.149	30.693	−0.149	3.39	5.2	22.267	3.0	2.8
G030.703−00.067	30.703	−0.067	99.54	5.2	23.424	5.2	4.0
G030.691−00.054	30.691	−0.054	60.1	5.2	23.424	5.2	3.8
G030.718−00.082	30.718	−0.082	50.64	5.2	23.271	4.7	3.8
G030.731−00.079	30.731	−0.079	14.74	5.2	22.903	3.9	3.3
G030.741−00.061	30.741	−0.061	75.23	5.2	22.904	5.4	3.8
G030.746−00.001	30.746	−0.001	78.93	5.2	–	–	–
G030.753−00.051	30.753	−0.051	33.49	5.2	22.76	5.5	3.4
G030.756+00.206	30.756	0.206	18.54	5.2	22.601	4.0	3.4
G030.763−00.031	30.763	−0.031	12.94	5.2	22.145	5.1	2.7
G030.766−00.046	30.766	−0.046	10.25	5.2	22.388	4.9	2.8
G030.769−00.087	30.769	−0.087	10.63	5.2	22.49	3.9	3.2
G030.773−00.216	30.773	−0.216	21.89	5.2	–	–	–
G030.783−00.262	30.783	−0.262	1.01	2.7	22.325	1.6	1.9
G030.784−00.021	30.784	−0.021	95.09	5.2	22.695	5.8	3.8
G030.786+00.204	30.786	0.204	9.99	5.2	22.921	3.9	3.1
G030.813−00.024	30.813	−0.024	17.21	5.2	22.825	4.4	3.3
G030.818+00.274	30.818	0.274	2.74	5.2	22.111	4.1	2.3
G030.818−00.056	30.818	−0.056	113.85	5.2	23.669	5.4	4.1
G030.819−00.081	30.819	−0.081	1.78	5.2	22.27	3.2	2.4
G030.823−00.156	30.823	−0.156	16.48	5.2	22.605	4.6	3.5
G030.828+00.134	30.828	0.134	9.0	2.7	22.172	3.0	2.5
G030.828−00.122	30.828	−0.122	1.18	2.7	22.029	2.9	1.5
G030.839−00.019	30.839	−0.019	12.82	5.2	22.555	3.3	3.4
G030.853−00.109	30.853	−0.109	9.65	5.2	22.329	3.9	3.1
G030.866+00.114	30.866	0.114	13.16	2.7	22.641	4.1	2.5
G030.866−00.119	30.866	−0.119	11.92	5.2	22.338	3.9	3.3
G030.874−00.094	30.874	−0.094	4.61	5.2	22.314	3.7	2.7
G030.886−00.231	30.886	−0.231	2.8	5.2	21.917	3.2	2.5
G030.893+00.139	30.901	0.147	1.8	5.2	23.023	3.3	2.5
G030.898+00.162	30.898	0.162	17.69	5.2	22.694	4.0	3.3
G030.901−00.034	30.901	−0.034	1.23	5.2	22.26	2.6	2.3
G030.908+00.027	30.908	0.027	7.06	5.2	22.049	3.2	3.0
G030.919+00.091	30.919	0.091	4.68	5.2	22.55	3.3	2.9
G030.959+00.086	30.959	0.086	8.77	2.7	22.459	3.6	2.4
G030.969−00.044	30.969	−0.044	1.44	5.2	22.133	2.5	2.4
G030.971−00.141	30.971	−0.141	17.45	5.2	22.841	3.8	3.6
G030.978+00.216	30.978	0.216	8.34	5.2	22.445	3.7	3.1
G030.994+00.236	30.994	0.236	19.85	5.2	22.378	3.3	3.5
G030.996−00.076	30.996	−0.076	5.46	5.2	22.465	3.8	2.8
G031.024+00.262	31.024	0.262	24.42	5.2	22.627	3.6	3.8
G031.046+00.357	31.046	0.357	8.83	5.2	22.436	4.0	3.0
G031.054+00.469	31.054	0.469	7.43	2.0	22.295	3.5	2.1
G031.071+00.049	31.071	0.049	2.76	2.7	21.911	3.8	1.7
G031.121+00.062	31.121	0.062	3.35	2.7	22.031	2.8	2.0
G031.148−00.149	31.148	−0.149	4.22	2.7	21.988	2.8	2.1
G031.158+00.047	31.158	0.047	8.87	2.7	22.564	3.3	2.5
G031.208+00.101	31.208	0.101	3.0	5.2	21.998	3.7	2.5
G031.239+00.062	31.239	0.062	7.17	5.2	22.515	3.2	3.2
G031.239−00.057	31.239	−0.057	5.06	2.7	22.298	2.1	2.5
G031.243−00.111	31.243	−0.111	8.0	12.9	22.691	5.3	3.6

ATLASGAL CSC Gname	ℓ (°)	b (°)	F_{int} (Jy)	Dist. (kpc)	N_{H_2} (cm^{-2})	$logL_{bol}$ ($L_\odot$)	$logM_{clump}$ ($M_\odot$)
G035.602+00.222	35.602	0.222	2.38	3.0	22.31	2.0	2.2
G035.604−00.202	35.604	−0.202	3.04	3.0	22.141	2.8	2.1
G035.681−00.176	35.681	−0.176	6.97	2.1	22.758	2.3	2.4
G036.406+00.021	36.406	0.021	5.41	3.5	22.556	3.9	2.3
G036.433−00.169	36.433	−0.169	5.4	4.6	22.242	3.0	2.9
G036.794−00.204	36.794	−0.204	5.05	5.8	22.241	3.5	3.0
G036.826−00.039	36.826	−0.039	5.01	3.6	22.399	2.4	2.7
G037.043−00.036	37.043	−0.036	8.16	5.8	22.666	3.7	3.2
G037.199−00.419	37.199	−0.419	2.92	2.2	22.424	2.4	1.9
G037.268+00.081	37.268	0.081	10.35	5.8	22.728	3.9	3.3
G037.341−00.062	37.341	−0.062	6.71	9.7	22.421	4.6	3.4
G037.374−00.236	37.374	−0.236	9.22	2.2	22.228	3.5	2.3
G037.444+00.137	37.444	0.137	2.82	2.2	22.109	1.5	2.0
G037.479−00.106	37.479	−0.106	3.7	9.7	22.35	4.0	3.2
G037.546−00.112	37.546	−0.112	9.43	9.7	22.55	5.1	3.4
G037.638−00.104	37.638	−0.104	1.58	9.7	21.945	4.2	2.7
G037.671+00.142	37.671	0.142	4.41	4.9	22.089	3.3	2.7
G037.672−00.091	37.672	−0.091	1.39	9.7	22.081	3.2	2.9
G037.734−00.112	37.734	−0.112	9.32	9.7	22.756	4.6	3.6
G037.764−00.216	37.764	−0.216	21.78	9.7	22.765	5.0	3.9
G037.819+00.412	37.819	0.412	7.57	12.3	22.744	4.8	3.7
G037.874−00.399	37.874	−0.399	18.45	9.7	22.799	5.7	3.6
G038.037−00.041	38.037	−0.041	2.28	3.3	22.059	3.0	2.0
G038.119−00.229	38.119	−0.229	2.65	6.5	22.274	4.0	2.6
G038.646−00.226	38.646	−0.226	2.86	–	22.172	–	–
G038.694−00.452	38.694	−0.452	4.51	9.8	22.556	4.2	3.3
G038.909−00.462	38.909	−0.462	2.87	1.9	22.111	2.2	1.7
G038.917−00.402	38.917	−0.402	3.96	1.9	21.982	2.3	1.8
G038.921−00.351	38.921	−0.351	20.17	1.9	22.91	3.3	2.6
G038.934−00.361	38.934	−0.361	12.79	1.9	22.55	3.2	2.4
G038.937−00.457	38.937	−0.457	9.3	1.9	22.521	2.5	2.3
G038.957−00.466	38.957	−0.466	14.71	1.9	22.844	2.1	2.8
G039.268−00.051	39.268	−0.051	4.81	11.8	22.401	4.4	3.5
G039.388−00.141	39.388	−0.141	5.51	3.4	22.541	3.8	2.3
G039.434−00.187	39.434	−0.187	2.23	3.3	22.015	2.8	2.0
G039.591−00.204	39.591	−0.204	5.26	–	22.346	–	–
G039.851−00.204	39.851	−0.204	4.4	9.3	22.249	3.4	3.4
G039.884−00.346	39.884	−0.346	7.05	9.3	22.469	4.6	3.3
G040.283−00.219	40.283	−0.219	13.24	6.4	23.079	4.5	3.3
G040.622−00.137	40.622	−0.137	11.17	10.6	22.738	5.0	3.7
G040.814−00.416	40.814	−0.416	1.04	3.4	21.998	2.6	1.7
G041.031−00.226	41.031	−0.226	3.29	8.9	22.26	3.9	3.1
G041.077−00.124	41.077	−0.124	4.09	8.9	22.277	3.6	3.3
G041.099−00.237	41.099	−0.237	5.95	8.9	22.084	4.4	3.2
G041.122−00.219	41.122	−0.219	7.96	8.9	22.359	3.8	3.6
G041.161−00.184	41.161	−0.184	6.73	8.9	22.326	4.2	3.4
G041.226−00.197	41.226	−0.197	3.59	8.9	22.275	3.9	3.2
G041.307−00.171	41.307	−0.171	4.1	8.9	22.361	3.3	3.4
G041.377+00.037	41.377	0.037	3.35	8.9	22.159	4.3	3.0
G041.507−00.106	41.507	−0.106	0.92	8.9	22.133	3.4	2.6
G042.108−00.447	42.108	−0.447	6.0	3.4	22.303	3.7	2.4
G042.164−00.077	42.164	−0.077	1.19	9.9	22.238	3.1	2.9
G042.421−00.259	42.421	−0.259	7.26	4.4	22.138	4.0	2.7
G043.038−00.452	43.038	−0.452	7.32	–	22.803	–	–
G043.108+00.044	43.108	0.044	13.22	11.1	22.326	4.8	3.9
G043.124+00.031	43.124	0.031	22.3	11.1	22.419	5.1	4.1
G043.148+00.014	43.148	0.014	48.87	11.1	22.894	5.9	4.3
G043.164−00.029	43.164	−0.029	86.15	11.1	23.265	6.2	4.5
G043.166+00.011	43.166	0.011	319.98	11.1	23.892	6.9	5.0
G043.178−00.011	43.178	−0.011	47.31	11.1	22.882	6.6	4.2
G043.236−00.047	43.236	−0.047	18.83	11.1	22.904	5.1	4.0
G043.306−00.212	43.306	−0.212	7.95	4.2	22.78	4.1	2.7
G043.519+00.016	43.519	0.016	2.75	4.3	22.483	2.5	2.6
G043.528+00.017	43.528	0.017	3.32	4.3	22.385	2.6	2.6
G043.794−00.127	43.794	−0.127	13.83	6.0	22.876	5.1	3.1
G043.817−00.119	43.817	−0.119	1.86	6.0	22.106	3.2	2.5
G043.994−00.012	43.994	−0.012	4.23	6.0	22.311	4.1	2.7
G044.309+00.041	44.309	0.041	12.23	8.1	22.698	4.5	3.5
G045.071+00.132	45.071	0.132	20.13	8.0	22.885	5.7	3.5
G045.086+00.132	45.086	0.132	1.24	8.0	22.206	3.7	2.6
G045.121+00.131	45.121	0.131	42.78	8.0	22.958	6.0	3.9
G045.454+00.061	45.454	0.061	35.12	8.4	22.702	5.8	3.8
G045.463+00.027	45.463	0.027	7.2	8.4	22.293	4.7	3.3
G045.474+00.134	45.474	0.134	20.08	8.4	22.641	5.5	3.6
G045.543−00.007	45.543	−0.007	2.51	8.4	22.015	4.3	2.8
G045.544−00.032	45.544	−0.032	3.37	8.4	22.122	3.7	3.0
G045.568−00.121	45.568	−0.121	1.49	0.3	22.063	0.5	-0.3
G045.776−00.254	45.776	−0.254	2.95	5.8	22.305	3.0	2.8
G045.804−00.356	45.804	−0.356	3.65	5.8	22.458	4.0	2.7
G045.821−00.284	45.821	−0.284	4.09	5.8	22.181	4.2	2.7
G045.829−00.292	45.829	−0.292	3.48	5.8	22.063	4.0	2.5
G045.936−00.402	45.936	−0.402	5.6	5.8	22.246	4.5	2.8
G046.118+00.399	46.118	0.399	5.74	7.5	22.348	4.0	3.3

TABLE 9
^{13}CO outflow calculations of all blue and red wings for 225 ATLASGAL clumps: observed peak ^{13}CO and C^{18}O velocities, the antenna temperatures are corrected for main-beam efficiency (0.72), the velocity range $\Delta V_{b/r}$ for blue and red wings of ^{13}CO spectra, the maximum projected velocity for blue and red shifted $V_{max_{b/r}}$ relative to the peak C^{18}O velocity.

ATLASGAL CSC Gname	^{13}CO v_p (km s^{-1})	^{13}CO T_{mb} (K)	C^{18}O v_p (km s^{-1})	C^{18}O T_{mb} (K)	ΔV_b (km s^{-1})	ΔV_r (km s^{-1})	V_{max_b} (km s^{-1})	V_{max_r} (km s^{-1})
G027.784+00.057	101.2	5.9	100.8	1.8	[96.3,100.8]	[103.8,104.8]	4.5	4.0
G027.903−00.012	97.9	6.3	97.5	4.9	[95.3,96.8]	[98.8,100.3]	2.2	2.8
G027.919−00.031	47.6	6.1	47.7	3.7	[46.3,46.8]	[48.3,49.8]	1.4	2.1
G027.936+00.206	42.3	6.2	42.0	2.3	[37.3,40.3]	[43.8,46.8]	4.7	4.8
G027.978+00.077	74.7	4.2	75.3	2.9	[71.8,73.3]	[76.8,79.3]	3.5	4.0
G028.148−00.004	98.6	4.0	98.5	3.1	[96.3,97.8]	[99.8,100.8]	2.2	2.3
G028.151+00.171	89.7	4.8	89.6	2.1	[86.8,88.8]	[90.8,92.3]	2.8	2.7
G028.199−00.049	96.3	6.8	95.6	3.6	[89.3,95.8]	[98.3,107.3]	6.3	11.7
G028.231+00.041	107.0	3.3	107.0	1.2	[104.8,105.8]	[107.3,110.3]	2.2	3.3
G028.234+00.062	107.1	4.9	107.0	1.8	[104.8,105.8]	[107.8,108.8]	2.2	1.8
G028.244+00.012	106.0	6.7	106.6	2.4	[103.8,104.8]	[106.8,109.3]	2.8	2.7
G028.288−00.362	48.3	7.8	47.8	4.4	[42.3,47.8]	[50.3,53.3]	5.5	5.5
G028.301−00.382	84.8	11.4	84.6	3.8	[80.8,84.3]	[86.3,88.8]	3.8	4.2
G028.321−00.009	100.0	5.1	99.6	2.0	[96.3,98.8]	[100.8,101.8]	3.3	2.2
G028.388+00.451	83.9	7.9	83.7	3.6	[81.8,82.3]	[84.3,87.3]	1.9	3.6
G028.398+00.081	77.6	4.1	78.5	2.9	–	[79.8,81.8]	–	3.3
G028.438+00.036	83.1	12.2	83.1	5.0	[80.3,82.3]	[83.8,85.3]	2.8	2.2
G028.469−00.282	48.3	5.5	48.3	4.4	[46.3,47.3]	[48.8,50.3]	2.0	2.0
G028.608+00.019	102.1	8.3	101.7	38	[96.3,99.8]	[102.3,107.3]	5.4	5.6
G028.608−00.027	45.2	8.9	45.6	3.7	[41.8,44.3]	[46.3,46.8]	3.8	1.2
G028.649+00.027	103.1	7.8	103.4	3.7	–	[104.3,108.8]	–	5.4
G028.707−00.294	89.2	4.4	88.7	2.3	[86.8,88.3]	[89.8,90.8]	1.9	2.1
G028.802−00.022	100.7	3.1	99.6	1.8	[96.8,98.3]	[101.8,104.3]	2.8	4.7
G028.812+00.169	105.4	8.1	105.1	2.9	[101.3,104.3]	[106.8,109.3]	3.8	4.2
G028.831−00.252	87.4	6.0	87.2	3.0	[82.3,85.8]	[87.8,96.8]	4.9	9.6
G028.861+00.066	102.8	7.7	103.2	3.6	[97.3,99.3]	[103.8,109.8]	5.9	6.6
G028.881−00.021	101.1	7.7	101.0	3.5	[98.3,100.8]	[102.3,103.3]	2.7	2.3
G028.974+00.081	72.0	5.5	72.1	2.5	[69.3,71.3]	[72.8,73.8]	2.8	1.7
G029.002+00.067	70.0	18.1	71.2	6.0	[68.0,69.5]	[70.5,71.5]	3.2	0.3
G029.476−00.179	105.3	9.7	105.4	4.6	[103.2,104.2]	[106.2,109.2]	2.2	3.8
G029.852−00.059	99.4	26.9	99.5	10.2	[97.7,98.2]	[100.7,102.7]	1.8	3.2
G029.862−00.044	101.2	11.8	100.8	4.4	[94.7,100.2]	[103.2,106.2]	6.1	5.4
G029.889−00.009	97.3	12.1	95.2	3.8	[91.7,95.2]	[100.2,102.7]	3.5	7.5
G029.899−00.062	100.6	8.3	100.9	3.5	[97.2,100.2]	[102.2,104.2]	3.7	3.3
G029.911−00.042	99.5	14.8	99.8	3.9	[92.2,96.7]	[101.7,105.7]	7.6	5.9
G029.931−00.064	98.8	6.8	99.3	3.2	[90.7,96.7]	[99.7,107.2]	8.6	7.9
G029.937−00.052	99.9	6.6	99.9	2.8	[92.7,97.7]	[102.7,109.2]	7.2	9.3
G029.954−00.016	97.8	13.8	97.5	14.4	[92.1,96.6]	[101.1,104.6]	5.4	7.1
G029.959−00.067	101.1	7.9	102.6	4.7	[97.2,100.2]	[102.2,105.2]	5.4	2.6
G029.964−00.012	98.2	14.8	98.6	8.1	[91.7,95.7]	[100.2,104.7]	6.9	6.1
G029.976−00.047	99.1	7.4	101.6	1.9	[89.7,97.2]	[100.7,105.7]	11.9	4.1
G030.008−00.272	103.1	2.4	103.1	1.6	[100.6,102.6]	[105.6,107.6]	2.5	4.5
G030.010+00.034	103.0	14.4	105.6	1.8	[99.6,100.1]	[105.1,106.1]	6.0	0.5
G030.019−00.047	95.3	10.6	92.6	2.3	[87.1,93.1]	[99.6,103.6]	5.5	11.0
G030.023+00.106	106.2	7.5	106.2	2.8	[100.6,105.1]	[106.6,109.6]	5.6	3.4
G030.029+00.117	106.3	6.0	106.0	2.8	[103.6,105.6]	[107.1,109.1]	2.4	3.1
G030.094+00.047	105.4	5.1	106.3	1.3	[102.1,105.1]	[106.1,107.1]	4.2	0.8
G030.198−00.169	103.2	6.5	103.1	3.2	[99.6,101.6]	[103.6,109.1]	3.5	6.0
G030.201−00.157	103.1	7.0	103.3	2.3	[101.1,102.6]	[103.6,104.6]	2.2	1.3
G030.213−00.187	104.9	7.7	104.8	3.7	[101.1,104.1]	[106.1,109.1]	3.7	4.3
G030.224−00.179	103.8	16.7	103.8	7.3	[100.1,102.6]	[104.1,109.6]	3.7	5.8
G030.251+00.054	71.0	3.4	71.0	1.5	–	[72.4,73.9]	–	2.9
G030.299−00.202	102.4	7.6	102.1	2.6	[99.6,101.6]	[103.6,106.6]	2.5	4.5
G030.348+00.392	92.9	6.2	92.8	2.9	[90.9,91.9]	[93.9,95.4]	1.9	2.6
G030.351+00.086	96.3	4.6	96.8	3.0	[94.4,95.4]	[97.4,98.9]	2.4	2.1
G030.386−00.104	86.9	11.5	86.9	5.8	[84.1,86.1]	[88.6,89.1]	2.8	2.2
G030.399−00.102	87.4	7.0	87.9	3.3	[85.6,87.1]	[89.1,90.1]	2.3	2.2
G030.399−00.296	101.8	7.3	102.2	2.4	[96.1,99.6]	[102.6,107.1]	6.1	4.9
G030.419−00.231	104.8	10.8	104.8	3.9	[95.9,103.9]	[105.9,113.4]	8.9	8.6
G030.426−00.267	103.3	9.3	103.0	3.0	[101.4,102.9]	[104.9,105.4]	1.6	2.4
G030.534+00.021	48.1	11.6	48.0	3.1	[39.9,46.9]	[49.8,54.4]	8.1	6.4
G030.588−00.042	42.1	5.2	41.9	2.3	[33.9,41.4]	[44.4,49.4]	8.0	7.5
G030.623−00.111	113.8	8.0	113.9	2.5	[111.4,113.4]	[114.9,115.9]	2.5	2.0
G030.624+00.169	105.3	7.0	105.5	2.9	[102.4,104.4]	[106.4,107.4]	3.1	1.9
G030.641−00.117	114.2	11.7	114.5	4.3	[112.4,112.9]	[114.9,115.9]	2.1	1.4
G030.648−00.119	114.1	7.7	114.4	2.8	[112.4,113.4]	[114.9,115.9]	2.0	1.5
G030.651−00.204	90.7	5.0	90.5	1.9	[83.4,89.4]	[93.4,100.9]	7.1	10.4
G030.659+00.229	100.5	5.1	100.4	2.9	[98.4,99.4]	[101.4,101.9]	2.0	1.5
G030.663−00.144	116.2	5.4	116.0	1.7	[113.4,115.9]	[117.9,118.4]	2.6	2.4
G030.683−00.074	91.7	7.5	92.0	6.1	[84.4,91.4]	[93.9,98.9]	7.6	6.9
G030.684−00.261	103.2	8.2	103.7	4.5	[98.9,101.4]	[104.9,107.4]	4.8	3.7
G030.693−00.149	91.5	4.9	91.5	1.7	[88.4,89.4]	[92.4,95.4]	3.1	3.9
G030.691−00.05	91.5	8.9	90.9	2.6	[76.4,88.4]	[96.4,105.9]	14.5	15.0
G030.703−00.067	92.2	15.1	91.0	4.2	[82.9,89.4]	[96.4,104.4]	8.1	13.4
G030.691+00.22	104.6	6.8	104.8	4.8	[102.8,103.8]	–	2.0	-
G030.718−00.082	93.2	7.5	93.1	4.3	[85.9,91.9]	[96.4,102.4]	7.2	9.3
G030.731−00.079	92.4	7.5	91.1	3.3	[83.4,90.4]	[94.9,99.4]	7.7	8.3

TABLE 9
–continuum ^{13}CO outflow calculations of all blue and red wings for 225 ATLASGAL clumps

ATLASGAL CSC Gname	^{13}CO v_p (km s^{-1})	^{13}CO T_{mb} (K)	C^{18}O v_p (km s^{-1})	C^{18}O T_{mb} (K)	ΔV_b (km s^{-1})	ΔV_r (km s^{-1})	V_{max_b} (km s^{-1})	V_{max_r} (km s^{-1})
G030.741−00.061	93.6	8.5	93.1	3.6	[80.9,90.9]	[96.9,106.4]	12.2	13.3
G030.746−00.001	91.0	3.1	91.9	1.1	[75.9,87.4]	[92.4,107.9]	16.0	16.0
G030.753−00.051	93.6	13.6	91.5	6.6	[85.9,91.4]	[95.9,100.4]	5.6	8.9
G030.756+00.206	99.0	3.0	99.5	2.1	[95.9,97.4]	[100.4,101.9]	3.6	2.4
G030.763−00.031	94.3	8.2	94.1	3.6	[77.9,92.9]	[95.9,110.4]	16.2	16.3
G030.766−00.046	92.3	15.5	89.8	3.9	[77.4,89.9]	[95.9,106.4]	12.4	16.6
G030.769−00.087	94.2	7.0	94.2	2.8	[88.9,93.4]	[96.4,103.9]	5.3	9.7
G030.773−00.216	103.7	3.6	103.8	1.5	[96.9,102.9]	[105.9,111.9]	6.9	8.1
G030.784−00.021	94.4	6.6	94.3	2.0	[77.4,90.9]	[97.4,111.9]	16.9	17.6
G030.786+00.204	81.8	5.9	81.9	3.8	[73.9,80.4]	[83.4,89.4]	8.0	7.5
G030.813−00.024	95.6	8.3	95.4	3.5	[89.4,94.9]	[96.9,100.4]	6.0	5.0
G030.818+00.274	97.9	6.3	97.9	3.2	[94.9,97.4]	[98.9,100.4]	3.0	2.5
G030.818−00.056	97.3	9.2	96.9	2.5	[85.4,95.9]	[100.9,106.4]	11.5	9.5
G030.819−00.081	94.9	5.4	94.8	2.0	[92.4,94.4]	[98.4,100.4]	2.4	5.6
G030.823−00.156	104.3	3.7	104.2	1.9	[88.9,103.4]	[106.9,113.9]	15.3	9.7
G030.828+00.134	38.0	5.7	37.8	2.4	[35.4,36.9]	[39.4,40.4]	2.4	2.6
G030.828−00.122	51.3	7.2	51.6	3.8	[48.4,50.4]	[51.9,54.4]	3.2	2.8
G030.839−00.019	93.0	4.9	92.4	1.7	[84.9,92.4]	[94.9,97.9]	7.5	5.5
G030.853−00.109	99.4	2.9	100.2	2.2	[93.4,96.4]	[100.9,105.4]	6.8	5.2
G030.866+00.114	39.4	10.3	39.3	3.1	[35.9,37.4]	[41.9,44.9]	3.4	5.6
G030.866−00.119	99.8	2.5	100.7	1.0	[84.9,98.4]	[101.4,106.9]	15.8	6.2
G030.874−00.094	100.8	9.6	101.2	5.3	[95.9,99.4]	[101.9,104.4]	5.3	3.2
G030.886−00.231	111.0	8.9	111.2	3.0	[106.4,110.4]	[111.4,113.9]	4.8	2.7
G030.898+00.162	105.6	6.2	105.6	1.9	[91.4,103.9]	[105.9,109.9]	14.2	4.3
G030.901−00.034	75.4	7.4	74.9	3.8	[73.4,74.4]	[76.9,77.4]	1.5	2.5
G030.959+00.086	39.8	6.9	39.6	2.4	[34.7,39.2]	[40.7,45.2]	4.9	5.6
G030.971−00.141	77.8	2.8	77.6	0.9	[75.4,77.4]	[78.9,81.4]	2.2	3.8
G030.978+00.216	107.8	4.9	108.0	3.5	[105.7,106.2]	[109.2,110.7]	2.3	2.7
G030.996−00.076	81.6	14.3	81.7	5.2	[75.9,79.9]	[81.9,84.4]	5.8	2.7
G031.024+00.262	96.2	3.0	96.1	1.2	[91.7,95.7]	[96.7,98.2]	4.4	2.1
G031.046+00.357	77.0	7.7	77.0	4.0	[72.7,76.2]	[78.2,79.2]	4.3	2.2
G031.071+00.049	38.2	9.7	37.9	2.6	[34.7,37.2]	[39.2,41.2]	3.2	3.3
G031.121+00.062	42.1	7.5	42.1	3.3	[36.2,41.7]	[43.2,46.2]	5.9	4.1
G031.148−00.149	41.7	2.6	42.2	0.9	[39.7,40.7]	[43.2,44.2]	2.5	2.0
G031.158+00.047	39.0	5.7	39.2	2.7	[34.2,38.2]	[42.7,43.7]	5.0	4.5
G031.208+00.101	108.1	7.1	108.1	3.3	[106.2,107.7]	[108.7,110.2]	1.9	2.1
G031.243−00.111	20.6	10.5	21.5	4.1	[16.7,18.7]	[23.7,25.7]	4.8	4.2
G031.281+00.062	108.3	6.5	108.8	2.9	[101.2,105.7]	[110.7,113.7]	7.6	4.9
G031.386−00.269	87.4	7.1	86.5	4.6	[84.7,86.7]	[88.7,92.2]	1.8	5.7
G031.396−00.257	87.1	19.2	86.6	8.4	[81.7,85.7]	[87.7,92.7]	4.9	6.1
G031.412+00.307	97.7	5.9	97.4	3.4	[92.7,95.7]	[100.2,102.2]	4.7	4.8
G031.542−00.039	44.8	3.5	44.5	1.1	[43.2,44.2]	[45.7,46.7]	1.3	2.2
G031.568+00.092	96.2	6.5	96.2	3.0	[94.2,95.2]	[96.7,97.7]	2.0	1.5
G031.581+00.077	96.0	9.4	95.8	6.9	[91.7,95.2]	[98.2,101.7]	4.1	5.9
G031.596+00.33	99.7	4.6	99.7	1.3	[95.2,98.7]	[101.2,104.7]	4.5	5.0
G031.644−00.266	43.9	6.5	43.9	2.8	[41.7,43.2]	[44.7,46.2]	2.2	2.3
G032.019+00.064	98.6	4.7	99.2	2.1	[90.4,96.9]	[99.4,101.4]	8.8	2.2
G032.044+00.059	95.1	7.0	95.3	1.8	–	[97.9,99.9]	–	4.6
G032.117+00.091	96.5	10.6	96.2	5.5	[90.9,94.9]	[97.4,101.4]	5.3	5.2
G032.149+00.134	94.4	9.8	94.4	3.1	[90.4,91.9]	[95.4,98.4]	4.0	4.0
G032.456+00.387	48.9	8.0	48.6	3.8	[46.3,48.3]	[49.3,52.3]	2.3	3.7
G032.471+00.204	49.2	6.1	49.4	2.1	[45.3,48.8]	[51.3,53.8]	4.1	4.4
G032.604−00.256	90.2	7.5	90.4	3.4	[88.3,89.8]	[91.8,92.8]	2.1	2.4
G032.739+00.192	19.0	4.3	19.0	1.3	[14.3,17.3]	[19.8,23.3]	4.7	4.3
G032.744−00.076	37.4	5.7	37.5	2.0	[30.3,35.8]	[39.3,42.8]	7.2	5.3
G032.797+00.191	14.4	13.8	14.7	5.4	[6.8,11.8]	[16.3,21.8]	7.9	7.1
G032.821−00.331	79.4	3.8	78.8	2.4	[75.3,78.3]	[80.8,85.3]	3.5	6.5
G032.990+00.034	82.6	5.3	82.5	3.2	[78.3,81.3]	[83.3,88.3]	4.2	5.8
G033.133−00.092	76.5	8.1	76.3	3.9	[69.8,74.3]	[77.8,82.8]	6.5	6.5
G033.203+00.019	101.0	4.7	101.1	2.5	[98.3,99.3]	[101.3,102.8]	2.8	1.7
G033.206−00.009	99.7	5.7	99.6	2.8	[96.3,97.8]	[100.3,102.8]	3.3	3.2
G033.264+00.067	98.6	5.1	98.8	3.7	[96.3,97.8]	[100.3,100.8]	2.5	2.0
G033.288−00.019	99.4	7.5	99.4	5.3	[97.8,98.3]	[100.3,102.8]	1.6	3.4
G033.338+00.164	85.1	11.7	85.2	4.7	[82.8,84.8]	[85.8,87.3]	2.4	2.1
G033.388+00.199	85.4	8.1	85.1	3.9	[83.3,84.3]	[85.8,87.3]	1.8	2.2
G033.389+00.167	9.3	5.6	9.4	2.9	[6.8,8.8]	[9.8,11.8]	2.6	2.4
G033.393+00.011	103.2	5.1	103.5	1.8	[94.3,102.8]	[104.8,107.8]	9.2	4.3
G033.416−00.002	74.6	7.1	74.4	1.5	[71.2,73.7]	[76.7,77.7]	3.2	3.3
G033.418+00.032	103.4	8.8	103.4	4.3	[101.2,102.7]	[104.2,105.7]	2.2	2.3
G033.651−00.026	103.9	5.0	104.2	2.8	[102.7,103.2]	[105.7,107.7]	1.5	3.5
G033.739−00.021	105.7	2.1	105.8	1.0	[102.7,104.7]	[107.2,108.7]	3.1	2.9
G033.809−00.159	52.2	10.2	52.7	3.4	[50.2,51.2]	[52.7,54.2]	2.5	1.5
G033.914+00.109	107.7	11.4	107.6	4.9	[102.9,106.9]	[108.9,112.9]	4.7	5.3
G034.096+00.017	57.1	3.4	57.6	2.1	[52.9,55.4]	[57.9,61.4]	4.7	3.8
G034.221+00.164	57.5	8.8	57.7	3.4	[54.9,56.4]	[59.4,62.4]	2.8	4.7
G034.229+00.134	57.4	14.4	57.7	6.0	[51.9,56.4]	[58.4,64.9]	5.8	7.2
G034.241+00.107	56.1	18.7	56.3	7.5	[52.4,54.9]	[56.4,58.9]	3.9	2.6
G034.243+00.132	56.9	16.4	57.0	6.9	[51.9,55.4]	[57.4,62.9]	5.1	5.9
G034.244+00.159	58.3	19.3	58.0	5.7	[49.9,56.4]	[61.4,67.4]	8.1	9.4

TABLE 9
–continuum ^{13}CO outflow calculations of all blue and red wings for 225 ATLASGAL clumps

ATLASGAL CSC Gname	^{13}CO v_p (km s^{-1})	^{13}CO T_{mb} (K)	C^{18}O v_p (km s^{-1})	C^{18}O T_{mb} (K)	ΔV_b (km s^{-1})	ΔV_r (km s^{-1})	V_{max_b} (km s^{-1})	V_{max_r} (km s^{-1})
G034.258+00.109	55.2	17.2	54.5	7.0	[52.4,54.4]	[56.4,59.4]	2.1	4.9
G034.258+00.154	58.5	30.6	57.7	10.6	[49.9,56.4]	[62.9,66.4]	7.8	8.7
G034.258+00.166	58.2	13.0	58.8	6.0	[52.9,56.9]	[62.4,65.4]	5.9	6.6
G034.261+00.176	58.7	5.8	58.6	2.5	[51.4,57.9]	[60.4,64.9]	7.2	6.3
G034.273+00.141	58.6	10.0	58.9	3.5	[54.9,57.9]	[59.4,62.4]	4.0	3.5
G034.391+00.214	57.3	4.8	57.5	1.5	–	[59.4,60.4]	–	2.9
G034.411+00.234	57.8	7.6	58.1	2.7	[53.4,56.4]	[58.9,61.4]	4.7	3.3
G034.459+00.247	58.7	3.8	58.8	1.0	[55.9,58.4]	[59.9,61.4]	2.9	2.6
G035.026+00.349	53.1	8.7	52.6	5.4	[49.1,51.1]	[53.6,58.1]	3.5	5.5
G035.344+00.347	94.5	8.9	94.7	3.7	[92.1,93.6]	[95.6,96.6]	2.6	1.9
G035.457−00.179	65.1	7.4	65.2	2.5	[62.2,63.7]	[66.7,67.2]	3.0	2.0
G035.466+00.141	76.8	8.9	77.3	3.7	[74.2,76.2]	[78.2,80.2]	3.1	2.9
G035.497−00.021	58.0	5.6	58.0	1.6	[52.7,57.2]	[59.2,62.2]	5.3	4.2
G035.522−00.274	45.4	3.7	45.1	1.1	[43.7,45.2]	[46.2,47.7]	1.4	2.6
G035.577+00.047	50.0	7.9	48.5	1.8	[40.2,48.7]	[54.7,58.2]	8.3	9.7
G035.577+00.067	49.8	6.5	50.1	2.2	[45.2,48.2]	[50.7,57.2]	4.9	7.1
G035.579−00.031	52.9	11.3	53.0	2.6	[45.7,48.7]	[53.7,59.2]	7.3	6.2
G035.602+00.222	49.6	4.7	49.6	1.7	[47.7,48.7]	[51.2,52.2]	1.9	2.6
G035.681−00.176	28.3	3.8	28.1	1.1	[26.7,27.2]	[29.2,30.2]	1.4	2.1
G036.406+00.021	57.8	11.2	57.8	5.4	[54.2,56.2]	[60.2,62.7]	3.6	4.9
G036.794−00.204	78.3	4.1	78.1	2.1	[75.7,77.7]	[78.7,80.2]	2.4	2.1
G036.826−00.039	60.2	5.8	60.6	2.8	[58.2,59.2]	[61.2,62.2]	2.4	1.6
G037.043−00.036	81.5	4.8	81.3	2.2	[79.5,80.5]	[82.5,83.0]	1.8	1.7
G037.268+00.081	91.1	6.0	91.5	3.3	–	[92.5,94.5]	–	3.0
G037.374−00.236	39.2	4.9	40.0	2.5	[35.5,37.5]	[40.5,43.5]	4.5	3.5
G037.546−00.112	52.7	12.8	52.7	2.7	[49.0,50.5]	[53.5,57.0]	3.7	4.3
G037.672−00.091	47.9	4.4	48.2	2.2	[46.5,47.5]	[48.5,49.0]	1.7	0.8
G037.734−00.112	46.1	7.5	45.6	2.7	[43.5,44.0]	[47.5,49.5]	2.1	3.9
G037.819+00.412	17.5	8.9	17.2	3.1	[14.6,16.1]	[19.6,21.1]	2.6	3.9
G037.874−00.399	60.7	11.9	60.8	3.6	[52.1,55.1]	[66.1,68.6]	8.7	7.8
G038.037−00.041	55.9	10.3	56.0	3.5	[53.1,55.6]	[56.6,58.1]	2.9	2.1
G038.119−00.229	83.5	9.5	83.1	5.0	[80.1,82.6]	[85.1,87.1]	3.0	4.0
G038.646−00.226	69.1	11.8	68.7	6.7	[66.6,68.6]	[69.6,72.1]	2.1	3.4
G038.917−00.402	40.8	11.4	40.7	3.4	[39.3,39.8]	[41.3,41.8]	1.4	1.1
G038.921−00.351	38.8	11.9	39.0	3.1	[35.3,37.8]	[39.8,40.8]	3.7	1.8
G038.934−00.361	39.7	11.8	40.0	3.2	[37.3,37.8]	[40.3,42.3]	2.7	2.3
G038.937−00.457	41.6	11.5	41.6	4.9	[38.8,41.3]	[42.3,43.8]	2.8	2.2
G038.957−00.466	42.2	5.7	42.0	2.4	[40.3,41.3]	[43.3,44.3]	1.7	2.3
G039.591−00.204	64.5	8.9	64.5	2.7	[63.1,63.6]	[65.1,66.6]	1.4	2.1
G039.851−00.204	57.3	4.0	56.6	2.3	[55.1,56.6]	[58.6,59.6]	1.5	3.0
G039.884−00.346	58.2	7.7	58.3	2.4	[54.1,57.1]	[60.6,62.6]	4.2	4.3
G040.283−00.219	73.9	9.8	73.8	3.9	[66.1,72.6]	[77.1,77.6]	7.7	3.8
G040.622−00.137	32.8	5.5	32.6	1.6	[26.2,31.2]	[33.7,38.7]	6.4	6.1
G040.814−00.416	80.3	3.1	80.2	2.3	[78.7,79.2]	[81.7,83.2]	1.5	3.0
G041.031−00.226	60.8	10.8	60.9	3.7	[57.2,60.2]	[62.2,63.7]	3.7	2.8
G041.226−00.197	59.5	8.0	59.5	2.0	[52.2,57.7]	[59.7,68.7]	7.3	9.2
G041.307−00.171	57.7	3.4	57.1	1.0	[51.2,56.7]	–	5.9	–
G041.507−00.106	63.0	4.0	62.8	1.5	[61.6,62.1]	[64.1,64.6]	1.2	1.8
G042.108−00.447	55.2	8.9	54.7	2.7	[52.3,54.8]	[56.3,59.3]	2.4	4.6
G043.038−00.452	57.8	9.2	57.8	4.0	[54.3,56.8]	[59.3,63.3]	3.5	5.5
G043.108+00.044	12.5	3.7	12.8	1.1	[8.3,10.3]	[13.8,16.3]	4.5	3.5
G043.124+00.031	9.3	5.8	6.8	1.1	[0.8,8.3]	[10.3,17.3]	6.0	10.5
G043.148+00.014	7.0	16.8	9.5	1.7	[−2.2,−0.2]	[10.3,16.3]	11.7	6.8
G043.164−00.029	13.7	11.2	13.7	2.3	[2.3,11.3]	[17.3,25.3]	11.4	11.6
G043.236−00.047	6.3	7.6	6.8	1.9	[3.3,4.3]	[9.8,10.8]	3.5	4.0
G043.306−00.212	59.2	7.8	59.4	4.4	[57.3,58.3]	[61.3,62.8]	2.1	3.4
G043.519+00.016	62.9	5.3	62.9	2.5	[61.3,61.8]	[64.3,64.8]	1.6	1.9
G043.528+00.017	61.6	6.2	62.5	3.4	–	[63.8,64.3]	–	1.8
G043.794−00.127	44.1	13.5	43.7	6.9	[36.8,42.3]	[45.8,52.3]	6.9	8.6
G043.817−00.119	46.3	3.6	46.4	2.0	[42.8,45.3]	[47.3,48.8]	3.6	2.4
G044.309+00.041	56.9	4.8	56.8	1.9	[53.2,54.7]	[58.2,61.2]	3.6	4.4
G045.071+00.132	58.4	13.3	58.6	3.0	[50.9,53.4]	[61.9,63.9]	7.7	5.3
G045.121+00.131	58.7	14.0	58.8	3.5	[52.9,57.4]	[60.9,64.9]	5.9	6.1
G045.454+00.061	58.5	9.1	58.7	2.8	[52.1,57.6]	[60.6,63.6]	6.6	4.9
G045.463+00.027	58.3	3.5	58.0	1.3	[54.1,57.1]	[59.1,61.6]	3.9	3.6
G045.466+00.046	60.7	7.9	61.5	2.2	[54.1,58.6]	[62.1,67.6]	7.4	6.1
G045.474+00.134	62.1	11.5	61.5	3.1	[54.6,60.1]	–	6.9	–
G045.543−00.007	55.5	10.9	55.8	2.5	[53.1,53.6]	[56.6,59.1]	2.7	3.3
G045.544−00.032	55.5	9.8	55.3	3.7	[53.1,55.1]	[56.1,57.1]	2.2	1.8
G045.804−00.356	59.2	6.5	58.4	4.5	[54.9,58.4]	[60.4,63.4]	3.5	5.0
G045.829−00.292	60.8	11.5	60.9	6.1	[59.4,60.4]	[61.4,62.4]	1.5	1.5
G046.118+00.399	55.3	4.9	55.6	3.1	[53.9,54.4]	[56.9,57.9]	1.7	2.3

TABLE 10
^{13}CO outflow properties of all blue and red lobes for 153 ATLASGAL clumps : blue/red lobe length $l_{b/r}$ [pc], masses M_b(blue), M_r(red), M_{out}(M_{out} = M_b + M_r)[$M_\odot$], momentum p[10 $M_\odot$ km s^{-1}], energy E[10^{39} J], dynamic time t_d[10^4 yr], mass entrainment rates $\dot{M}_{out}$[10^{-4} $M_\odot$/yr], mechanical force F_{CO}[10^{-3} $M_\odot$ km s^{-1}/yr], and mechanical luminosity L_{CO}[$L_\odot$].

ATLASGAL CSC Gname	l_b (pc)	l_r (pc)	M_b ($M_\odot$)	M_r ($M_\odot$)	M_{out} ($M_\odot$)	p (10 $M_\odot$ km s^{-1})	E (10^{39} J)	t_d (10^4 yr)	$\dot{M}_{out}$ ($10^{-4} M_\odot$/yr)	F_{CO} ($10^{-3} M_\odot$ km s^{-1}/yr)	L_{CO} ($L_\odot$)
G027.784+00.057	1.1	0.6	39.4	5.4	44.8	20.8	2.4	14.8	2.9	1.2	1.2
G027.903−00.012	0.8	1.0	18.8	18.8	37.6	14.0	0.8	24.5	1.5	0.6	0.28
G027.919−00.031	0.5	0.5	3.0	9.5	12.4	4.6	0.16	16.0	0.7	0.2	0.08
G027.936+00.206	0.2	0.2	1.9	3.2	5.1	3.8	0.4	3.1	1.6	1.2	0.8
G027.978+00.077	0.5	1.0	7.4	13.3	20.7	12.6	1.2	16.1	1.2	0.8	0.4
G028.148−00.004	0.5	0.6	5.4	8.5	13.9	5.0	0.32	14.6	0.9	0.4	0.16
G028.151+00.171	0.6	1.2	6.0	2.7	8.7	4.0	0.28	25.5	0.3	0.14	0.08
G028.199−00.049	0.8	1.5	83.5	86.0	169.5	176.0	38.8	9.7	16.8	16.6	30.8
G028.234+00.062	0.4	0.5	8.2	6.9	15.0	6.6	0.36	15.9	0.9	0.4	0.2
G028.244+00.012	1.0	1.0	26.0	25.5	51.5	28.2	2.0	21.8	2.3	1.2	0.8
G028.288−00.362	1.9	1.5	312.5	193.9	506.5	353.4	54.8	18.3	26.6	17.8	23.2
G028.301−00.382	1.7	2.2	118.0	118.0	236.0	117.0	9.2	32.6	7.0	3.2	2.0
G028.321−00.009	0.5	0.9	13.9	10.7	24.6	10.6	0.8	18.3	1.3	0.6	0.36
G028.438+00.036	0.6	0.9	12.7	14.2	26.9	10.2	0.4	21.2	1.2	0.4	0.2
G028.469−00.282	1.4	1.2	37.5	54.7	92.2	29.8	1.2	40.9	2.2	0.6	0.24
G028.608+00.019	0.7	0.7	53.9	59.0	112.8	99.8	11.6	6.3	17.2	14.6	14.0
G028.608−00.027	0.2	0.2	2.6	1.3	3.9	0.6	0.04	5.3	0.7	0.1	0.08
G028.802−00.022	2.0	1.5	5.6	12.1	17.7	16.6	1.2	31.6	0.5	0.4	0.28
G028.831−00.252	0.5	0.8	18.0	21.4	39.4	44.8	4.0	6.4	5.9	6.4	4.8
G028.861+00.066	1.0	0.6	4.1	96.7	100.8	245.4	6.8	9.1	10.6	24.8	5.6
G028.881−00.021	0.8	0.7	33.2	10.3	43.6	15.2	1.2	19.7	2.1	0.8	0.4
G028.974+00.081	1.3	0.9	28.7	21.3	50.1	6.4	0.4	33.0	1.5	0.18	0.08
G029.002+00.067	1.6	1.4	101.3	92.7	194.1	89.2	7.2	47.4	3.9	1.8	1.2
G029.476−00.179	0.8	0.8	15.9	30.3	46.2	27.4	1.6	15.2	2.9	1.6	0.8
G029.937−00.052	1.6	1.6	45.8	32.9	78.7	104.0	17.2	11.4	6.6	8.4	11.6
G029.954−00.016	0.7	1.3	143.5	118.7	262.2	177.8	28.4	11.6	21.7	14.0	18.8
G029.959−00.067	0.9	0.6	8.7	18.2	27.0	6.8	0.8	12.5	2.1	0.4	0.4
G030.010+00.034	1.3	1.1	6.2	10.6	16.9	14.8	2.8	23.9	0.7	0.6	0.8
G030.019−00.047	0.4	0.5	53.7	10.1	63.8	17.0	4.0	3.5	17.5	4.4	8.8
G030.023+00.106	0.8	1.2	10.6	16.7	27.3	16.0	0.8	16.0	1.6	1.0	0.4
G030.029+00.117	1.1	0.9	8.4	11.6	20.0	7.2	0.4	22.9	0.8	0.2	0.12
G030.094+00.047	0.8	0.9	18.2	9.5	27.7	14.0	1.2	20.1	1.3	0.6	0.4
G030.224−00.179	1.5	1.2	12.2	91.8	103.9	106.2	3.2	17.9	5.6	5.4	1.6
G030.299−00.202	0.9	0.4	2.2	49.5	51.7	234.6	2.4	8.7	5.7	24.6	2.0
G030.348+00.392	0.6	1.3	6.4	4.9	11.3	5.0	0.28	34.6	0.3	0.14	0.04
G030.386−00.104	0.8	0.5	38.7	12.6	51.3	26.0	2.0	18.1	2.7	1.4	0.8
G030.399−00.296	1.0	0.7	6.2	15.6	21.8	18.8	2.0	11.1	1.9	1.6	1.2
G030.419−00.231	0.7	0.7	14.7	27.9	42.6	26.0	3.2	4.7	8.7	5.0	5.2
G030.534+00.021	1.7	1.3	491.2	108.5	599.6	391.8	60.8	13.4	43.0	26.8	34.8
G030.588−00.042	1.6	1.0	313.3	148.1	461.3	484.4	82.4	12.3	35.9	36.0	51.6
G030.624+00.169	0.8	1.0	11.7	6.2	17.9	9.8	0.8	23.2	0.7	0.4	0.24
G030.648−00.119	1.0	1.1	7.9	6.8	14.7	5.8	0.24	37.6	0.4	0.14	0.04
G030.651−00.204	0.5	0.9	14.2	8.8	23.0	19.2	3.6	5.9	3.7	3.0	4.8
G030.659+00.229	1.1	1.1	11.7	13.8	25.5	10.0	0.4	37.2	0.7	0.2	0.08
G030.663−00.144	0.9	0.5	23.4	3.7	27.2	8.2	0.4	22.1	1.2	0.4	0.16
G030.684−00.261	0.6	0.7	23.5	23.7	47.2	36.0	4.4	10.0	4.5	3.4	3.2
G030.693−00.149	1.4	1.1	10.2	18.0	28.2	26.8	1.6	23.5	1.1	1.0	0.4
G030.703−00.067	1.9	1.0	45.2	23.0	68.1	71.6	16.0	10.2	6.4	6.4	12.4
G030.753−00.051	1.0	0.8	46.6	33.4	80.0	148.6	16.8	7.7	10.0	17.8	16.8
G030.756+00.206	0.6	0.9	7.1	16.6	23.7	13.2	1.2	18.0	1.3	0.6	0.4
G030.763−00.031	0.8	1.3	65.8	68.1	133.9	252.4	80.4	4.6	27.9	50.0	134.4
G030.773−00.216	1.0	0.5	17.7	27.6	45.3	32.0	4.8	7.5	5.8	4.0	5.2
G030.784−00.021	0.9	1.4	16.8	34.8	51.6	73.4	19.2	4.8	10.4	14.2	31.2
G030.786+00.204	0.8	0.5	27.2	25.2	52.4	51.2	8.0	5.7	8.8	8.2	10.8
G030.818+00.274	0.6	0.6	14.6	9.4	24.0	9.4	0.8	13.1	1.8	0.6	0.4
G030.828+00.134	0.3	0.7	4.9	3.1	8.0	3.8	0.28	15.8	0.5	0.2	0.12
G030.828−00.122	0.2	0.3	3.0	3.9	6.9	3.2	0.2	6.3	1.0	0.4	0.24
G030.839−00.019	1.2	1.5	6.9	57.9	64.8	193.6	6.0	13.9	4.5	12.8	3.2
G030.866+00.114	0.9	1.6	146.3	244.2	390.5	277.2	29.6	15.9	23.6	16.0	14.4
G030.866−00.119	1.3	1.1	30.4	18.6	49.0	70.6	18.0	7.2	6.5	9.0	19.2
G030.874−00.094	0.5	0.7	27.6	24.3	51.9	41.4	5.2	9.7	5.1	4.0	4.0
G030.886−00.231	2.8	1.2	80.2	54.3	134.5	85.2	8.4	43.9	2.9	1.8	1.6
G030.898+00.162	0.6	0.7	13.0	12.1	25.2	31.4	8.0	4.3	5.7	6.8	14.4
G030.901−00.034	0.5	0.6	4.7	1.7	6.3	1.8	0.12	16.2	0.4	0.1	0.04
G030.959+00.086	1.6	1.7	202.2	225.6	427.8	237.0	24.0	15.1	27.2	14.4	12.0
G030.971−00.141	0.5	0.9	9.7	12.2	21.9	9.0	0.8	17.0	1.2	0.4	0.32
G030.978+00.216	1.2	0.4	7.5	8.6	16.1	11.2	0.4	28.9	0.5	0.4	0.16
G030.996−00.076	0.8	1.0	17.6	57.3	74.9	41.8	3.2	13.6	5.3	2.8	1.6
G031.024+00.262	0.8	1.5	7.8	9.4	17.2	5.8	0.4	26.7	0.6	0.2	0.12
G031.046+00.357	1.0	1.0	19.1	21.3	40.5	17.6	1.2	18.7	2.1	0.8	0.4
G031.071+00.049	0.4	0.5	7.7	9.5	17.2	8.2	0.4	8.8	1.9	0.8	0.4
G031.121+00.062	0.5	0.5	10.3	8.4	18.7	11.0	1.2	6.4	2.8	1.6	1.6
G031.148−00.149	0.5	0.6	1.5	1.9	3.4	1.4	0.08	14.7	0.2	0.1	0.04
G031.158+00.047	0.3	0.4	2.6	3.5	6.2	5.8	0.8	4.6	1.3	1.2	1.2
G031.208+00.101	1.2	0.8	33.4	7.9	41.3	22.2	2.0	22.6	1.8	1.0	0.8
G031.243−00.111	1.7	2.1	270.2	79.5	349.7	321.4	38.0	26.8	12.5	11.0	10.8
G031.281+00.062	1.5	0.9	70.5	33.1	103.6	99.2	13.6	14.3	7.0	6.4	7.6
G031.396−00.257	1.2	1.7	173.0	253.4	426.4	320.6	31.2	14.7	27.9	20.0	16.4
G031.412+00.307	0.6	0.9	42.7	29.7	72.3	61.0	8.8	8.0	8.7	7.0	8.4

TABLE 10
–continuum^{13}CO outflow properties of all blue and red lobes for 153 ATLASGAL clumps

ATLASGAL CSC Gname	l_b (pc)	l_r (pc)	M_b ($M_\odot$)	M_r ($M_\odot$)	M_{out} ($M_\odot$)	p ($10\,M_\odot\,km\,s^{-1}$)	E (10^{39} J)	t_d (10^4 yr)	$\dot{M}_{out}$ ($10^{-4}M_\odot$/yr)	F_{CO} ($10^{-3}M_\odot\,km\,s^{-1}$/yr)	L_{CO} ($L_\odot$)
G031.542−00.039	0.3	0.3	1.1	1.1	2.2	0.6	0.028	10.5	0.2	0.06	0.024
G031.568+00.092	0.8	0.8	9.2	12.2	21.4	7.6	0.32	26.6	0.8	0.2	0.08
G031.581+00.077	0.7	0.7	72.0	32.1	104.2	53.8	6.4	7.3	13.7	6.8	6.8
G031.644−00.266	0.3	0.3	2.8	1.9	4.7	1.6	0.08	8.3	0.5	0.18	0.08
G032.117+00.091	0.6	0.8	42.5	68.0	110.5	77.2	7.2	9.3	11.4	7.6	6.0
G032.149+00.134	0.6	0.8	39.4	57.6	97.0	84.8	6.4	12.1	7.7	6.4	4.0
G032.456+00.387	0.4	0.4	5.3	5.1	10.5	3.8	0.16	8.4	1.2	0.4	0.16
G032.471+00.204	1.0	2.0	66.8	33.4	100.2	76.6	9.6	21.1	4.6	3.4	3.6
G032.604−00.256	1.3	0.8	24.2	4.9	29.1	11.0	0.8	34.6	0.8	0.2	0.12
G032.744−00.076	1.1	0.9	110.4	52.5	162.9	164.4	25.2	11.4	13.7	13.2	16.8
G032.797+00.191	1.3	1.6	841.3	950.3	1791.6	2288.6	385.2	10.0	172.3	210.0	297.2
G032.821−00.331	0.3	0.4	7.9	7.4	15.3	14.0	2.8	2.7	5.4	4.8	7.6
G032.990+00.034	1.2	1.7	75.3	95.7	170.9	136.0	10.8	19.6	8.4	6.4	4.4
G033.133−00.092	1.0	0.8	86.9	104.9	191.7	180.4	20.8	8.4	21.8	19.6	19.2
G033.264+00.067	1.1	0.9	25.5	10.1	35.6	16.8	1.2	27.7	1.2	0.6	0.32
G033.288−00.019	0.7	0.5	11.1	13.7	24.8	11.2	0.8	16.8	1.4	0.6	0.28
G033.338+00.164	0.5	0.7	23.8	14.1	37.9	9.8	0.4	18.3	2.0	0.4	0.2
G033.388+00.199	0.7	0.7	10.7	19.6	30.3	15.0	0.4	20.3	1.4	0.6	0.16
G033.389+00.167	1.8	2.0	42.9	32.0	74.9	23.4	1.2	46.0	1.6	0.4	0.24
G033.393+00.011	1.0	1.3	39.3	25.8	65.1	45.8	6.8	11.3	5.5	3.8	4.8
G033.416−00.002	0.8	2.0	43.3	79.3	122.6	62.0	4.0	35.6	3.3	1.6	0.8
G033.418+00.032	0.6	0.9	16.8	25.1	41.8	14.0	0.8	24.6	1.6	0.6	0.24
G033.651−00.026	0.8	1.4	18.8	8.8	27.6	12.8	0.8	32.5	0.8	0.4	0.2
G033.809−00.159	0.5	0.4	5.7	10.6	16.3	5.8	0.32	16.0	1.0	0.4	0.16
G033.914+00.109	0.5	0.6	49.1	41.9	91.1	51.0	4.8	6.6	13.3	7.2	6.0
G034.096+00.017	0.4	0.2	2.0	3.2	5.2	3.8	0.4	5.4	0.9	0.6	0.4
G034.258+00.154	0.3	0.4	36.9	9.0	45.9	44.4	8.0	2.5	17.5	16.2	24.4
G034.459+00.247	0.1	0.2	1.4	1.4	2.8	1.0	0.08	4.2	0.6	0.2	0.12
G035.026+00.349	1.1	1.8	71.7	236.6	308.4	433.2	22.4	20.3	14.6	19.6	8.4
G035.344+00.347	0.5	0.4	7.2	4.4	11.6	5.0	0.32	13.4	0.8	0.4	0.2
G035.457−00.179	0.8	0.5	8.9	2.2	11.1	7.8	0.8	18.7	0.6	0.4	0.28
G035.466+00.141	0.9	1.8	62.5	50.1	112.6	55.4	4.0	34.9	3.1	1.4	0.8
G035.577+00.047	1.3	2.1	284.5	57.7	342.2	238.6	48.4	13.8	23.7	15.8	26.8
G035.579−00.031	0.8	0.7	67.8	102.8	170.5	297.8	40.4	6.2	26.5	44.2	50.8
G035.602+00.222	0.3	0.3	1.1	1.0	2.1	0.8	0.04	6.9	0.3	0.12	0.08
G035.681−00.176	0.5	0.5	0.5	0.9	1.4	0.6	0.024	15.6	0.08	0.04	0.012
G036.406+00.021	0.5	0.4	18.2	10.4	28.6	21.4	2.4	7.1	3.9	2.8	2.4
G036.826−00.039	0.6	0.4	3.3	2.3	5.6	2.6	0.16	16.7	0.3	0.14	0.08
G037.043−00.036	0.7	0.3	9.2	3.0	12.2	5.0	0.24	23.1	0.5	0.2	0.08
G037.374−00.236	0.2	0.4	5.0	6.1	11.2	8.8	0.8	6.2	1.7	1.4	1.2
G037.546−00.112	1.3	0.9	56.1	156.1	212.2	251.0	8.8	21.8	9.3	10.6	3.2
G037.672−00.091	1.6	1.2	34.9	20.6	55.5	15.6	0.8	75.4	0.7	0.2	0.08
G037.734−00.112	1.2	1.8	74.7	97.7	172.4	85.0	8.4	33.0	5.0	2.4	2.0
G037.819+00.412	0.9	1.1	74.4	42.0	116.3	81.4	6.8	19.5	5.7	3.8	2.8
G037.874−00.399	1.1	1.1	87.1	48.2	135.3	305.8	94.0	6.0	21.7	46.8	120.8
G038.037−00.041	0.6	0.6	16.5	9.1	25.6	10.4	0.8	14.1	1.7	0.6	0.4
G038.119−00.229	0.7	0.4	38.9	12.4	51.3	25.4	2.0	11.9	4.2	2.0	1.2
G038.646−00.226	0.7	0.5	19.5	21.6	41.0	13.0	0.8	15.7	2.5	0.8	0.32
G038.917−00.402	0.4	0.4	4.2	5.4	9.6	3.4	0.08	18.9	0.5	0.16	0.04
G038.921−00.351	0.5	0.4	8.0	4.3	12.3	7.0	0.4	10.7	1.1	0.6	0.36
G038.937−00.457	0.5	0.6	6.3	2.8	9.1	2.8	0.16	14.8	0.6	0.18	0.08
G038.957−00.466	0.4	0.3	4.1	1.5	5.7	2.4	0.12	10.3	0.5	0.2	0.08
G039.851−00.204	1.9	1.9	74.2	52.5	126.7	29.4	2.8	50.8	2.4	0.6	0.4
G039.884−00.346	1.1	1.6	66.6	42.1	108.7	71.0	7.6	19.3	5.4	3.4	3.2
G040.283−00.219	1.1	1.6	79.6	6.3	85.9	79.2	10.4	16.3	5.1	4.4	4.8
G040.622−00.137	1.5	0.9	120.3	125.9	246.2	202.2	21.2	13.9	17.0	13.4	12.0
G040.814−00.416	0.2	0.3	1.5	1.4	2.9	1.4	0.08	7.9	0.3	0.16	0.08
G041.031−00.226	1.4	1.3	67.5	12.0	79.5	31.4	2.0	25.0	3.1	1.2	0.4
G041.507−00.106	1.8	2.3	25.6	8.6	34.2	10.6	0.4	89.0	0.4	0.1	0.036
G042.108−00.447	1.1	1.6	122.0	109.8	231.8	77.2	8.4	22.7	9.8	3.2	2.8
G043.124+00.031	2.8	2.8	376.0	228.2	604.2	460.2	82.4	19.8	29.4	21.4	32.0
G043.148+00.014	2.2	2.0	287.6	478.3	765.8	2246.4	440.4	14.0	52.6	147.2	242.8
G043.164−00.029	2.5	1.6	1145.1	920.1	2065.3	2964.6	786.4	12.1	164.5	225.2	502.8
G043.236−00.047	1.1	3.0	336.8	245.3	582.1	488.6	74.8	32.2	17.3	13.8	18.0
G043.306−00.212	0.4	0.3	9.3	4.3	13.6	6.6	0.4	8.0	1.6	0.8	0.4
G043.794−00.127	1.1	1.0	268.5	235.0	503.5	513.0	76.8	7.7	62.6	60.8	76.8
G044.309+00.041	0.8	0.5	22.3	12.8	35.1	23.8	2.8	11.1	3.0	2.0	2.0
G045.071+00.132	0.3	0.5	21.7	43.8	65.5	114.4	21.2	3.1	20.2	33.6	52.0
G045.121+00.131	1.0	1.0	123.1	90.2	213.3	247.0	46.4	5.8	35.2	39.0	61.6
G045.454+00.061	0.9	1.9	146.6	156.1	302.8	256.2	35.2	16.9	17.2	14.0	16.0
G045.543−00.007	0.8	1.1	16.3	41.2	57.5	53.2	2.0	22.1	2.5	2.2	0.8
G045.544−00.032	1.1	1.1	38.2	18.9	57.1	16.0	0.8	32.6	1.7	0.4	0.16
G045.804−00.356	1.0	0.7	35.3	30.9	66.2	37.4	3.2	13.4	4.7	2.6	2.0
G045.829−00.292	1.3	1.6	29.4	29.2	58.6	14.2	0.4	63.7	0.9	0.2	0.08